Gran Sasso Science Institute

PHD PROGRAMME IN MATHEMATICS IN NATURAL, SOCIAL AND LIFE SCIENCES
Cycle XXX
09/11/2017

Fluid–Structure Interaction in the left ventricle of the human heart: numerical simulations and experimental validation

PHD CANDIDATE
Valentina Meschini

ADVISOR
Prof. Roberto Verzicco
Università di Roma Tor Vergata

GRAN SASSO SCIENCE INSTITUTE
SCHOOL OF ADVANCED STUDIES
Scuola Universitaria Superiore

SISSA
Scuola Internazionale Superiore di Studi Avanzati

Gran Sasso Science Institute

PHD PROGRAMME IN MATHEMATICS IN NATURAL, SOCIAL AND LIFE SCIENCES

Cycle XXX

09/11/2017

Fluid–Structure Interaction in the left ventricle of the human heart: numerical simulations and experimental validation

PHD CANDIDATE
Valentina Meschini

ADVISOR
Prof. Roberto Verzicco
Università di Roma Tor Vergata

GRAN SASSO SCIENCE INSTITUTE
SCHOOL OF ADVANCED STUDIES
Scuola Universitaria Superiore

SISSA
Scuola Internazionale Superiore di Studi Avanzati

Thesis Jury Members

Prof. Gianni Pedrizzetti (Jury President, Università di Trieste)

Prof. Luca Helthai (SISSA, Trieste)

Prof. Marco D. de Tullio (Politecnico di Bari)

Dr. Mauro Chinappi (Università di Roma Tor Vergata)

Dr. Stefano Spirito. (Università dell'Aquila)

Thesis Referees

Prof. Antonio De Simone (SISSA, Trieste)

Prof. Rajat Mittal (Johns Hopkins University, Baltimore)

To Prof. Roberto Verzicco
& Prof. Alberto Branciari

for being the best teaching models
I could have ever desired to meet
during all the course of my studies,
from High School till now

Acknowledgements

This goal would not have been achieved without the support and affection of many people and these lines are for thanking all of them.

The first person I would like to address my thought is my advisor Prof. Roberto Verzicco for the great work you have done with me. It seems to me that so long time has passed since that first year of PhD, when things did not go so well to me and I was even thinking to leave; but then I met you, who proposed to me this challenging project, even though I did not know almost anything about fluid dynamics, and told me not to worry as we would have embarked on that journey together. I have to admit that the first months were very difficult, since we could not see the outcomes of our hard effort, but every week I came in Rome I felt enriched of some new skills. Then the good period arrived and I cannot forget our emotion when the code started working and we got our first prototype of the ventricle, actually half of a sphere, beating. From then on we have reached a series of very interesting results with prestigious scientific collaborations. For all these reasons this thesis is dedicated to you because you are a special advisor, you have made me grow scientifically and become more conscious of myself; also from a human point of view without realizing you have taught me a lot of everyday life. I feel really proud of being your student and I wish to continue working with you.

A deserved thank is for Prof. Marco de Tullio. Your contribution has been fundamental in the realization of this work and you have turned out to be always extremely kind in helping and prompt in replying to my questions.

I feel to owe a friendly thank to Vamsi. It has been a pleasure to work with you in the development of the computational model and I have learnt a lot from our collaboration. I enjoyed our non scientific chats during the conferences we attended together, you deserve all the best academic achievements.

Another due thank is for Prof. Rajat Mittal for the interesting conversations we had on cardiovascular topics. Your comments have been crucial in understanding what we had to improve in the model and your suggestion to try to study a specific pathology has been very challenging for me. I hope to have the opportunity to go on working together.

A very special thank is for my math High School teacher Alberto Branciari. It was my desire to dedicate this thesis also to you because I am sure that without a teacher like you I would have never decided to take this course of studies and reached such a goal. For more than ten years you represents a fixed point in my life, and I know that I can count on you for every doubt or problem I have, from mathematics to everyday issues.

Now it is time to thank the Gran Sasso Science Institute professor board which gave me the opportunity to enroll in this PhD programme. I lived three

very intense years in L'Aquila, with the privilege of moving around the world for conferences and meeting the most representative scientists of my research field: this has been an invaluable added factor to my formation. Except from research, I feel really grateful for the very nice and special people of all the GSSI staff I had the luck to meet, Solange, Annastella and Emily above all, and it is also thanks to them that I can say to feel at home.

An affectionate thank is for Elena, with whom I shared everything: the flat, the office, the first year exams, the bad times and especially the unforgettable happy moments in L'Aquila. As I told you several times, you are unique and I feel very lucky to have met you on my way, but you need to make every effort in becoming stronger in making decisions and more conscious of your qualities and potentialities that are really a lot, I assure. It is very difficult for me to think to my everyday life without you, but this is just the beginning of a new chapter which you will continue to be part of. Never forget "Ti voglio bene".

Another tender thought is for my friend Eirini. Despite you call me "bully", you are the most "stratenera" girl, always ready to help everyone and to take care of the people you love. It has been wonderful to share these years with you and I am sure that this is only the beginning of a long-lasting friendship.

I want to thank my other adventure friend Giancarlo, for the very funny moments we had together especially during the first year. We shared a lot of chats on different subjects, from serious life problems to gossip and stupid stuff. I really wish you can realize your dreams in the future.

There are some other students of my PhD XXX cycle I cannot exempt myself from thanking: Mora, Valeria, Andrea, Claudio, Marco, Emilio, Cosimo, Gianluca and Feliciano. Even though in these three years we have not been all very close geographically, we had a lot of fun together and I always will bring all those moments with me. Moreover during this last year I had the luck to meet other GSSI students, the so called "strateneri group", with whom I spent most of my free time, playing volleyball, board and card games, and especially soccer table during our long lunch break. Thanks to Manuel, Stefano, Lorenzo, Francesco and Raffaello, you all know I always have very "nice" words for each of you, but only for this time I will pass over and I will say something new: "I love you all and I will miss you".

Thanks to those friends of mine whose presence and love I always feel at my side: Martina, Matteo, Chiara, Lorenzo and Claudia.

Last, but not least, a devoted thank is for my whole family. Thanks to my parents Rita and Stefano, for putting always your trust in me, in every choice I make and especially for supporting me in the difficult periods of my life; you are precious mentor for me. A tender thought is addressed to my sister Federica. You are for me an extraordinary example of determination and dedication in doing everything at your best. I hope we will continue to be as close as we are now, I love you and I wish the best for your future life.

Finally I feel to owe a loving thank to Andrea for being the most important part of my life. Thanks for supporting and pushing me to make important decisions for my own good, even when this leads me far from you. You cannot even imagine how your words have allowed me to carry on, in spite of difficulties, and how you have always made me smile. This thesis is also a bit yours for the care you put in its aesthetic appearance and in my English revision. Thanks for always being there.

Contents

Chapter 1

Introduction

1.1 Cardiovascular hemodynamics: background and motivations

The understanding of the most basic principles of the cardiovascular system has been a hard conquest for the scientific community, achieved as the outcome of extensive medical studies over many centuries.

In ancient times the greatest obstacle for a correct knowledge of the heart and its system was represented by Aristotle and his belief that the role of this organ was of being the source of body heat, then transferred by blood vessels to the whole organism.

We have to wait the birth and proliferation of Christianity in order to see considerable advances; these have been possible thanks to the contribution of the Greek physician Galen, lived in the first centuries. He was the first to observe the presence of blood in vessels, instead of air as according to the conviction of his time, and to recognize the existence of two circulatory systems, the venous and the arterial one. Even though his work contained relevant scientific errors, such as his conjecture that blood was generated in the liver and its circulation began from the gastric and intestinal vessels, his theories dominated and influenced western medical science for almost 1500 years.

Only much later, in the 17th century, Sir William Harvey inaugurated modern cardiovascular research with his treatise entitled *De Motu Cardis*. Basing on his many years of experiments and observations as a scientist and physician, he finally established that blood circulates while the heart acting as a pump, providing the first accurate description of the human cardiovascular system. All those spiritualistic functions conferred to the heart until that time had been finally wiped out in favour of the awareness of its correct role, which consists of supplying oxygenated blood to the whole body and then transporting the de-oxygenated blood to the respiratory system for oxygen replenishment. It is a muscular organ composed of two separate volumetric pumps, the left and the right, each one comprising an atrium and a ventricle and two valves, the aortic and the mitral, which ensure the correct flow direction, as shown in figure 1.1. The atria receive blood from the veins, while the ventricles pump it out of the heart and through the circulatory system. More precisely the right atrium is responsible for collecting de–oxygenated blood from the vena cava, and then passes it via the tricuspid valves; the blood goes into the right ventricle for pumping into the lungs through the pulmonary valve and via the pulmonary artery for oxygenation; the oxygenated blood returns via the pulmonary vein into the left atrium and then is squeezed into the left ventricle through the mitral valve, which is fastened to its walls by chordae tendineae and papillary muscles; the left ventricle is the strongest chamber of the heart as it provides the oxygenated blood to the rest of the human body. Therefore, due to the high pressure it has to withstand, it represents the part of the heart most exposed to damages, which in case of severe impairing may lead to cardiac pathologies, such as myocardial infarction, heart failure, valvular disease, cardiomyopathy.

According to the Heart Disease and Stroke Statistics Update presented by the American Heart Association (Benjamin, 2017) by 2030 almost 44% of the US adult population is projected to have some form of cardiovascular disease.

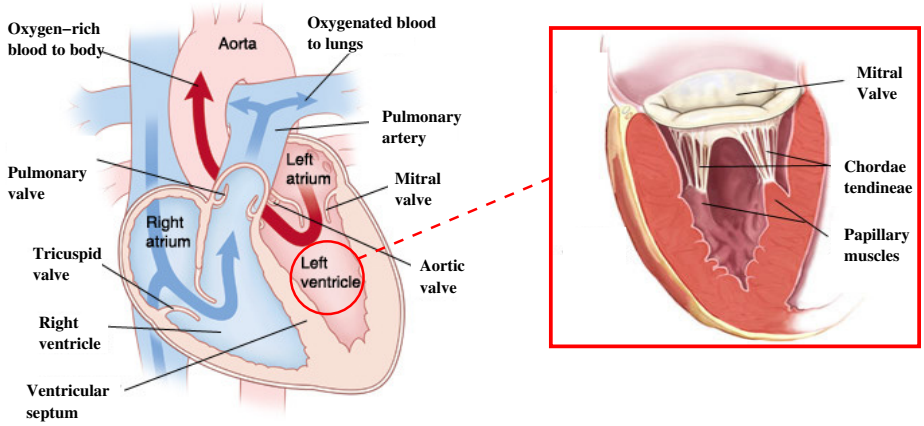

Figure 1.1: Schematic of the structure of the human heart, with its four chambers and valves. On the right a focus on the left ventricle is given.

Moreover these diseases, accounting for an estimated 17,3 of 54 million total deaths in 2013, corresponding to approximately $31,5\%$, are still considered the leading cause of death in developed countries.

Despite the effort in improving diagnostic procedures and intervention measures to reduce this rate of mortality, the predicted scenario does not present enhanced outcomes in the forthcoming years. In fact the occurrence of cardiovascular diseases has been proved to be strongly correlated with several risk factors, such as age, overweight and obesity, physical inactivity, diabetes smoking and tobacco use, whose incidence rate is going to show an increasing trend in the imminent future, as depicted in figure 1.2. Furthermore the high costs of such treatments, which in 2013 made cardiovascular diseases to have the greatest burden on total health expenditure around 14%, are projected to triple reaching almost an alarming trillion dollars by 2030.

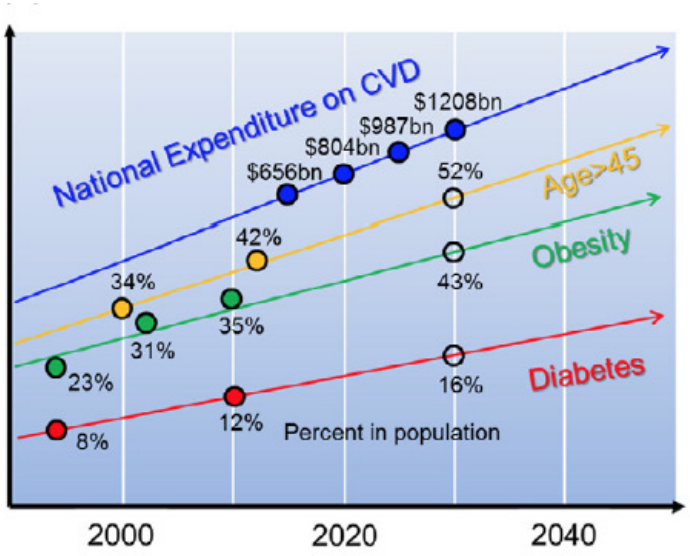

Figure 1.2: Trends of the main risk factors in cardiovascular diseases over the next decades (http://www.census.gov/population/age/ (Mittal *et al.*, 2016)).

This unfavourable prospected tendency needs to be reverted, starting from the research of new investigation tools and the development of new technologies able to improve treatment outcomes without concurrently increasing the cost of medical diagnosis and therapies. A significant change is being produced by the recent continuous progress of computational engineering: on one hand the medical community relies heavily on digital imaging techniques and computer aided procedures, on the other hand the unprecedented availability of fast and massively parallel computers allows for multi–physics computational models to be run on realistic configurations that are of direct interest for clinical application. The way it is going through is to develop a computational cardiovascular hemodynamics, meaning to realize a numerical model which could replicate cardiac pathologies and provide insights in order to alter their progress. There are several reasons to resort to computational modeling to study hemodynamics. First of all novel technological solutions, such as prostheses or surgical procedures, can be tested by simulations, thus avoiding the extensive use of hardware models or in vivo experiments on animals. Then computer simulations provide virtually unlimited access to hemodynamics data and dynamical features of the system that would be exceedingly difficult or even impossible to obtain otherwise. Finally from the huge time– and space–resolved database produced by a numerical simulation it is possible to synthetize all the signals of medical imaging (MRI, CT–scan, ultrasound), thus allowing to refine the diagnostic power of medical tools and to train medical doctors by virtual scans. With regard to computational modeling, it is useful to separate cardiovascular hemodynamics into cardiac hemodynamics and vascular hemodynamics. While the former relates to blood flow in the left and right ventricles and atria of the heart, the latter relates to the blood flow in the vessels which transports blood to and from these chambers to the rest of the body. It has to be highlighted that while the field of computational modeling of vascular hemodynamics has been extensively investigated by several studies and translated to clinical applications (Taylor *et al.*, 2013), cardiac hemodynamics still presents several challenging problems for its computational modeling that need to be addressed (Mittal *et al.*, 2016). Motivated by the above considerations, in this thesis we deal with computational modeling of cardiac hemodynamics. More precisely we decide to focus on the whole system of the left ventricle since, as mentioned above, it plays the most important and delicate role in all the cardiovascular system. The main challenges are related to the large scale motion and complex deformation of the entire structure, made by the valves and the ventricle itself, and also to the dynamics of the blood flow inside it owing to the interaction with valves. The main goal to address in order to construct a reliable model, which could be even taken advantage of by the medical community, is to provide a synergistic functioning of all elements, thus reflecting the real behaviour of the human heart.

1.2 State of the art and challenges in computational cardiac hemodynamics

The earliest computational modeling of cardiac hemodynamics can be traced back to Peskin in the first ’70; he developed a first two–dimensional model for the left ventricle using the immersed boundary method (IBM) introduced in

Peskin (1972). In this method, the flow was solved on a fixed Cartesian grid and elastic fibers immersed in the fluid grid were used to simulate the cardiac wall; these fibers moved with the local flow velocities and their effect was transmitted through a smooth delta–function to the fluid. However this function had the limitation of reducing the accuracy in resolving hemodynamics in proximity of the walls of the ventricle. Later Peskin and McQueen extended such a model in order to study three–dimensional cardiac flow inside the left ventricle (Peskin, 1977; Peskin & McQueen, 1989).

From then on the challenging field of cardiac hemodynamics has been investigated following essentially two different approaches in the modeling process: a patient–specific approach, based on medical imaging data, and a multi–physics approach, based on direct numerical simulations.

The former method intends to extract a realistic geometry of the heart over the entire cardiac cycle from high–resolution medical images (MRI, CT–scan, ECHO), then go back to the dynamics of the ventricle and finally run the fluid dynamics simulations. Earlier computational models based on this approach were quite simplified, supplying only the realistic shape of the ventricle without many surface details, and not including physical valves but simulating their presence prescribing ad–hoc boundary conditions (Saber *et al.*, 2003; Schenkel *et al.*, 2009). Later models were provided with better segmentation procedures, which enabled to improve previous deficiencies (Mihalef *et al.*, 2011). Despite this patient–specific approach appears to be a promising research field, whose great potentiality lies on the visual realism given by imaging techniques, it is still far from becoming a relevant numerical tool for the medical community: first of all because each simulated case is specific of a single person and cannot be generalized so easily; moreover until now this procedure has revealed itself to be very time consuming, thus not in compliance with required diagnostic timing.

The alternative approach does not start from medical imaging data but rather develops from scratch a geometry for the heart, even if more simplified than the real one, and use it as simulation set–up for modeling cardiac hemodynamics. In the last decade several research groups tackled this approach, but with the limitation of focusing each one separately on a specific component of the ventricle and making simplifying assumptions on boundary conditions related to other aspects. In Domenichini *et al.* (2005) they employed a simplified shape for the geometry of the left ventricle, like a prolate spheroid, with moving walls to study the dynamics of intraventricular flow during filling phase. The motion of the ventricle was imposed and forced to coincide with the wave–form profile of the incoming fluid. The formation and evolution of a vortex ring was investigated by varying governing parameters, and for all values a well–defined structure of vorticity was found out. The same research group also applied such a model to understand the effect of some ventricular pathologies like dilated cardiomyopathy (Baccani *et al.*, 2002) and myocardial infarction (Domenichini & Pedrizzetti, 2011) on the vortex formation and direction during filling phase. Some other works (Georgiadis & Pasipoularides, 1992; Nakamura *et al.*, 2003) paid specific attention to the flow structure inside the left ventricle. Later also Seo and Mittal performed direct numerical simulations to analyze the effect of intraventricular flow patterns on the pumping efficiency and the blood mixing of the left ventricle (Seo & Mittal,

2013). Their simulations indicated that intraventricular blood flow patterns have a physiologically insignificant effect on the pumping efficiency. However, diastolic flow patterns were recognized to influence the blood mixing as well as the residence time of blood cells in the ventricle.

Despite the useful insights all these works provided in studying cardiac flow, some relevant features like the simulation of the complete cardiac cycle (inflow/outflow) and the inclusion of valves inside the ventricle modeling were still missing. Furthermore a crucial point that needed to be addressed was the construction of a standing alone model, since in the human left ventricle the fluid (blood) and the structure (ventricle and valves) coexist and strongly interact among themselves. Considering only part of the entire system still led to oversimplified models which produced unsatisfactory results and, even worse, contributed to make the medical community sceptical with respect to the effectiveness of computational engineering and its applications. Including Fluid–Structure Interaction (FSI) procedure started to become a challenging but desirable result to achieve.

Regarding the modeling of left ventricle valves, but not yet accounting for the effect of the ventricle on them, two contributions have to be mentioned. For the aortic valve, direct numerical simulations of the pulsatile flow through a bileaflet mechanical valve were first carried out by de Tullio *et al.* (2009), under physiological conditions and in a realistic aortic root geometry. The motion of the valve leaflets was computed from the forces exerted by the fluid on the structure, considering both as a single dynamical system. He made use of the IBM, combined with a FSI algorithm, which turned out to be a reliable and accurate technique for such complex flows. On the other hand, almost concurrently, the first three–dimensional FSI model of the mitral valve including leaflets and chordae tendineae was presented by Kunzelman *et al.* (2007). Physiological valve was first assessed, then the leaflet and chordal strain and the papillary muscles force were determined. The obtained numerical results well agreed with a wide range of available in vivo and in vitro data.

The merit of integrating valves in the dynamics of intraventricular flow has to be attributed to Seo *et al.* (2014): they employed computational hemodynamics simulations to understand the effect of mitral valve leaflets on diastolic flow including the left ventricle geometry. In a perspective of modeling the synergistic functioning of the whole left ventricle, the choice of focusing on the mitral valve instead of the aortic one was dictated by the fact that, while the latter does not affect intraventricular flow as it operates passively, the former heavily influences it. Their simulations were performed with both a diode type valve model and a physiological one in order to asses the effect of mitral valve leaflets on the flow inside the ventricle. Their study suggested that a normal physiological mitral valve enforces the formation of a circulatory flow pattern in the ventricle; in addition its leaflets increase the strength of the apical flow, thus enhancing apical washout and mixing of ventricular blood. However, it has to be underlined that the leaflets motion was prescribed, thus the synergistic interaction between flow and structure dynamics was imposed rather than captured by the solution.

In this thesis we aim to go one step further and try to overcome such limitations. We propose to perform direct numerical simulations, with the least possible simplifying assumptions, provided with a full FSI algorithm to

couple flowing blood, left ventricle and mitral valve in such a way the dynamics of the whole system is univocally computed: the valve and ventricle dynamics are determined by their interaction with the flow which, in turn, depends on the motion of the structure. The numerical model, validated with an ad–hoc constructed experimental set–up (figure 1.3), seems to be able to replicate with high–fidelity the physical processes of such a complex system, thus resulting efficient and reliable.

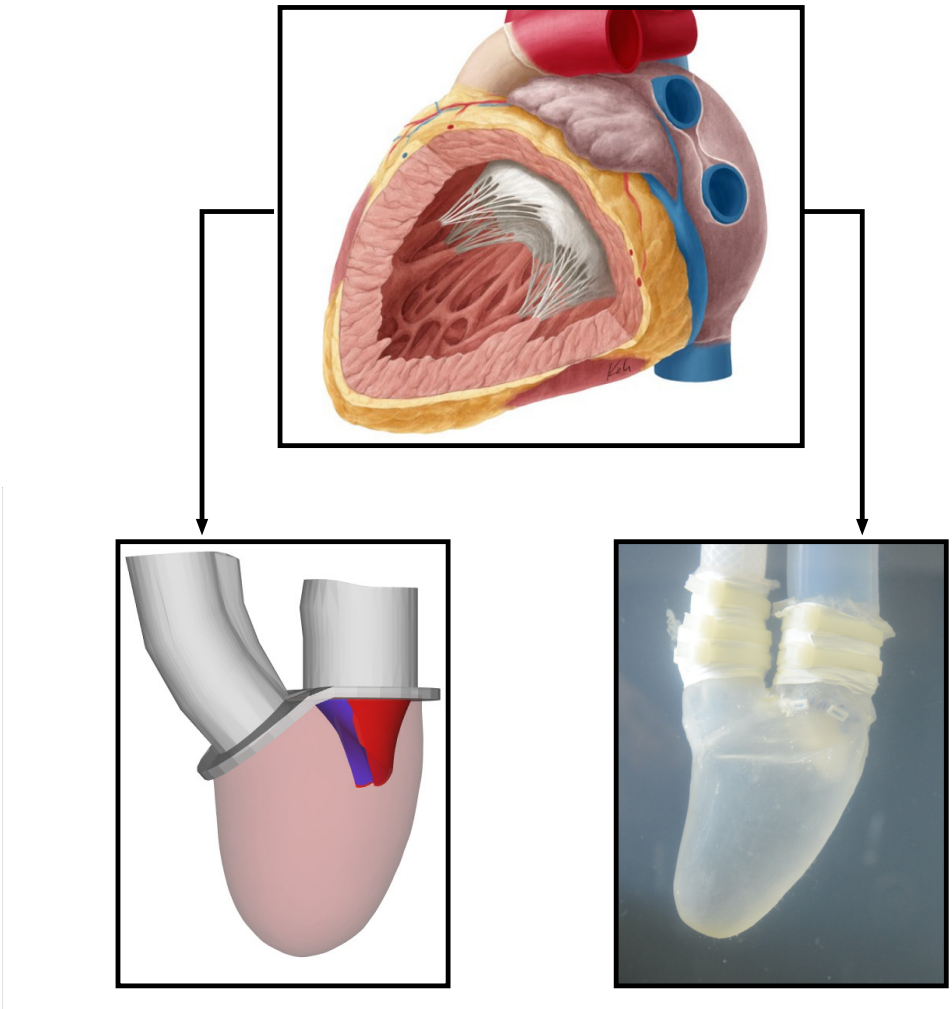

Figure 1.3: Two different approaches in facing the left ventricle modeling: (left) numerical simulations and (right) experimental measurements.

1.3 Governing equations and numerical details

The backbone of the computational model employed for numerical simulations in this thesis is a direct numerical simulation solver for the fluid dynamics. The motion of the blood, considered as an incompressible and viscous fluid, is described by the incompressible Navier–Stokes equations, which in non di-

mensional form read as follows

$$\begin{aligned} &\frac{\partial \mathbf{u}}{\partial t} + \mathbf{u} \cdot \nabla \mathbf{u} = -\nabla p + \nabla \cdot \boldsymbol{\tau} + \mathbf{f}, \\ &\nabla \cdot \mathbf{u} = 0, \end{aligned} \tag{1.1}$$

where $\mathbf{u}$ is the velocity; p is the pressure; $Re = UL/\nu$ is the Reynolds number defined from a characteristic length scale L, a velocity scale U and f is a specific body force term, linked to the immersed boundary technique, used to impose the correct boundary condition at the interface. Along the thesis the blood is assumed to be Newtonian meaning that the viscous term of equation (1.1) reads $\nabla \cdot \boldsymbol{\tau} = \nabla^2 \mathbf{u}/Re$, as it is known that its non–Newtonian nature strongly occurs only in vessels of diameter smaller than $15 - 20$ red blood cell diameters ($\sim 80 - 100\ \mu$m), (Siginer *et al.*, 1999), which is far from the ventricle case. However, since the non–Newtonian feature is implemented in the code, in chapter 3 it will be investigated and the numerical results obtained will be compared with the ones of the Newtonian model.

The spatial discretization of the Navier–Stokes equations is performed with an energy conserving second–order centered finite–difference scheme with velocities on a staggered grid; explicit Adams–Bashforth scheme is used to discretize the non–linear terms, while an implicit Crank–Nicholson scheme is used for the viscous terms. The resulting system leads to a large sparse matrix whose inversion is avoided by an approximate factorization and the sparse matrix is then transformed into three tridiagonal matrices (one for each direction) and solved using Thomas' algorithm. Time integration is performed via a self starting fractional step third–order Runge–Kutta (RK3) scheme. These schemes have already been tested and described extensively previously for a variety of flow related problems; thus we refer to Verzicco & Orlandi (1996) and van der Poel *et al.* (2015) for a detailed dissertation.

The integration of the Navier–Stokes equations on a complex geometry time–dependent domain with moving and deforming boundaries would be a formidable computational task without the help of the IBM. The great advantage of this approach is that it avoids body–fitted meshes, which on complex and deforming geometries would require difficult and computationally demanding procedures. Any boundary condition can be virtually applied at the immersed surface, still retaining the ease and efficiency of computational fluid dynamics in simple and structured meshes. The fundamentals of the IBM employed in this thesis can be found in Fadlun *et al.* (2000) and Vanella & Balaras (2009).

The structure configuration is solved by imposing the local instantaneous equilibrium between the inertia forces induced by the accelerations, the internal forces, the body forces and the external hydrodynamic loads, using a spring–mass model based on an interaction potential approach, firstly introduced in Fedosov (2010). The structure surface is discretized with triangular elements and the total mass is uniformly distributed on the vertices; then the total potential energy is computed and transformed into nodal force by applying first spatial derivative. The outcome is a system of ordinary differential equations that can be solved very efficiently even for a large number of structure elements in order to get the instantaneous structure configuration. All the details on this new approach will be given in the following chapters.

As already mentioned previously, a loose coupling FSI algorithm is implemented in order to simulate the synergistic working of all components, thus getting a reliable modeling of the whole left ventricle.

1.4 Outline of the thesis

The thesis is structured so that each chapter is self-consistent, basing on papers that have been already published, submitted or that are still in preparation. In details it is organized as follows.

In chapter 2, first we present the development of the structure of the computational model in all its parts from the description of the employed fluid solver to the detailed analysis of the new approach for the structural solver based on an interaction potential method. Moreover the IBM with the moving least squares interpolation and the coupling procedure of fluid dynamics and structure deformation are illustrated. Then we show two feasible applications of the model in two different research fields: the former is related to turbulence processes, proving how the interaction potential approach can be used to model liquid–liquid interface problems in order to study the deformation of drops/bubbles, coupling the flow with the interface morphology; the latter refers to cardiac hemodynamics of the left ventricle, investigating the interaction between flow dynamics and structure deformation both with numerical simulations and experimental validations.

In chapter 3, we investigate how the inclusion of three different types of mitral valve (natural, biological and mechanical prosthetic) influences left intraventricular flow, in both a physiological and a pathological case. In addition we assess their effectiveness in terms of hemodynamics performances in order to have clinical insights in the process of valve replacement.

In chapter 4, we enhance our computational model by adding chordae tendineae to natural mitral valve in order to evaluate how their physical presence differently affects the flow dynamics inside the left ventricle with respect to the non chorded case. Although it implies a substantial increase in numerical and modeling complexity, this procedure avoids the use of numerical constraints to mimic their functionalities and allows to achieve a much more realist description of the interaction between fluid and structure.

In chapter 5, we give a medical application of our numerical model, by studying the cardiac pathology of hypertrophic cardiomyopathy. First we aim to replicate the patho–physiology of the disease; then we perform a parametric study of different severity levels of hypertophy of the left ventricle to assess clinical risks involved to each one; finally we simulate the surgical procedures of leaflets plication and septum myectomy in order to give insights on the efficiency and reliability of such intervention measures.

In chapter 6, we conclude our dissertation with a summary of the main contributions achieved and an overview on the ongoing works and future perspectives.

Chapter 2

A parallel interaction potential approach coupled with the immersed boundary method for deformable interfaces and membranes

Based on: Vamsi Spandan, Valentina Meschini, Rodolfo Ostilla–Monico, Detlef Lohse, Giorgio Querzoli, Marco D. de Tullio & Roberto Verzicco, 'A parallel interaction potential approach coupled with the immersed boundary method for deformable interfaces and membranes', *Journal of Computational Physics*, 348, 567-590, 2017.

2.1 Introduction

The interaction between fluid flow and an immersed elastic body (fluid or solid) has been studied extensively over the last few decades due to its wide range of applications, for example, bubbles and drops dispersed in a turbulent flow (Balachandar & Eaton, 2010; Tryggvason *et al.*, 2013), red blood cells flowing through blood vessels (Freund, 2014), pumping motion of ventricles and valves in the heart (Mittal *et al.*, 2016; Sotiropoulos *et al.*, 2016), oscillation of large structures such as aircraft wings and high–rise buildings (Dowell *et al.*, 2004). While the source of elasticity of the immersed body in each of these phenomena is different, the interplay between a deformable body and a surrounding inhomogeneous time dependent flow can result in a complex non–linear system where they determine each other's behaviour in a coupled manner. In addition the presence of multiple bodies with different static and dynamic properties interacting with each other gives rise to a wide range of control parameters which makes these systems extremely challenging to study. Over the last few decades tremendous amount of effort has been devoted to the modeling and simulation of such systems which are often classified in literature as fluid–structure interaction (FSI) problems. Among a variety of techniques developed to tackle FSI problems, the immersed boundary method (IBM) (Mittal & Iaccarino, 2005; Peskin, 1972, 2002) has gained immense popularity and has been instrumental in making efficient and accurate simulations of several complex flow systems possible; for example cardiac and vascular hemodynamics (Mittal *et al.*, 2016; Sotiropoulos *et al.*, 2016), suspensions of rigid spheres (Fornari *et al.*, 2016; Picano *et al.*, 2015; Prosperetti, 2015; Uhlmann & Doychev, 2014), deformable bubbles or drops (Schwarz *et al.*, 2016), vehicle aerodynamics (Iaccarino & Verzicco, 2003; de Tullio *et al.*, 2011*b*) etc.

One of the biggest advantages of IBM is that it relies on the use of a single underlying mesh for the fluid flow (hereafter referred to as Eulerian mesh) which does not have to conform/adapt with the moving/deforming immersed body (Mittal & Iaccarino, 2005; Peskin, 1972, 2002). This eliminates the complex and computationally expensive procedure of Eulerian mesh regeneration every time step as the immersed body moves or deforms, resulting in the decoupling of the mesh required for the flow solver from the position and morphology of the immersed body. The surface of the immersed body is discretized independently of the Eulerian mesh and is often called a Lagrangian or a structural mesh. The influence of the immersed body on the flow can be achieved through a volume averaged body force in the fluid governing equations after a careful transfer of information between the Eulerian and Lagrangian meshes. Moreover the time invariant nature of the Eulerian mesh makes IBM promising for parallelization on multiple distributed memory computing processors and this has led to breakthroughs in simulations of highly turbulent flows around complex geometries. However, the inclusion of deformability into the immersed boundary framework to study the motion of liquid–liquid interfaces or elastic membranes is not straightforward and this is the focus of this chapter.

In the field of multiphase flows several techniques have been developed to understand the motion and influence of particles, drops or bubbles in a turbulent flow (e.g. point–particle, volume of fluid, level–set, front tracking)

(Prosperetti & Tryggvason, 2007). When the inherent surface tension forces in the bubbles or drops are not strong enough, they deform according to local flow conditions and also alter them simultaneously. The challenge in direct numerical simulations of such flows arises from the wide range of length, time scales and regimes involved (Crowe *et al.*, 1996; Magnaudet & Eames, 2000; Tryggvason *et al.*, 2013). Numerically handling a sharp boundary between different phases and the singularity of the surface tension term in the governing equations is non–trivial (Scardovelli & Zaleski, 1999). Additionally, since the density is not uniform in the flow domain, the pressure cannot be computed using fast Poisson solvers, but through relatively slower iterative methods. The complex algorithms and procedures put in place to tackle the above mentioned issues have restricted the scale of multiphase flows that can be studied; for example, state of art parallel simulations can only reach up to $O(10^2)$ deformable drops/bubbles in a reasonably turbulent flow (Tryggvason *et al.*, 2013). In order to scale up numerical simulations of dispersed multiphase flows, there is a need for development of alternative methods are relatively computationally inexpensive and still account for the various active physical mechanisms in the flow.

In the first part of this chapter we show the validity and use of a new phenomenological approach to replicate the deformation of closed liquid–liquid interfaces under given flow conditions. The main advantage of this approach is the computationally inexpensive nature of the deformation algorithm which allows for simulations of large scale dispersed multiphase flows. The deformability of any immersed drop or bubble is replicated by solving for the dynamics of a three–dimensional spring network spread over its surface. Hereafter we refer to this technique as the interaction potential (IP) model. The Navier–Stokes equations which govern the fluid motion inside and around the immersed body are solved using direct numerical simulations (DNS), while IBM is used to enforce the interfacial boundary conditions (for example no–slip or free–slip). Thus the fluid motion and the effect of an immersed interface on the flow is fully resolved, while the deformability is captured through a stable, versatile, easy to implement and computationally inexpensive IP model. In later sections we will further discuss why the IP model is able to sufficiently replicate the dynamics of deforming liquid–liquid interfaces. This model has been used previously by de Tullio & Pascazio (2016) within the immersed boundary framework to simulate elastic bodies with arbitrary thickness, such as flapping flags, leaflets of heart valves, thin elastic sheets.

In the second part of this chapter we show how this approach can be extended to more complex FSI problems by performing a three dimensional simulation of the flow in the left heart ventricle with mechanical and biological valves. In particular, we focus on the simulation of the left ventricle of the human heart along with a physical mitral valve in both pathological and physiological conditions. IBM has been a front runner in the field of cardiovascular hemodynamics, as it has been evidenced in several previous studies (Choi *et al.*, 2015; Seo & Mittal, 2013; Seo *et al.*, 2014, 2013; de Tullio *et al.*, 2011*a*, 2009; Vedula *et al.*, 2014; Zheng *et al.*, 2012). A main impulse in developing this research field from a computational fluid dynamics point of view is the increasing demand from the medical community for scientifically rigorous and quantitative investigations of cardiovascular diseases. Again, the major bot-

tleneck in conducting fully resolved simulations of the complete human heart is created by the complex deformation dynamics of the various ventricles and valves which interact with the pulsatile blood flow (Mittal *et al.*, 2016).

Various approaches have been employed over the years to achieve realistic and reliable cardiac hemodynamic simulations. One approach is to use available models of the heart functionality along with the biophysical component of cardiac electromechanics. This has been used in the 'Living Heart Project' (Baillargeon *et al.*, 2014), where a fully coupled electro–mechanic and hemodynamic simulation is realised, and more recently by Choi *et al.* (2015), who coupled a multi scale model for electromechanics with the Navier–Stokes equations for the flow dynamics. Zheng *et al.* (2012) and Seo & Mittal (2013) focused on intraventricular flow and the accompanying pathologies under the effect of a diastolic flow pattern, while Seo *et al.* (2014) studied the effect of the mitral valve on the flow dynamics. In all these simulations the deformation cum motion of the left ventricle and the valves are imposed either through kinematic models or derived through imaging, but not through a fully coupled FSI simulation. The motivation in employing kinematic models to describe the motion of ventricles and valves instead of a full FSI simulation is to eliminate the massive computational cost in solving the three dimensional Cauchy–Navier equations for the immersed elastic body along with the Navier–Stokes equations. Although numerical simulations with predefined ventricle/valve motion is a challenging task in itself, in reality the motion of the ventricle and the valves, and the fluid are coupled to each other and can govern each other's motion.

The FSI simulation of the left ventricle with a physical valve, which is described in detail later, is performed within the equivalent of 48 CPU hours on a single processor with an Eulerian grid of 150x150x150 and a Lagrangian mesh of approximately 50000 elements on the ventricle which shows the computationally inexpensive nature of the IP approach. Moreover these simulations were compared and validated with in–house ad–hoc laboratory experiments to ensure the reliability of the results. While we do not solve for computationally challenging coupled three dimensional Navier–Stokes Cauchy–Navier equations, we take a step further from employing kinematic models towards having full FSI between the flow, the ventricle and the mitral valve. In order to further throw light on the computational time gained by the IP approach, a relatively simpler problem of flow across an aortic valve within a deformable aortic root which used 10^6 nodes for the fluid solver and 10^3 triangular elements for the structure (de Tullio *et al.*, 2011*a*) required the same computational time as that of the IP approach to model the full left ventricle with physical mitral valve. In comparison to the FEM solver, the IP approach needs only 3% of the CPU time per time step for the structural solver.

The IBM described in this chapter makes use of the moving least squares (MLS) approximation which is crucial when the system involves moving and deforming boundaries. However, the computational cost of MLS increases rapidly with increase in the resolution of the immersed bodies. New algorithms or a parallel implementation of the computation on distributed memory processors thus become an invaluable tool in scaling up fully resolved flows interacting with several moving/deforming immersed bodies. In particular, parallelization is an attractive prospect given the increasing availability of cost–

efficient high performance computing facilities. A parallel implementation of a flow solver involving multiple deforming bodies is not a straightforward task due to many algorithmic complexities. The challenge lies underneath the fact that two different meshes (Eulerian and Lagrangian) are required for the complete solution and different parallelization strategies would be required to make use of multiple processors effectively.

In the last part of the chapter we describe a parallelization scheme designed to track the time evolution of several deformable bodies (e.g. vesicles, drops, biological tissues) immersed in turbulent flows. This strategy is built upon the already underlying parallelization scheme implemented for the fluid solver, thus reducing the downtime of overall code development. In particular, the benefits of the parallelization is oriented towards simulation of dispersed phase systems with several thousand deforming drops, bubbles, vesicles or bodies moving in a highly turbulent carrier fluid phase.

The novelty of the current work is threefold. We first discuss the extension of the algorithm to liquid–liquid interfaces which is not straightforward. From a theoretical point of view we take advantage of the fact that the deformation of any immersed interface or membrane are both based on the fundamental principle of minimum potential energy. This has not been taken advantage of in its full extent for liquid–liquid interfaces in previous works and, given its computational efficiency and ease of implementation, it can be extremely beneficial for studies involving large scale dispersed multiphase flows where traditional techniques become too expensive. We also demonstrate that the method is extremely versatile and that the approach can not only handle simple elastic structures but also tackle complex FSI problems; for example flow in the left heart ventricle with mitral valves. This is a step forward in the field of cardiovascular simulations where the conventional approach is to derive the motion of the ventricle from kinematic models or imaging techniques. Although this approach is computationally inexpensive, parallelization is inevitable for handling thousands of immersed bodies in a turbulent flow, which is discussed in the last part of the chapter.

In the next section we give an overview of the governing equations for the solution of the fluid phase, implementation of the IBM using MLS and the interaction potential approach for computing the deformation of elastic bodies. In section 3, we show how the interaction potential approach can be used to study deformation of drops/bubbles where the flow is dynamically coupled with the interface morphology. These results are validated with analytical solutions and experimental measurements taken from literature. In section 4, we describe the simulation of the full left ventricle with both mechanical and natural mitral valves in addition to comparing the results from our simulations with ad–hoc in–house experiments. In section 5, we discuss the data structures required and also the parallelization strategy to scale up the problem to study several thousand deforming immersed bodies. Finally, we provide a summary and outlook in section 6.

2.2 Governing equations and numerical scheme

2.2.1 Fluid phase

For the fluid phase we solve the Navier–Stokes equations governing incompressible flow in a Cartesian box as given in equations (2.1). In the following text, velocity and force fields on the Lagrangian and Eulerian meshes are represented by upper case and lower case symbols, respectively.

$$\begin{aligned} &\frac{\partial \mathbf{u}}{\partial t} + \mathbf{u} \cdot \nabla \mathbf{u} = -\nabla p + \frac{1}{Re} \nabla^2 \mathbf{u} + \mathbf{f}, \\ &\nabla \cdot \mathbf{u} = 0. \end{aligned} \tag{2.1}$$

Reynolds number of the flow is defined based on a characteristic length scale L and velocity scale U as $Re = UL/\nu$, where ν is the kinematic viscosity of the fluid. $\mathbf{u}$, p are the velocity and pressure in the flow, while $\mathbf{f}$ is the volume averaged force arising from the IBM and is included to enforce the interfacial boundary condition.

A conservative second–order centered finite–difference scheme with velocities on a staggered grid is used for spatial discretization; explicit Adams–Bashforth scheme is used to discretize the non–linear terms, while an implicit Crank–Nicholson scheme is used for the viscous terms. Treating all the viscous terms implicitly results in a large sparse matrix which is avoided by an approximate factorization of the sparse matrix into three tridiagonal matrices (one for each direction) which are solved using Thomas' algorithm. Time integration is performed via a self starting fractional step third–order Runge–Kutta (RK3) scheme. The pressure required to enforce mass conservation is computed by solving a Poisson equation for a pressure correction. The code for single phase flows has already been tested extensively in previous studies for a variety of flow configurations and additional details of the numerical scheme can be found in Rai & Moin (1991), Verzicco & Orlandi (1996) and van der Poel *et al.* (2015).

2.2.2 Dispersed phase: immersed boundary method

We now describe the procedure of constructing the Lagrangian mesh and the schemes used to transfer flow quantities between the Lagrangian and Eulerian mesh which is a crucial ingredient in IBM. The details of the methodology are reported in de Tullio & Pascazio (2016) and are included here for convenience. In figure 2.1 we show a schematic of the various Lagrangian meshes used in this study. Any given surface (closed or open) is discretized into triangular elements where each element is composed of three vertices (v_1, v_2, v_3) which are connected by edges (e_1, e_2, e_3). Under the condition that the mass is uniformly distributed on the triangular element, the position of the centroid (c_1) of each triangular element is computed based on the coordinates of the vertices. Figure 2.1a shows a sphere discretized into triangular elements along with a schematic showing the composition of each triangle. In figure 2.1b we can see the discretized geometry of the left ventricle and figure 2.1c shows the remaining auxiliary components.

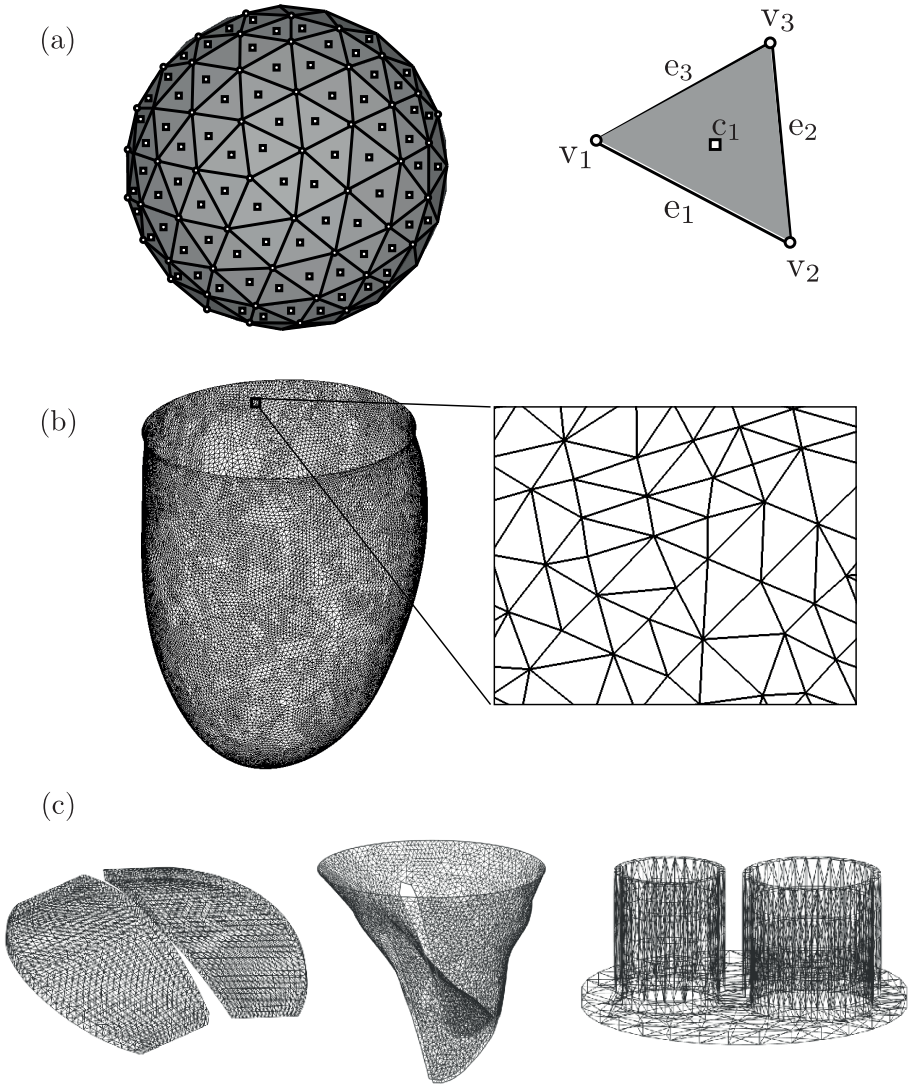

Figure 2.1: Schematic of the Lagrangian mesh. a) A sphere discretized using triangular elements; on the right a single triangular element is decomposed into three vertices v_1,v_2,v_3 (circles), three edges e_1,e_2,e_3 and one centroid c_1 (square). b) Full structure of the left ventricle with a zoomed–in area showing the triangulated network. c) Rest of the components of the full left ventricle structure; the left panel shows the leaflets of prosthetic mechanical mitral valve, the middle panel shows the natural mitral valve and the right panel the channels for mitral and aortic valves.

Following the idea of Uhlmann (2005) the force required to enforce the interfacial boundary condition is first computed on markers laid out on the Lagrangian mesh and then transferred to the Eulerian mesh. Here we consider the triangle centroids to be the Lagrangian markers, which are responsible for enforcing the interfacial boundary condition. The vertices and edges of the discretized triangular elements play a role in the deformation dynamics and will be explained later.

The next step is to build a transfer function around each Lagrangian

marker (here the centroid c_i) which would be used to exchange information between the Eulerian and Lagrangian mesh. As noted previously, we adopt the MLS approach (Lancaster & Salkauskas, 1981; Liu & Gu, 2005), which is part of the class of meshless approximations and has been used previously in several fields such as element free Galerkin methods (Atluri *et al.*, 1999; Belytschko *et al.*, 1994, 1996; Hegen, 1996; Krongauz & Belytschko, 1996), computer graphics (Fleishman *et al.*, 2005; Kobbelt & Botsch, 2004; Kolluri, 2008; Schaefer *et al.*, 2006; Zeng & Lu, 2004), and also recently for IBM (de Tullio & Pascazio, 2016; Vanella & Balaras, 2009). In order to compute this transfer function we first need to build a support domain centered around each Lagrangian marker which consists of all Eulerian grid nodes closer than a threshold value in each direction. By taking a threshold value of $r_i = 1.5\Delta x_i$ in each direction, a three–dimensional support domain consisting of $N_e = 27$ (3x3x3) Eulerian nodes is built around each Lagrangian marker. In figure 2.2a we show a schematic of a two dimensional support domain consisting of nine Eulerian cells around the centroid c_1. The next step is to use these Eulerian cells and build a transfer function through which any quantity q_i defined on the Eulerian nodes can be interpolated on the Lagrangian marker (i.e centroid of each triangular element). The same transfer function can be used to extrapolate the force computed on the Lagrangian markers (F_i) to the Eulerian mesh (f_i).

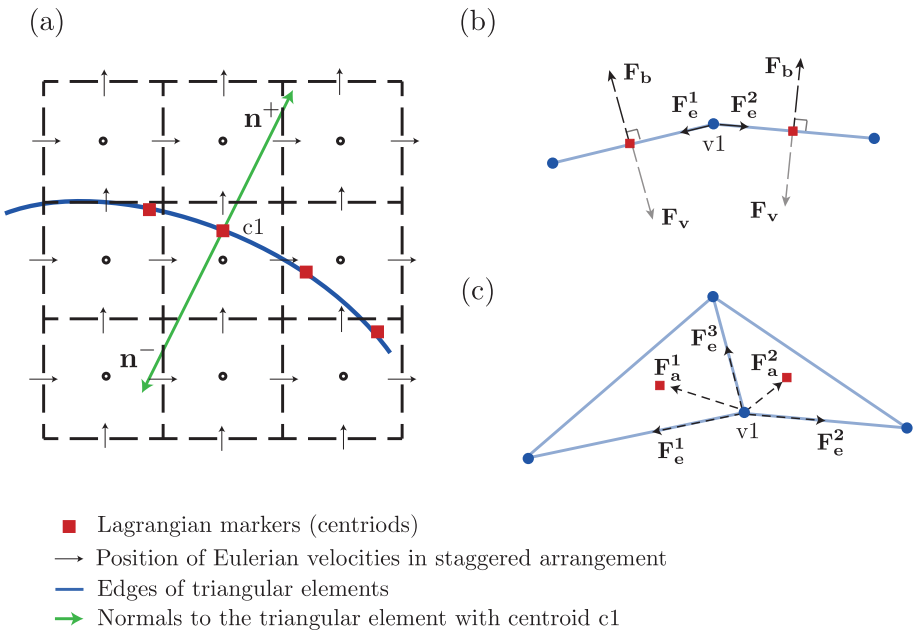

Figure 2.2: a) Schematic of a two–dimensional support domain around the centroid c_1 (red squares) consisting of nine Eulerian cells; arrows show the position of Eulerian velocities in a staggered formation. b), c) Schematic of the direction of the various elastic forces acting on the triangular elements.

The MLS interpolation of q_i at a Lagrangian marker (c_i) is defined as follows

$$Q_i(\boldsymbol{x}^l) = \boldsymbol{p}^T(\boldsymbol{x}^l)\boldsymbol{a}(\boldsymbol{x}^l) = \sum_{j=1}^{m} p_j(\boldsymbol{x}^l)a_j(\boldsymbol{x}^l),$$

where Q_i is the quantity interpolated on the Lagrangian marker, while $\boldsymbol{p}^T(\boldsymbol{x}^l)$ is a basis function vector with dimension m. $\boldsymbol{x}$ is the position vector of the Lagrangian marker. In this work we consider a linear basis function with $\boldsymbol{p}^T(\boldsymbol{x}^l) = [1, x, y, z]$, i.e. $m = 4$, which is cost–efficient and also able to represent the gradients in the Eulerian field with second order accuracy. $\boldsymbol{a}(\boldsymbol{x}^l)$ is the vector of coefficients obtained by minimizing the weighted L2 norm J as follows

$$J = \sum_{k=1}^{N_e} W(\boldsymbol{x}^l - \boldsymbol{x}^k)[\boldsymbol{p}^T(\boldsymbol{x}^k)\boldsymbol{a}(\boldsymbol{x}^l) - q_i^k]^2. \tag{2.2}$$

Here $W(\boldsymbol{x}^l - \boldsymbol{x}^k)$ is a weight function; we use the exponential weight function which is given as follows

$$W(\boldsymbol{x}^l - \boldsymbol{x}^k) = \begin{cases} e^{-(r_k/\alpha)^2} & r_k \leq 1, \\ 0 & r_k > 1, \end{cases}$$

where α is a constant of shape parameter and r_k is given by

$$r_k = \frac{|\boldsymbol{x}^L - \boldsymbol{x}^k|}{r_i},$$

where r_i is the size of the support domain in the i^{th} direction as defined previously. Other commonly used shape functions are the cubic spline and quadratic spline functions and a spline function with any order of continuity can be constructed using the steps detailed in Liu & Gu (2005). Minimizing J in equation (2.2) leads to $\boldsymbol{A}(\boldsymbol{x}^l)\boldsymbol{a}(\boldsymbol{x}^l) = \boldsymbol{B}(\boldsymbol{x}^l)\boldsymbol{q}_i^k$ where

$$\boldsymbol{A}(\boldsymbol{x}^l) = \sum_{k=1}^{N_e} W(\boldsymbol{x}^l - \boldsymbol{x}^k)\boldsymbol{p}(\boldsymbol{x}^k)\boldsymbol{p}^T(\boldsymbol{x}^k),$$

$$\boldsymbol{B}(\boldsymbol{x}^l) = [W(\boldsymbol{x}^l - \boldsymbol{x}^1)\boldsymbol{p}^T(\boldsymbol{x}^1)...W(\boldsymbol{x}^l - \boldsymbol{x}^{N_e})\boldsymbol{p}^T(\boldsymbol{x}^{N_e})],$$

$$\boldsymbol{q}_i = [q_i^1...q_i^{N_e}]^T.$$

Combining all the above equations, the interpolated quantity Q_i can be expressed as follows

$$Q_i(\boldsymbol{x}^l) = \boldsymbol{\phi}^T(\boldsymbol{x}^l)\boldsymbol{q}_i = \sum_{k=1}^{N_e} \phi_k^l(\boldsymbol{x}^l)q_i^k \tag{2.3}$$

where $\boldsymbol{\phi}^T(\boldsymbol{x}^l) = \boldsymbol{p}^T(\boldsymbol{x}^l)\boldsymbol{A}^{-1}(\boldsymbol{x}^l)B(\boldsymbol{x}^l)$ is the transfer function containing the shape function coefficients for each Lagrangian marker. This shape function is used to interpolate the value of the intermediate Eulerian velocity $\hat{u}_i$ at the exact location of all Lagrangian markers and the volume force in each direction is calculated as $F_i = (V_i^b - U_i)/\Delta t$, where V_i^b is the desired velocity boundary condition on the Lagrangian marker (c_i) and U_i is the Eulerian flow velocity interpolated on the Lagrangian marker using MLS. Under the assumption of a no–slip boundary condition on the interface, the desired velocity V_i^b is

equal to the velocity of the corresponding centroid. This force needs to be transferred back to the Eulerian mesh using the same transfer function built for interpolation in equation (2.3) under the constraint that the total force is conserved during the extrapolation. The force to be included in the Eulerian mesh is written as $f^k_{b,i} = \sum_{k=1}^{N_L} c_l \phi^L_k F^L_i$, where N_L is the number of Lagrangian markers associated with a Eulerian point k. c_l is a scaling factor obtained by imposing the condition that there is no net–gain/loss in the IBM force while transferring flow information from the Lagrangian mesh to the Eulerian mesh which results in the following

$$c_l = \frac{\Delta V^l}{\sum_{k=1}^{N_e} \phi^l_k \Delta V^K},$$

where ΔV^L is the forcing volume associated with each Lagrangian marker and is computed as $\Delta V^l = A_l h_l$. A_l is the area of the triangular element associated with the Lagrangian marker (area composed by v_1, v_2, v_3 in figure 2.1) and $h_l = 1/3 \sum_{k=1}^{N_e} \phi^L_k (\Delta x^k + \Delta y^k + \Delta z^k)$. ΔV^k is the volume of the Eulerian cell k involved in the support domain. Here it is important to note that the transfer functions built using this approach conserves momentum on both uniform and stretched grids while reasonable accuracy is retained for torque equivalence on slightly stretched grids (de Tullio & Pascazio, 2016; Vanella & Balaras, 2009). For example, Vanella & Balaras (2009) report that with 10 % grid stretching, the net loss/gain in torque conservation is less than 0.5 %.

The calculation of hydrodynamic forces (pressure and viscous stresses) acting on the surface of any dispersed body in an IBM simulation is not straightforward as the Lagrangian and the Eulerian meshes do not necessarily align with each other at a given time instant. Since the surface of the dispersed bodies are discretized using triangular elements, the local pressure and viscous forces are first computed on the Lagrangian markers (centroids of triangular elements); the total external force on a triangular element with area A_l and surface normal $\boldsymbol{n}_l$ is calculated as $\boldsymbol{F}^l_{\text{ext}} = (-p_l \boldsymbol{n}_l + \boldsymbol{\tau}_l \cdot \boldsymbol{n}_l) A_l$. To evaluate p_l and τ_l, which are the pressure and viscous forces acting on a triangular element l, respectively a probe is sent along the normal of each triangular element with its centroid as the origin. The length of the probe h_l is equal to the mean local grid size and the MLS interpolation described above is used to interpolate both pressure and velocity gradients at the end point of the probe. The velocity gradients can also be computed from the derivatives of the shape functions (Liu & Gu, 2005). The value of the pressure gradient along this normal is computed from the momentum equation normal to the triangular element which gives $\frac{dp}{dn} = -\frac{D\boldsymbol{U}_L}{dt} \cdot \boldsymbol{n}_L$. The pressure on the Lagrangian marker (centroid) is then computed as follows

$$p_l = p^*_l + h_l \frac{D\boldsymbol{U}_l}{Dt} \cdot \boldsymbol{n}_l,$$

where p^*_l is the pressure at the probe endpoint and $\frac{D\boldsymbol{U}_l}{Dt}$ is the acceleration of the Lagrangian marker (de Tullio & Pascazio, 2016; Vanella & Balaras, 2009; Yang & Balaras, 2006). The shear stress $\boldsymbol{\tau}_l$ on the Lagrangian marker is computed based on the velocity gradients interpolated at the probe endpoint. This holds true under the assumption that the velocity of the fluid near the surface of the body varies linearly. An important note here is that when the

nature of the immersed body is such that fluid loads on either side of the interface are relevant, the pressure and viscous forces need to computed on both sides of the surface thus requiring two probes sent along the normal to every triangular element, one each along the positive and negative normal, respectively i.e. $\boldsymbol{F}^l_{\text{ext}} = [(-(p_l^+ - p_l^-)\boldsymbol{n}_l^+ + (\boldsymbol{\tau}_l^+ - \boldsymbol{\tau}_l^-) \cdot \boldsymbol{n}_l^+)]A_l$; the subscripts $^+$ and $-$ represent quantities evaluated on the end points of the probe on either side of the surface (de Tullio & Pascazio, 2016; Vanella & Balaras, 2009; Yang & Balaras, 2006).

2.2.3 Interaction potential approach for deformation

As mentioned above, the dynamics of deformation is computed based on a minimum energy concept which we describe here briefly. The surface of any immersed body is first discretized using triangular elements (see figure 2.1) the edges of which are composed of hypothetical linear/non–linear springs thus resulting in a two–dimensional network of springs. Under the influence of external forces such as pressure fluctuations or viscous stresses, the spring network undergoes deformation thus storing potential energy into the system. The potential is converted to nodal forces acting on individual triangular vertices by differentiating the potentials with respect to its corresponding displacement. The force acting on each triangular vertex is converted into an acceleration and integrated based on Newton's second law of motion. The position of each individual vertex is then accordingly.

The first form of potential is the in–plane elastic potential (W_e) which comes from the work done by an external force parallel to the plane of a triangular face and is converted into elastic energy stored into every spring connecting the triangle. We also consider an out–of–plane deformation (W_b) for which the total potential is computed based on a bending spring connecting the centroids of two adjacent triangular faces. This out–of–plane bending potential is stored in a pair of two faces sharing an edge and is a function of the contact angle between them. Additional potentials can be included which constrain the geometrical properties of the overall immersed body. For example, we can include a volume or area potential (W_v or W_a) which is a function of the change in volume/area of a single element with respect to an initial reference state. All the individual potentials are formed as given in the following equations

$$W_e = \frac{1}{2} k_e \boldsymbol{x}^2 \tag{2.4}$$

$$W_b = k_b(1 - cos\theta) \tag{2.5}$$

$$W_v = \frac{1}{2} k_v \left(\frac{V - V_0}{V_0} \right)^2 V_0 \tag{2.6}$$

$$W_a = \frac{1}{2} k_a \left(\frac{A - A_0}{A_0} \right)^2 A_0 \tag{2.7}$$

In the above equations, k_e, k_b, k_v, and k_a are the elastic constants for in–plane deformation, out–of–plane deformation, volume constraint and area constraint potentials, respectively. $\boldsymbol{x}$ is the change in length of a single edge; θ is the angle between the normals of two triangular faces sharing an edge; V_0, V and

A_0, A are the corresponding reference and deformed volumes and areas of each triangular element, respectively. While the equations (2.4)–(2.7) can be used to simulate homogeneous isotropic materials, the interaction potential approach can also used for inhomogeneous anisotropic materials by changing the functional form of the elastic potentials (de Tullio & Pascazio, 2016).

In figure 2.2bc we show a 2D and 3D schematic, respectively of the forces originating from these potentials on the vertices of the triangular elements. $\boldsymbol{F}_e$ is the in–plane elastic force and it acts along the edges connecting two vertices; $\boldsymbol{F}_b$ and $\boldsymbol{F}_v$ are the out of plane bending and volume constraint forces which act along the normal at the centroids of each triangular element. $\boldsymbol{F}_a$ is the force originating from the area constraint potential and is directed towards the centroid of the triangular element.

Once the forces on each of the triangular vertices are known, individual nodes are moved based on the equation $m\ddot{\boldsymbol{x}}^{\mathrm{v}_i} = F_{\mathrm{ext}}^{\mathrm{v}_i} + F_{\mathrm{int}}^{\mathrm{v}_i}$; $F_{\mathrm{ext}}^{\mathrm{v}_i}$ and $F_{\mathrm{int}}^{\mathrm{v}_i}$ are the external and internal forces acting on the triangular node v_i, $\ddot{\boldsymbol{x}}$ and m are the acceleration and mass of individual nodes. In the previous section F_{ext} was calculated on the centroid of each triangle. This force is transferred to an individual triangular vertex as $F_{\mathrm{ext}}^{\mathrm{v}_i} = \sum_{j=1}^{\mathrm{n}_{fi}} (1/3) F_{\mathrm{ext}}^{\mathrm{c}_j}$; where n_{fi} is the number of faces each vertex is connected to and $F_{\mathrm{ext}}^{\mathrm{c}_j}$ is the external force computed on the triangle centroid (Lagrangian marker) c_j. The calculation of m, which is the mass of individual triangular node is straightforward for surfaces made of materials where the density and thickness is known a priori. In cases where the immersed bodies are drops or bubbles, calculating m of the triangular nodes becomes tricky as there is no physical definition of the density and thickness of a liquid–liquid interface. In such a case m of the triangular nodes becomes a free parameter and to overcome this we fix the value of $m = 1$ and then correspondingly tune the elastic constants. This is detailed more in the next section.

Computing the individual potentials according to equations (2.4)–(2.7) in the interaction potential approach requires selection of several parameters (k_e, k_b, k_v, k_a). Once again, this step is straightforward for membranes where the elastic moduli are already known (de Tullio & Pascazio, 2016). In a later section where we show simulations of flow in the heart ventricle we will further show how we compute the elastic constants from the physical properties of the material that is used. In addition it is important to note that when the surface is discretized with non–uniform triangles such that the lengths of the edges of triangle vary, k_e should be computed based on the model proposed by Van Gelder (1998). This is to ensure that at the rest state of the elastic structure the properties of all the springs connecting the vertices are equivalent. On the other hand, simulating liquid–liquid interfaces using the interaction potential approach would require the use of ad–hoc elastic constants as again there is no direct physical correlation between the elastic constants and the surface properties of a liquid–liquid interface. The procedure of estimating these ad–hoc elastic constants will be described in detail in the next section.

Here it is important to note that modeling an elastic membrane or an interface using the interaction potential approach is a discrete formulation of the elasticity governing equations and thus a simplification of the existing continuum models. It has been shown in previous studies that through a careful

design of the spring network and the selection of appropriate elastic constants the mechanics of several elastic membranes can be exactly reproduced (Chen & Boyle, 2014; Fedosov *et al.*, 2010; de Tullio & Pascazio, 2016). While such a formulation is useful and necessary for complex simulations of several immersed deformable bodies owing to its simplicity and lower computational cost, it has its limitations. In particular for liquid–liquid interfaces, when the drops/bubbles deform to such an extent that they approach the critical Capillary/Weber number for breakup, the Lagrangian resolutions become terminally high. Such scenarios are better handled with techniques such as VOF or level set. When the Capillary/Weber numbers for the drops/bubbles are well below their breakup limit, the IP model provides a viable alternative to simulate large scale dispersed multiphase flows with realistic computational expenses. Here we would like to note that the derivation of the interaction potential approach is not unique to this work and variants of this method have already been used previously to predominantly study red blood cells (Chen & Boyle, 2014; Dupin *et al.*, 2008; Fedosov *et al.*, 2010; Krüger, 2016). In this work we show how this approach can also be extended for more complex cases such as large scale flows with dispersed deforming drops/bubbles and also biological membranes with full FSI, for example flow in heart ventricles with valves. In the case of biological tissues, the deformable membranes can be hyperelastic and orthotropic. The versatility of the IP model easily allows us to extend the method to such materials by changing the formulation of the potentials and deriving the corresponding elastic constants. Additionally electrophysiology can also be implemented into the IP model (this is currently in progress) by solving a constitutive equation for an electric potential along the surface of the membrane. Here the flow in the heart ventricle is driven using an inflow–outflow boundary condition to facilitate comparison with in–house experiments. Thick boundaries (i.e. with thickness larger than the local Eulerian resolution) or volumetric structural elements cannot be handled with the present approach, given the membrane/shell–like formulation of the model.

Another important issue in the simulations involving FSI problems is the type of coupling used i.e. loose (explicit) versus strong (implicit). In the loosely coupled (explicit) case, the fluid and the immersed body governing equations are solved separately one after the another with a transfer of information between them every time step. On the other hand, in the strongly coupled (implicit) case the governing equations are solved in an iterative manner for each time step using a predictor corrector scheme until sufficient convergence is achieved. A detailed solution procedure for a strongly coupled IBM–FSI Navier Stokes solver with the provision for the interaction potential approach is given in de Tullio & Pascazio (2016), where the governing equations are solved using a Hammingś fourth order predictor–corrector scheme. In our code, we have provisions for both a strong (implicit) and weak (explicit) coupling between the fluid and the immersed body. For the simulations shown in the following sections, loose coupling is used given its computationally inexpensive nature. Also it has to be remembered that strong coupling is only needed when added mass effects from the immersed body become important and the recent work by Schwarz *et al.* (2015) gives insights into how this can be tackled smartly while there is still loose coupling between the fluid and the immersed body. We now move on to combining DNS of the fluid governing

equations along with a moving least squares IBM coupled with the interaction potential approach to simulate deformable drops/bubbles and heart ventricles/valves.

2.3 Liquid–liquid interface dynamics using the potential approach

In order to replicate the deformation dynamics of drops or bubbles using the IP model, we first need to devise a method to compute the elastic constants of a given spring network which can represent a liquid–liquid interface with a given surface tension. As mentioned earlier, this is not straightforward since there is no direct physical correlation between the elastic constants and the surface tension of a liquid–liquid interface. Here we use a reverse–engineered approach and perform a single simulation with a set of intuitively chosen elastic constants and estimate the surface tension of the immersed drop by comparing its morphology with previously known analytical solutions. By using the same set of elastic constants but for different flow conditions we also show that such an approach is self–consistent and reliable. Our goal here is to show that the IP model for deformation can be used to replicate the deformation dynamics of liquid–liquid interfaces under given flow conditions.

Before we analyse the results, it important to understand from a theoretical point of view why the IP model can be expected to mimic the deformation behaviour of drops/bubbles. When an initially spherical drop is immersed in a fluctuating flow field, the viscous and pressure stresses tend to deform the drop while the surface tension forces tend to resist the deformation and bring it back to its original spherical shape. During deformation, the total potential energy of the deformation stored in the drops surface is given by $W = \int[(p_i - p_o) - 0.5\gamma(1/R_1 + 1/R_2)]dn \cdot dA$, here p_i, p_o are the pressures inside and outside the drop, γ is the surface tension while R_1, R_2 are the principal radii of curvature (Landau & Lifshitz, 1959). Under the action of external forces, the shape of the drop adjusts itself such that the total displacement potential energy W tends to a minimum. The shape of the deformed drop can be computed by parametrising the surface in such a manner that it satisfies the above condition under certain constraints (for example an ellipsoidal shape or more complex shapes using spherical harmonics) (Emans & Zenger, 2005; Schwarz *et al.*, 2016). The IP model is mathematically analogous in a way that the forces on each triangular vertex (see figure 2.2bc) act such that the total potential energy of deformation $\Pi = W_e + W_b + W_v + W_a$ tends to a minimum. Although the IP model for deforming drops is not an exact representation of the surface tension phenomena it can be considered as a phenomenological approach which can mimic the drop deformation characteristics given the fact that both the exact representation and the IP model rely on the fundamental principle of minimum potential energy.

2.3.1 Deformation of a neutrally buoyant drop in shear flow

For the first test case we choose a neutrally buoyant drop deforming in a laminar shear flow which has a simple configuration and a limited set of control parameters. Variants of this problem have been studied for a long time

and several analytical and phenomenological models already exist in literature which can accurately predict the deformation dynamics of the immersed drop (Maffettone & Minale, 1998; Taylor, 1932, 1934). For this simulation, we use a Cartesian box which is wall–bounded in the vertical direction ($\hat{e}_z$) and fully periodic in the horizontal directions. The top and bottom walls move in the opposite direction parallel to each other with the same velocity to generate a laminar shear in the domain. A triangulated sphere as shown in figure 2.1a is positioned in the flow at a distance $0.5L_z$ from the walls (L_z is the gap between the walls).

The degree of deformation and orientation of a viscous drop in the presence of a velocity gradient depends on the Capillary number $Ca = \mu_f R\dot{\gamma}/\sigma$, where R, $\dot{\gamma}$, σ and μ_f are the drop radius, local strain rate, surface tension and fluid viscosity, respectively. For these simulations the viscosity ratio of the droplet and the carrier phase is set to 1, i.e. $\hat{\mu} = \mu_d/\mu_c = 1$. Since this simulation will be used to 'tune' the elastic constants to replicate a liquid–liquid interface, we assume that the immersed drop is very small in comparison to the distance between the walls and the immersed boundary forcing $\boldsymbol{f}$ in equation (2.1) is set to zero. This is done so that the immersed sphere only experiences the forces generated due to the laminar shear from the moving walls and not due to any wall effects. It also facilitates in quickly tuning the elastic constants due to the ease in setting up such a simulation. Here it is important to point out that while we choose the system of a neutrally buoyant deforming drop any other flow with known solutions can be used.

To estimate the ad–hoc surface tension value for any given spring network the following steps are undertaken. We first fix the Lagrangian resolution i.e the number of vertices on the surface of a sphere and initialize a spherical drop under a given shear rate $\dot{\gamma}$ with a set of elastic constants. For the first set of elastic constants, k_e and k_a are fixed to large values in comparison to k_b thus resulting in an extremely stiff drop. k_v is chosen to be much larger than the rest of all constants as this ensures incompressibility of the immersed drop. Once the first set of elastic constants are chosen the drop is allowed to deform under the action of the velocity gradient $\dot{\gamma}$ according to the potential approach described in the previous section. If the final state of the drop is close to spherical, the elastic constant k_e and area constant k_a are reduced simultaneously which reduces the overall stiffness resulting in deformation of the spring network. Here it is important to note that if both k_v and k_a are fixed to a large value, which would imply conservation of both the volume and total area, the triangulated sphere would represent a vesicle. To represent a drop, both k_e and k_a are reduced to a low enough value such that the drop deforms approximately into an ellipsoid as shown in figure 2.3ab. The initial and final states of the triangulated sphere shown in figure 2.3ab are for two different Lagrangian resolutions i.e the spheres are discretized using 320 and 1280 triangular elements (faces), respectively.

We now give an estimate of the elastic constants used for the following analysis. For any given spring network with a prescribed elastic modulus and mass distribution, the ratio $k_e l_e^2$ (l_e is the mean edge length on the sphere) should be independent of the number of triangular elements (Van Gelder, 1998). For the sphere shown in figure 2.3a, $k_e l_e^2 = 3 \times 10^{-3}$ and $l_e/L = 1.5 \times 10^{-2}$. The bending constant is set as $k_b = k_e/10.0$ while the volume constant is

set to a very large value; in this case $k_v = \alpha_v k_e$ where typically $\alpha_v \sim 10^4 - 10^5$ is sufficient to ensure that incompressibility of the sphere is ensured. The area constant k_a is set equal to that of the elastic constant. As discussed previously, when simulating other systems (for example vesicles) which also require surface area conservation along with volume conservation the area constant k_a is also set to relatively large value similar to the volume constant k_v. On changing the Lagrangian resolution the elastic constants should also be scaled in a way that the product $k_e l_e^2$ remains unchanged. This ensures that the physical properties of the spring network remains similar and is independent of the resolution used. The time step for the following simulation is set to $\Delta t = 10^{-4}/\dot{\gamma}$ ($\dot{\gamma}$ is the imposed strain rate) and the convergence criteria is such that the change in the total surface area of the sphere in successive time steps is less than 10^{-6}.

Once the deformation of the sphere has reached a steady state under a laminar shear flow, we compute its semi–major axis (L) and semi–minor axis (B). Next, we use a phenomenological model proposed by Maffettone & Minale (1998) (hereafter called 'MM' model) to estimate the Capillary number Ca for which a neutrally buoyant immersed drop would have the same final state under similar flow conditions. The model proposed by Maffettone & Minale (1998) predicts the deformation of a drop in an arbitrary velocity field under the assumption that the drop is ellipsoidal in shape. For a simple flow field such as a laminar shear flow the model can be analytically solved to give the steady state values of the semi–major (L) and semi–minor axis (B) of the deformed drop as given below.

$$L^2 = \frac{f_1^2 + Ca^2 + f_2 Ca\sqrt{f_1^2 + Ca^2}}{(f_1^2 + Ca^2)^{1/3}(f_1^2 + Ca^2 - f_2^2 Ca^2)^{2/3}},$$

$$B^2 = \frac{f_1^2 + Ca^2 - f_2 Ca\sqrt{f_1^2 + Ca^2}}{(f_1^2 + Ca^2)^{1/3}(f_1^2 + Ca^2 - f_2^2 Ca^2)^{2/3}},$$

where f_1 and f_2 are constants which depend on the viscosity ratio ($\hat{\mu}$) and Ca is the Capillary number

$$f_1 = \frac{40(\hat{\mu} + 1)}{(2\hat{\mu} + 3)(19\hat{\mu} + 16)} \qquad f_2 = \frac{5}{2\hat{\mu} + 3}.$$

This model has already been used in other studies; for example to predict hemolysis of red blood cells (de Tullio *et al.*, 2012) and also deformation and orientation statistics of drops in turbulent flows (Biferale *et al.*, 2014; Spandan *et al.*, 2016). Additionally experimental studies have shown that under moderate deformations the steady–state droplet shape can be very well described by an ellipsoid (Guido & Villone, 1998; Torza *et al.*, 1972).

In figure 2.3cd we plot the analytical solutions (MM model – solid lines) in the form of the lengths of the semi–axes and the orientation angle of the major axis (corresponding to the axes with length L) with the stream–wise direction versus the Capillary number. Using this as a reference, we check the position of overlap of the semi–axes lengths computed through the IP model with the MM model to estimate the corresponding Capillary number. This match is shown through a vertical dotted line in figure 2.3c and since the flow

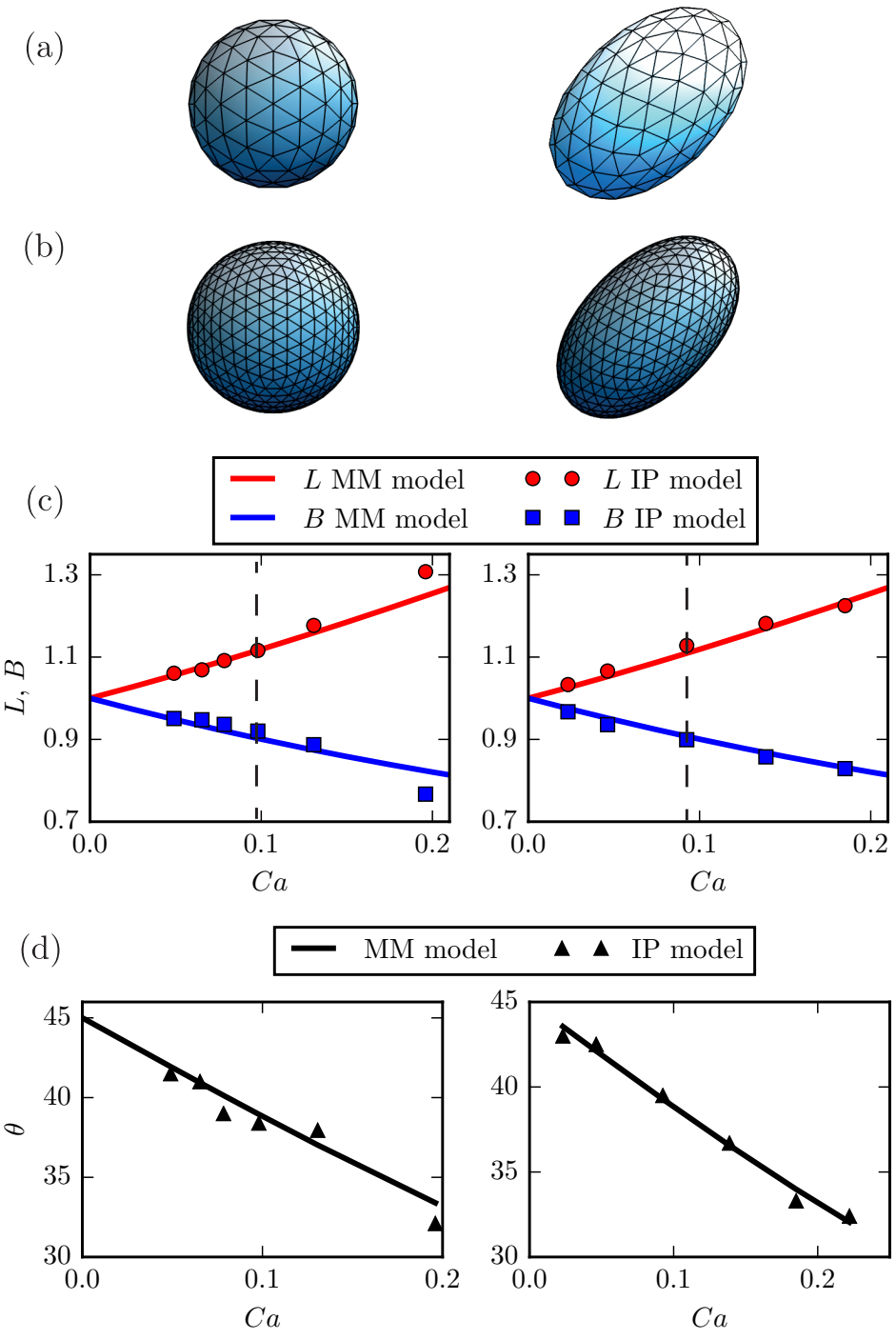

Figure 2.3: Deformation of a neutrally buoyant drop in a laminar shear flow using the IP model. Lagrangian resolution of a) $N_{\text{faces}} = 320$, b) $N_{\text{faces}} = 1280$. In both cases, the viscosity ratio is set to $\hat{\mu} = 1$. c) Comparison of the semi–axes lengths versus the Capillary number. d) Comparison of the angle formed by the major–axis in the shear plane with the velocity direction.

configuration such as drop radius, viscosity and shear rate are already fixed in the simulation, this Capillary number can be directly used to estimate the ad–hoc surface tension value for the chosen elastic constants. The left and right panels in figure 2.3 correspond to different Lagrangian resolutions. The important point to observe here is the reasonably good match between the semi–axes lengths computed from the IP model and the MM model. Small differences in the semi–axes lengths could arise due to multiple reasons: (i) lack of sufficient Lagrangian resolution, since in the IP model the surface of the sphere is discretized using markers; (ii) MM model assumes a perfectly shaped sphere which deforms into an ellipsoid, while the IP model has no constraint of deforming into an ellipsoid; (iii) the elastic constants would need further tuning.

Next we keep the elastic constants the same and change the Capillary number which can be done by either changing the shear rate or the viscosity of the fluid. As shown in figure 2.3cd again the semi–axes lengths computed from the IP model agree reasonably well with the analytical solutions from the MM model. This shows that the ad–hoc surface tension computed by fitting the results from a single simulation using the IP model with MM model is reliable to extend the approach to other flow conditions. A good agreement with the MM model is found also for the orientation angle of the semi–major axes as shown in figure 2.3d. At higher Capillary numbers ($Ca = 0.2$) there is some difference found in the lengths computed from the IP model as compared to MM model (left panel of figure 2.3c). However, this is just an effect of the Lagrangian resolution and can be corrected by increasing the number of vertices on the surface of the sphere, as can be seen in the right panel of 2.3d.

2.3.2 Dynamics of a liquid–liquid interface deforming in cross–flow

In the previous subsection we demonstrated that by tuning the elastic constants for a single flow configuration to compute an ad–hoc surface tension, the IP model can be used to reliably simulate a neutrally buoyant drop deforming in a laminar shear flow. We now move on to simulating a more dynamic problem where the interface is strongly linked to the local flow conditions. In order to do this we take the same test case as done by Schwarz *et al.* (2016) and have a drop immersed in a cross flow and compute the mean shape arising from the resulting flow conditions. For such a flow, the aspect ratio of the deforming drop depends strongly on the Weber number $We = \rho_f U_{\text{ref}}^2 d_{\text{eq}}/\sigma$, which is the ratio of inertia forces acting on the drop in comparison the surface tension forces (Loth, 2008). The cross–stream set up in the domain is influenced by the interface of the spherical drop leading to the development of a boundary layer on the drop surface and a corresponding wake.

The computational domain is taken to be of size $L = (10, 5, 5)d_{\text{eq}}$, d_{eq} is the diameter of the drop in its initial spherical shape. The spherical drop is triangulated with $N_v = 2562$ nodes and is placed at $\boldsymbol{x} = (0.5, 0.5, 0.5)L_z$. The vertical direction ($\hat{e}_z$) is wall bounded with stationary free–slip walls; $\hat{e}_y$ direction is periodic in nature and a uniform flow of $\boldsymbol{U} = U\hat{e}_x$ is imposed in the $\hat{e}_x$ direction.

The control parameters for such a problem are the Reynolds number, $Re = Ud_{\text{eq}}/\nu_f$ and the Weber number, $We = \rho_f U_{\text{ref}}^2 d_{\text{eq}}/\sigma$. The response

of the system can be measured through the quantification of the wake of the drop and also through the morphology of the drop. The combined action of the dynamic pressure acting on the faces of the drop and the shear stresses generated from the boundary layer development on the surface of the drop leads to its deformation. In figure 2.4 we show the wall–normal component of the velocity field (u_z) and the corresponding deformed drop represented through the triangulated spring network. The two snapshots shown in figure 2.4 are at two different instants showing the starting up phase and the deforming phase. To quantify the shape of the immersed drop we compute the mean aspect ratio of the bubble measured as the ratio of the lengths of the drop bounding box in the wall–normal and stream–wise directions i.e. $X = l_z/l_x$, where X is the aspect ratio and l_z, l_x are the lengths of the box surrounding the deformed drop in the $\hat{e}_z, \hat{e}_x$ directions, respectively.

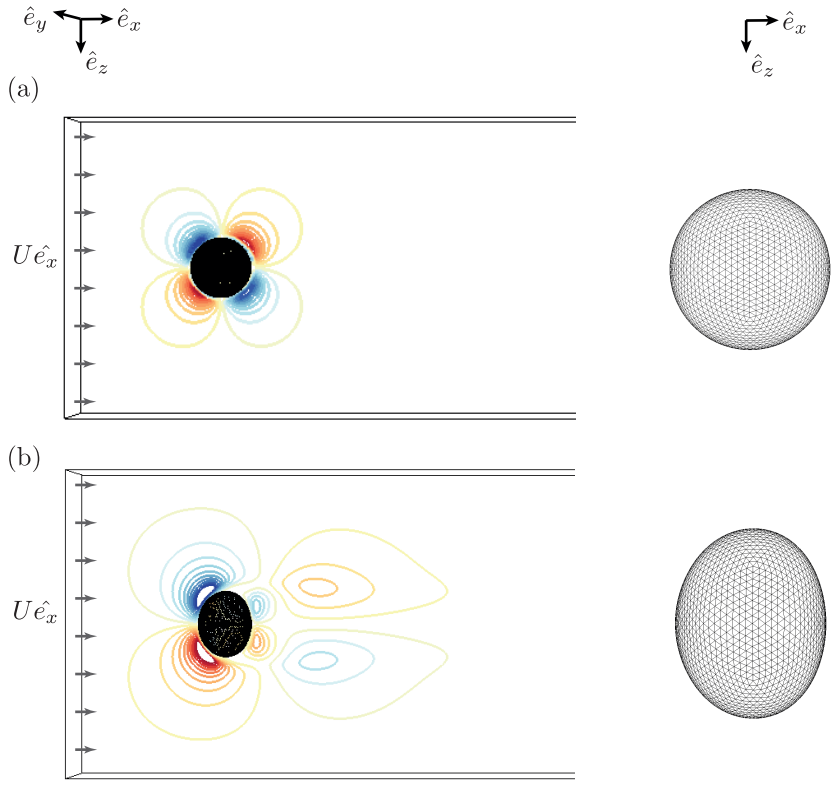

Figure 2.4: Left panels show the contours of velocity in $\hat{e}_z$ direction along with the deforming drop at two different time instants. Right panels show the corresponding drop in the form of the deformed triangulated spring network. The Reynolds number of the flow based on the initial drop diameter is set to $Re = 150$, while the elastic constants chosen correspond to a Weber number $We = 2$.

In figure 2.5 we plot the inverse of the measured aspect ratios of the deformed drop versus the corresponding Weber number and compare it with experimental data from multiple measurements (Loth, 2008). For these simulations the Reynolds number is fixed to $Re = 150$ and the Weber number is changed by modifying the elastic constants for each simulation. A very good match is found between the aspect ratios computed from the IP model and the

several experimental measurements of drop shapes found in literature. These simulations further show that the IP model can be reliably used to simulate deformation in liquid–liquid interfaces under given flow conditions.

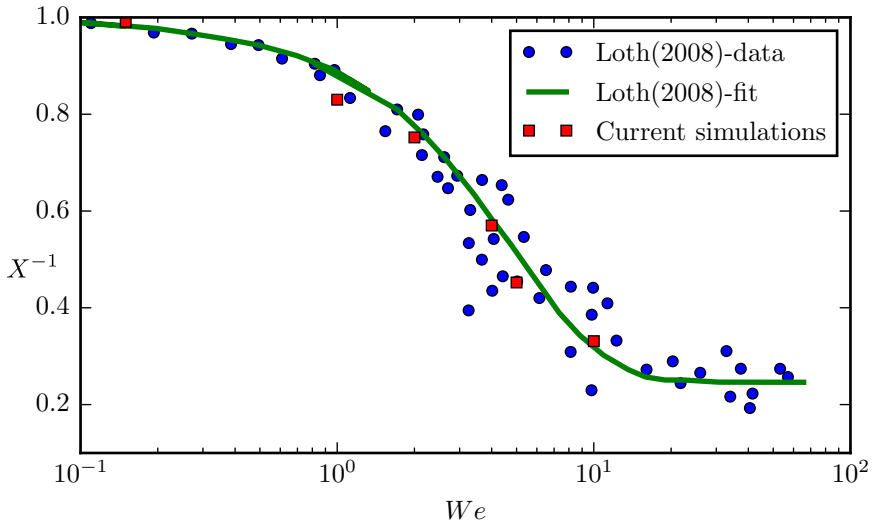

Figure 2.5: Comparison of the inverse aspect ratio (X^{-1}) of the deformed drop versus Weber number at $Re = 150$, with data from Loth (2008) for contaminated drops or bubbles.

2.4 Dynamics of the left heart ventricle

We now move on to simulating the flow inside the left ventricle of the heart where the motion of the ventricle and the valves are fully coupled to the flow dynamics. The results from the numerical simulations are compared against ad–hoc experiments where the ventricle is made up of silicone rubber.

The various structures used for this simulation are shown in figure 2.1 and it is important to note that each structure is made up of a different material i.e. each material has a different elastic property. The left ventricle and the natural mitral valve can move and deform based on the local flow; the leaflets of the mechanical mitral valve, while rigid in shape, can move depending on the forces acting on their faces and more specifically on the moments of the pressure and viscous forces about the hinges of the leaflets; the channels for the aortic and mitral valves are completely rigid, fixed in space and provide a passage for the influx and outflux of the flow. The aortic valve is not simulated explicitly in these simulations but only through an opening/closing mechanism that is imposed by the immersed boundary depending on the phase of the cycle. While this has been done to limit the computational effort, it has no major consequences on the results because we are only interested in the ventricular flow and the aortic valve influences flow mainly in the ascending aorta. The dynamics of the aorta could affect the ventricular flow because of the timing of the opening and closure of the aperture, but it is driven by the impedance of the circulatory system downstream and its simulation is much more complicated and out of scope of this chapter.

In reality, the configuration of the left ventricle is determined by the dynamics of the myocardium contraction and relaxation along with the deformation of the valves and vessel walls. The complete structure adjusts to the forces induced by the hydrodynamic loads (pressure and shear stresses), body forces, internal damping and the internal elastic forces. In our simulations, the flow into the ventricle is governed through an inflow–outflow channel rather than a myocardium contraction to facilitate comparison with experiments. Similar to the experiments, the ventricle is assumed to be made of a homogeneous material i.e. silicone rubber. With minor modifications the IP approach works equally well for hyper elastic or inhomogeneous (orthotropic) materials as discussed in section 2.2.

2.4.1 Experimental and numerical set–up

In figure 2.6a we show a CAD rendering of the experimental apparatus used to replicate the dynamics of the left ventricle with a mechanical mitral valve and results from this will be used to validate the numerical model. An electric motor is used to drive a cam which imposes a prescribed displacement in time of the pneumatic piston/cylinder. The cylinder is directly linked to a Plexiglass box which is transparent and allows for the observation of the evolution of the left ventricle model inside. The time law imposed by the pneumatic cylinder is replicated by the fluid in the tank in which the left ventricle is immersed and is the only deformable element. Moreover the evolution of the flow rate imposed by the motion of the cylinder is captured versus time and this is used as a boundary condition in the numerical simulations. This is shown in figure 2.7 where we plot the flow rate versus time. As can be seen, the first part of the cycle has one strong peak (E–wave) and a secondary weak peak (A–wave) which is the result of the shape of the cam. The shape of the cam can be modified to achieve any desired flow rate profile. In the case shown here the ratio of amplitudes of E–wave to the A–wave is approximately 20:3. The profile of the cam is chosen in such a way that the flow rate resembles that of an inefficient and failing left ventricle and is generally observed in old people or heart patients. In a healthy condition, the time evolution of the flow rate versus time is similar to that shown in figure 2.7 but with an amplitude ratio of A–wave to E–wave of approximately 0.5. The efficiency/healthiness of the ventricle can also be quantified using ejection fraction (EF) which quantifies the pumping efficiency of the ventricle and is calculated as $EF = (V_M^* - V_m^*)/V_M^*$; V_m^* and V_M^* being the minimum and maximum values of the volume of the left ventricle, respectively during the cycle.

The left ventricle is transparent and made up of silicone rubber, fixed to the upper surface of the box by a rigid plate and consists of a mechanical mitral and aortic valves. The fluid (deionized water here) inside the left ventricle is pumped into the aorta which then flows into the hydraulic circuit composed of two branches. In one, the windkessel, there is a box connected in series to simulate the vascular capacitance while there are gate valves to regulate the impedance of the systemic circulation or to exclude one branch or another. The fluid after passing through the hydraulic circuit returns into the ventricle through the duct and a new cardiac cycle starts. In order to compare experimental measurements and numerical simulations we make use of Particle Image Velocimetry (PIV) measurements (Falchi *et al.*, 2006) where the fluid is

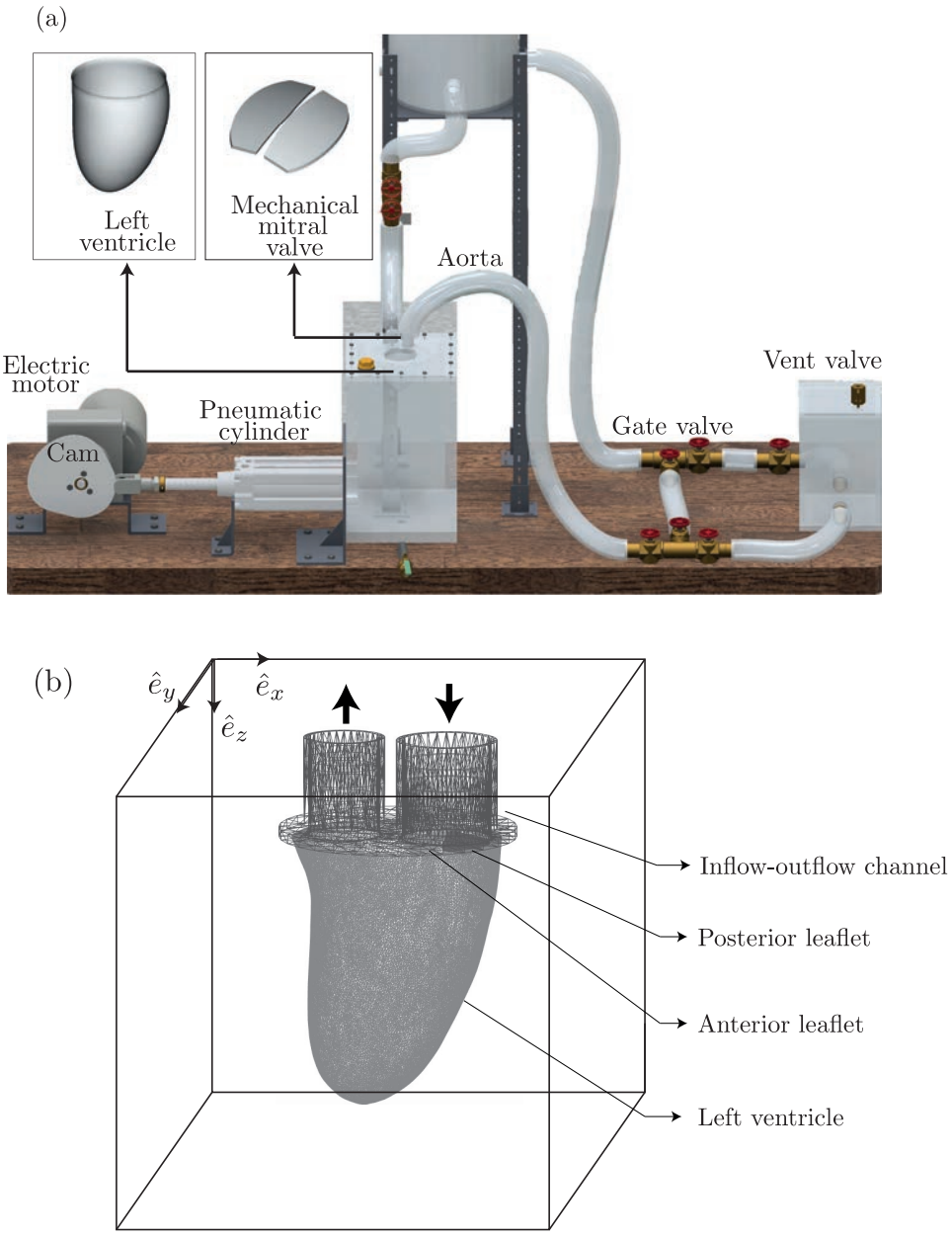

Figure 2.6: a) CAD rendering of the experimental set–up built for validating the numerical approach. b) Cartesian computational box with the inflow–outflow channel, mitral valve and the left ventricle. Individual components are shown in figure 2.1.

seeded with tracer particles (10 μm diameter pine pollen) and illuminated by a laser sheet. The motion of the particles is captured using a high–speed camera and a robust algorithm is used to compare image windows in subsequent frames and estimate the velocity field in the flow on a regular grid.

In figure 2.6b we show the computational domain and the set–up of the complete left ventricle along with the mechanical mitral valves and the channels for the aortic and mitral valves. The geometry of the structures, the material properties and the boundary conditions have been chosen to replicate the experimental conditions as close as possible. The channels connected to the mitral and aortic valve perform the function for allowing the influx/outflux of the fluid into/from the ventricle. Since we use the IBM formulation for representing any immersed body, the whole domain is filled with a single fluid. The domain is periodic in all the directions $\hat{e}_x$, $\hat{e}_y$ and while it is confined in the $\hat{e}_z$ direction it allows for inflow–outflow boundary conditions on selected regions.

The flow rate evolution shown in figure 2.7 is used as the boundary condition on the inflow/outflow channels and is linked to an amplification factor that regulates its amplitude, i.e. the higher the amplitude the higher the ejection fraction of the left ventricle. In the numerical simulations we set the value of EF to 30% which is what is imposed in the experiments in order to study the flow in a severe failing left ventricle.

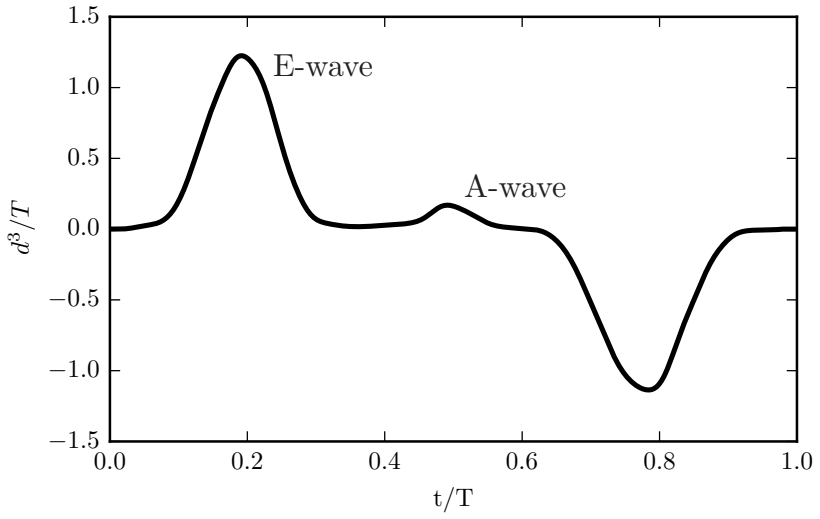

Figure 2.7: Flow rate (scaled by the diameter d of the opening to the mitral valve) versus time (normalized using time T required for one cardiac cycle). It regulates the expansion (positive flow–rate or diastolic phase) and relaxation (negative flow–rate or systolic phase) of the ventricle.

After performing grid independence tests, a resolution of 150x150x150 was chosen for the Eulerian field. The surface of the ventricle is discretized with 51142 triangular elements; mechanical valves with 2578 elements and the natural valves with 3794 elements each. Both experiments and the simulations are performed in dynamic similitude with a real left ventricle i.e. since the dimensions in the experiments and simulations are set to a 1:1 ratio in comparison with a real left ventricle and water is four times less viscous than blood,

the total system is pulsated four times slower to maintain the same Reynolds number. The characteristic Reynolds number in the flow based on the mitral orifice diameter and maximum inflow velocity is around 5000. For a nearly isotropic membrane, the elastic constants used in the spring network can be computed using the model by Van Gelder (1998) as $k_e = Eh(A_1 + A_2)/l_o^2$ and $k_b = 2B/\sqrt{3}$; E and B are the Young's modulus and bending stiffness of the membrane, respectively while h is the local membrane thickness and A_1, A_2 are the areas of the triangles sharing an edge with initial length l_o. The experiments discussed in the work use rubber silicon as the membrane material and the elastic constants for the simulations are directly computed from the physical properties of rubber silicon.

We first look at the large scale flow structures created inside the ventricle. In figure 2.8 we plot the instantaneous snapshots of the flow velocity vectors in the mid–Y plane at certain time instants. All the left panels correspond to numerical simulations while the right panels show the measurements from the PIV experiments. It can be seen that the large scale flow dynamics can be reliably captured in the numerical simulations as compared to the experiments. During the initial part of the cardiac cycle i.e. the diastole, the jet from the mitral valve passes through the prosthetic mechanical leaflets which starts to open. The flow over the two leaflets results in the propagation of two vortices into the ventricle, one close to the left wall and the other in the center. The two vortices are directed towards the apex of the ventricle, but since in both the simulations and experiments we reproduce the dynamics of a failing left ventricle the vortices soon dissipate into small scales and the mitral jet is not able to penetrate down to the apex and wash out the stagnant fluid. This will be shown more clearly later.

We now compare the mean position of the left ventricle in the $\hat{e}_x$ and $\hat{e}_z$ directions to further validate the dynamics of the deforming ventricle from the numerical simulations. This is shown in figure 2.9 where the mean position x/d and z/d is plotted against time. The fluctuations in the mean x–position of the left ventricle occurs due to its asymmetrical geometry with respect to the mitral jet. The fluctuations seen in the numerical simulations are entirely physical as we consider full FSI without any kinematic models to govern the motion of the ventricle. The oscillations seen in the numerics cannot be fully resolved in the experimental measurements. The positions obtained from the numerical simulations have reasonably good agreement with its experimental counterpart except from small oscillations which cannot be captured in the experiments. This shows that not only the large scale flow structures, but also the dynamics of the deforming left ventricle which is modelled using the interaction potential approach can be simulated with reasonable accuracy.

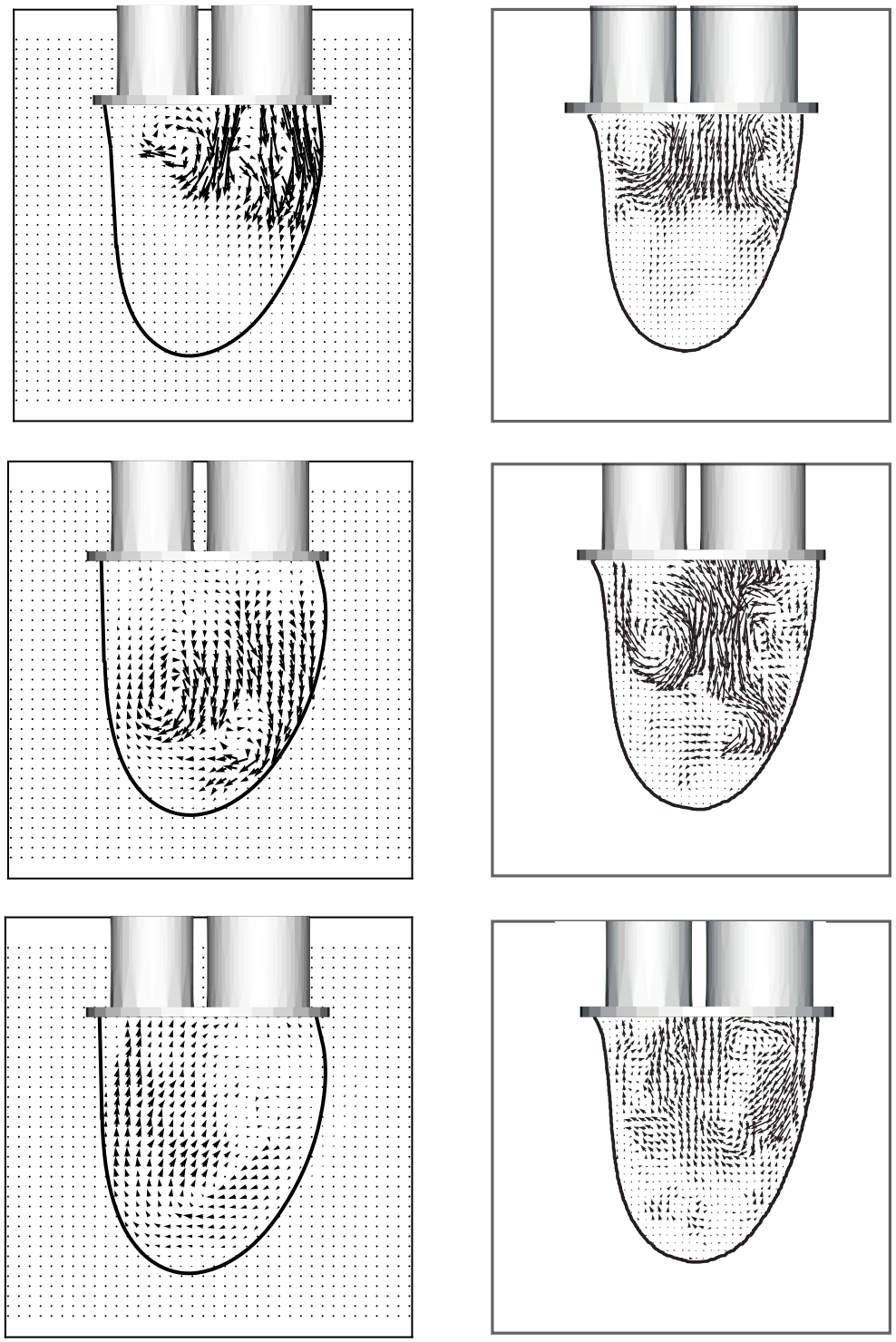

Figure 2.8: Snapshots of the flow inside the ventricle during the diastolic phase in the cardiac cycle: (left panels) numerical simulations; (right panels) experimental measurements.

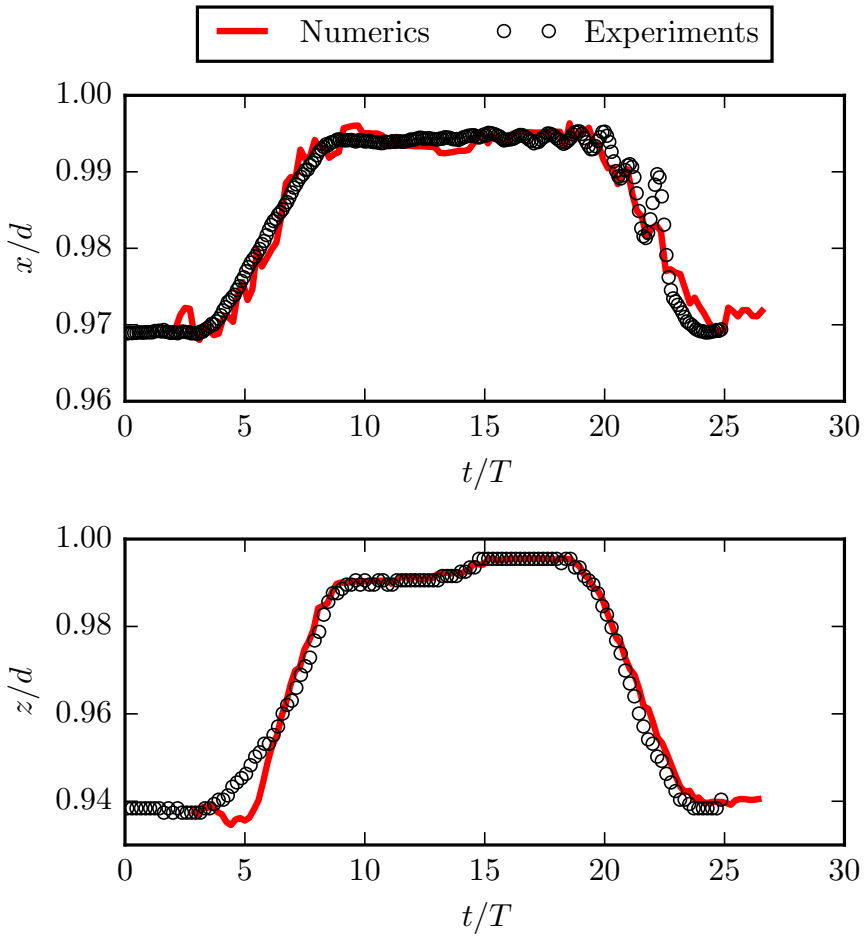

Figure 2.9: Comparison of the mean position of the left ventricle in the $\hat{e}_x$ and $\hat{e}_z$ directions versus time.

2.4.2 Mechanical and natural mitral valve

An important element affecting the dynamics and nature of the flow is the presence of the mitral valve. To understand the effect of the mitral valve we couple our computational model of the left ventricle with two kinds of mitral valve: prosthetic mechanical valve and natural valve. While the former is structurally rigid, the latter is similar to a flexible membrane and can deform based on the local flow conditions (see figure 2.1). In figure 2.10 we show both the mechanical and natural valve during their initial state and when they are close to being fully open. Here we would like to again emphasize that since the numerical set up uses a FSI approach, the valve dynamics are solely determined by the hydrodynamic loads and any geometrical constraints set up by the user. The panels on the right in figure 2.10 show a clear difference in the shape of the ventricle. The shape of the ventricle depends heavily on the hydrodynamic loads exerted on it from the fluid inside it. The mechanical and natural mitral valves lead to different flow structures inside the ventricle and thus a different shape of the ventricle. We now show the difference in flow structures arising from the different valves used.

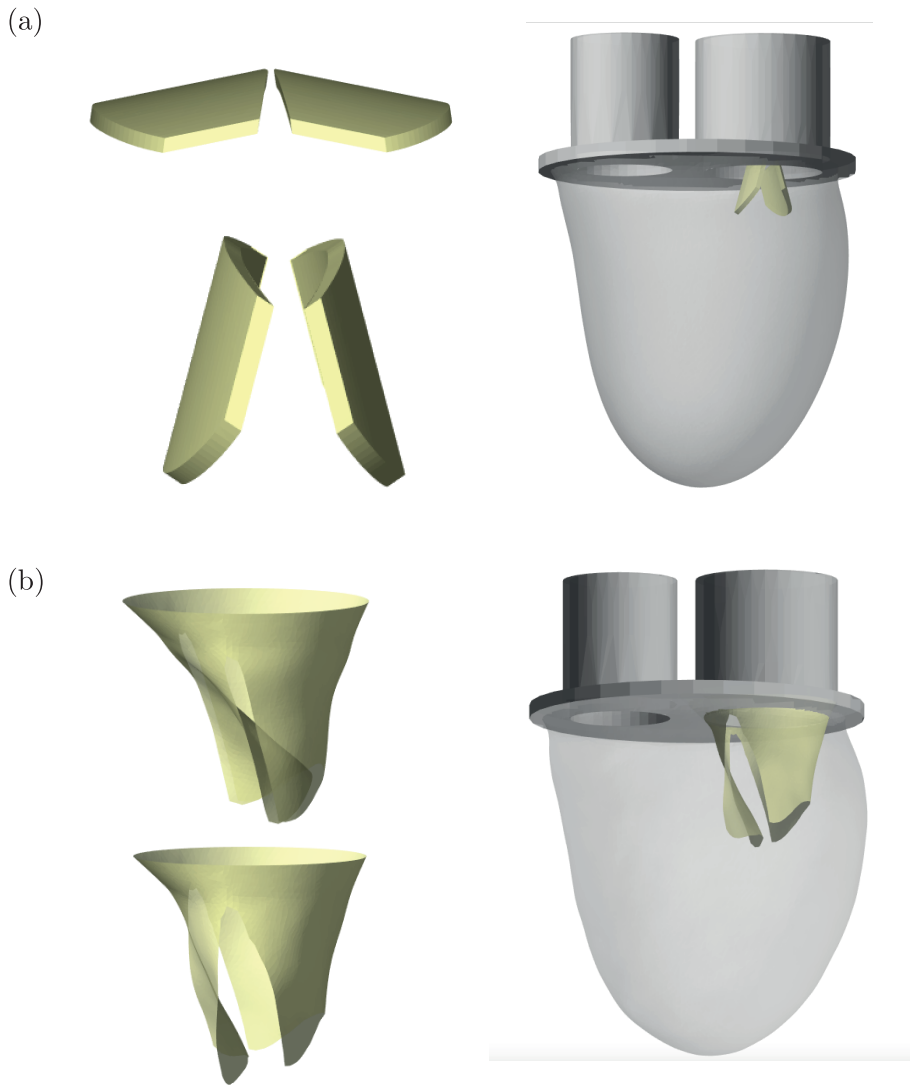

Figure 2.10: The left panels show snapshots of a) mechanical and b) natural valves at two different time instants in the diastolic phase of the cardiac cycle. The right panels show the full set up of the ventricle along with the valves and the inflow/outflow channels.

First we consider the case of a prosthetic mechanical mitral valve which in a sense obstructs the flow through the mitral orifice. For the dynamics of the full valve, we allow each leaflet to rotate around a fixed axis which is symmetric about a plane situated in the center of the mitral orifice. In figure 2.11 we show the dynamics of the leaflets which go in opposite directions and close asymmetrically since the backward flow induced by the systole comes from different regions of the ventricle for the anterior and posterior leaflets. The opening phase starts at the beginning of the diastole as the flow starts accelerating and finishes before the end of the flow acceleration when the fully open position is reached. The closing phase starts when the flow rate reaches its peak and ends when the minimum negative value of the flow rate function is achieved, thus positioning the leaflets in the fully closed position.

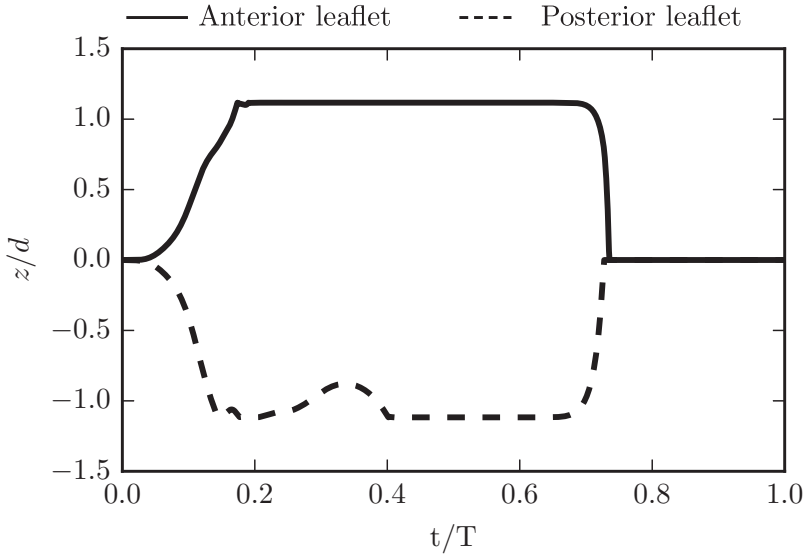

Figure 2.11: Axial position of the center of mass of prosthetic mechanical leaflets for a healthy left ventricle in a single cardiac cycle. The solid line and dashed line represent two different leaflets. d is the diameter of the mitral orifice, while T is the time taken for one full cardiac cycle.

In figure 2.12 we show instantaneous velocity fields during the diastolic phase of the cardiac cycle with both a prosthetic mechanical and natural mitral valve. In the case of mechanical valves (top panels of figure 2.12), the leaflets start rotating during the early opening phase and destabilize the mitral jet. In the bottom panels of figure 2.12 we show the flow structure in the presence of a natural mitral valve which is also made up of two leaflets but has different dynamics due to the inherent deformability of the natural valves. In the presence of the mechanical valve, the flow is split into three different jets thus causing high vorticity regions in the wake of the valve. This results in the mitral jet not reaching the bottom of the ventricle as desired. It is evident that the disturbance generated by the mechanical leaflets destabilizes the mitral jet, creating vortex rings thus further decreasing its capability to penetrate the ventricular region. The flow soon degenerates into small scales that are dissipated during the diastatic phase of the cycle. Unlike the prosthetic mechanical valves, the natural valves can deform based on the local hydrodynamics forces allowing for a much smoother flow of the mitral jet into the ventricle. Due to this the natural valves evolve differently resulting in a different flow structure in the ventricle which reaches the bottom of the ventricle which is a desired flow condition.

From the discussion of figure 2.12 it is clear that the behaviour of the flow inside the left ventricle depends strongly on the kind of mitral valve used. Overall, we have been able to show that the complete dynamics of the left heart ventricle with either mechanical or biological valves can be simulated reliably using IBM coupled with an interaction potential approach for deformation.

Figure 2.12: Snapshots of the flow inside the ventricle at the two different time instants (left and right panels) in the diastolic phase of the cardiac cycle. Top panels show the ventricle with a mechanical natural valve while the bottom panels show the ventricle with a deformable natural valve. The colour represents the iso–surface of the velocity magnitude of the flow inside.

2.5 Parallel performance

In this section we describe the parallelization strategy implemented and the data structures required for parallelizing the algorithms described in previous sections. For dealing with a suspension of spherical particles, Uhlmann (2004) proposed a 'master' and 'slave' strategy, where each particle is allocated an individual 'master' processor which is responsible for all the computations related to it. Additional 'slave' processors may be allocated to help the 'master' processor. Wang *et al.* (2013) employ a 'gathering–scattering' strategy where a single master processor is responsible for the computation of the Lagrangian force on the immersed bodies and advecting them and this information is scattered to the slave processors which solve the Navier–Stokes equations in parallel. While both parallelization approaches have been shown to produce reasonable performances, there exist some drawbacks and challenges. The strategy implemented by Uhlmann (2004) requires continuous exchange of control on the Lagrangian mesh by the processors which may lead to a complex programming environment. The approach of Wang *et al.* (2013) eliminates this issue leading to a simple structure of the code while increase in the memory usage on the master processor and data transfer between the master and slaves are some hurdles. In this work, we propose a different easy to implement parallelization approach for the IBM where the information of all triangle nodes is present with all processors. But the computation required for each Lagrangian node/structure is performed only by specific processors depending on the type of computation that needs to be performed. In other words the allocation of processor for the IBM depends on the task that needs to be performed which results in a task–based parallelism for the FSI–IBM computation.

We first describe in brief the parallelization strategy employed for the flow solver and later explain the data structures and parallelization implemented for the FSI–IBM in the appendix. For the flow solver we employ domain decomposition and split the Cartesian box into slabs i.e. 'one–dimensional slab' parallelization. It is also possible to use a Cartesian box decomposed with 'two–dimensional pencil' parallelization as shown in van der Poel *et al.* (2015). In such a fluid solver, the viscous terms are computed explicitly in the periodic directions to take advantage of the reduced ALL–to–ALL communications. This may prove fatal dispersed deforming bodies in the flow since we also need to resolve the boundary layers over the immersed bodies which have dominant velocity gradients. With pure MPI, slab based codes already give good scalability up to 10^3 cores and this can be further enhanced to 10^4 cores by having a hybrid MPI+OpenMP type parallelization which is already sufficient to tackle a large scale of problems.

In addition to the slabs, each processor needs to store information from the neighbouring processors which would be required for computing the derivatives and is stored in what is called as a 'halo/ghost' layer. Since the flow solver employs a second–order finite difference spatial discretization at most one halo layer is required on each side of a slab for single phase flows. However, as we explain later when this solver is coupled with a FSI–IBM solver for finite–size bodies which makes use of MLS interpolations, multiple halo layers become necessary. It is important to keep in mind that an unrestricted increase in

the number of stored halo layers would automatically result in an increase in the communication time which may deteriorate the overall performance of the code. For the MLS interpolations which need a support domain of 27 (3x3x3) Eulerian points at most 3 halo layers are necessary.

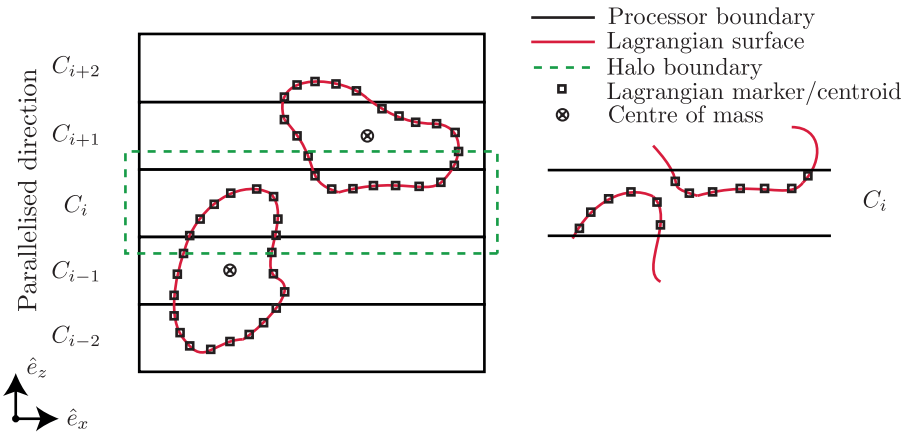

Figure 2.13: Schematic of two bodies immersed in a flow. Flow solver is 1D slab parallelized. $\hat{e}_z$ is the wall–normal direction.

We consider two arbitrarily shaped deformable bodies immersed in a flow as shown in figure 2.13, where the squares represent the Lagrangian markers/centroids of the triangular elements. The allocation of Eulerian slabs to each processor is straight forward as the Eulerian mesh stays fixed in time and this is done at the start of the simulation. For the flow solver each processor with identity `myid` is allocated the task of solving equation (2.1) on a slab of `[1:N_1,1:N_2,N_3_start:N_3_end]`. Given below are the steps undertaken to complete one full time step of the simulation. As given below there are four major steps and multiple sub–steps involved in completing one full iteration. The steps shown here are applicable for a loosely coupled approach which has been used for the simulations in this chapter; details on the strongly coupled approach are elaborated in the paper by de Tullio & Pascazio (2016).

1. Compute the indices of all markers/centroids on the Lagrangian mesh relative to the Eulerian mesh.
2. Compute the properties of the Lagrangian mesh, i.e. surface areas and normals of each face of the Lagrangian mesh.
3. Compute flow configuration along with IBM forcing i.e. all three sub–steps of RK3 integration.
   (a) Compute intermediate fluid velocity under the RK3 framework.
   (b) Interpolate velocity on the centroids of the Lagrangian mesh using MLS interpolation.
   (c) Communicate the forces in the halo cells to neighbouring processors.
   (d) Correct intermediate velocity using the MLS–interpolated force.
   (e) Solve pressure correction equation and compute the pressure and solenoidal velocity field.

4. Compute external and internal loads on the immersed body.
   (a) Compute the external loads which is the sum of pressure and viscous forces on each face using MLS interpolation.
   (b) Sum up external loads on all faces across all processors.
   (c) Compute internal loads which are derived from the potentials described in section 2.2.
   (d) Sum up internal loads across all processors.
   (e) Update the nodes of the triangles using Newton's law of motion.

2.5.1 Data structures and pseudo code for Lagrangian mesh parallelization

Here we give the details on the data structures and the pseudo code for the parallelization of the IBM–IP solver.

The Lagrangian meshes shown in figure 2.1 are unstructured and are exported in the form of a GTS (GNU Triangulated Surface) data format which contains information about the spatial positions of the vertices of the triangular elements, the various vertices which are connected by edges and also the edges which constitute a face. Using this information we construct additional auxiliary arrays which will be required while computing the total force acting on the triangle nodes based on the potentials described in the section 2.2. The total number of vertices, edges and faces on a single immersed body is stored in `N_vert`, `N_edge`, `N_face`, respectively while `N_particle` is the total number of immersed bodies to be simulated and `N_edge_vert` is the maximum number of edges that any single vertex can be connected to. A brief overview of the required auxiliary integer arrays is given below.

1. `vert_of_edge[2, N_edge, N_particle]` : Contains pairs of vertices sharing a single edge.
2. `face_of_edge[2, N_edge, N_particle]` : Contains pairs of faces sharing a single edge.
3. `vert_of_face[3, N_face, N_particle]` : Contains the three vertices that constitute a single face.
4. `edge_of_face[3, N_face, N_particle]` : Contains the three edges that constitute a single face.
5. `vert_of_vert[N_edge_vert, N_vert, N_particle]` : Contains all the vertices that a single vertex is connected to.
6. `edge_of_vert[N_edge_vert, N_vert, N_particle]` : Contains all the edges that a single vertex is connected to.
7. `v1234[4, N_edge, N_particle]` : Contains all the four vertices that is contained in two faces sharing an edge.
8. `pind[3, N_face, N_particle]` : Stores the [`N_x`,`N_y`,`N_z`] indices of each centroid relative to the Eulerian mesh and tells us inside which Eulerian computational cell the centroid resides in. This array is updated every time step.

9. `bboxind[6,N_particle]` : Stores the indices of the bounding box of each immersed body.

In the first step, we compute the indices of all the centroids on every triangular element and store it in a global array `pind`. In addition to the axial index of every triangular element we also compute the mean axial index of every immersed body i.e for an immersed body `i` the mean axial index is `bboxind[1:3,i]=0.5*(max(pind[1:3,:,i]+min(pind[1:3,:,i]))`. In step 2, we compute the geometrical properties of the triangulated mesh (i.e. surface areas and normals of each triangular element). Both steps (1 and 2) are done by all processors (i.e. `MPI_COMM_WORLD`) on all immersed bodies and at the end of this operation every processor has information on all three indices [`pind(1:3,N_face,N_particle)`] of every centroid immersed in the flow, surface areas and normals of every triangular element.

For steps 3(a), 3(d) and 3(e) each processor performs all the operations required on its respective slabs. Step 3(b), which consists of interpolation using MLS and computing the IBM force has to be performed on the Lagrangian markers (centroids here) and this is done only on the centroids lying within the processors slab (see right panel of figure 2.13). This allocation is regardless of which immersed body it belongs to. This is achieved by first performing a check on the axial index of every centroid (stored in `pind[3,:,:]` and computed in step 1); for example, if the processor C_i is responsible for the slab `[1:N_1,1:N_2,N_3_start:N_3_end]` the following procedure is undertaken.

```
do i=1,N_particle
  do j=1,N_face

    if pind(3,j,i) >= N_start(myid).AND.pind(3,j,i) < N_end(myid)
        - Perform MLS interpolation around the centroid.
        - Compute IBM forcing.
    end if

  end do
end do
```

As explained in section 2.2, MLS interpolations require a support domain built from 3 Eulerian grid nodes in each direction. Thus the forcing computed from a centroid lying right next to a processor boundary would be stored in a halo layer and this is communicated to the neighbouring processors in step 3(c). Every processor adds the IBM forcing received from the halo cells of the neighbouring processors to the already existing forcing thus accounting for the forcing from the centroids lying on processor boundaries.

Step 4(a) involves computing the external forces on the immersed body (i.e. pressure and viscous forces) which are performed following the procedure described in section 2.2. The allocation of processor for computing the external processors is done in a similar manner to step 3(b). Here it is important to note that for centroids lying on the processor boundaries the probes may lie in the neighbouring processor. For example, a centroid belonging to processor C_i may have an axial index of `N_3_start` and the axial index of the corresponding probe would be `N_3_start-1`. Building a support domain around

`N_3_start-1` would require information from [`N_3_start-2, N_3_start-1, N_3_start`] i.e. at least two halo layers need to be stored by each processor.

```
do i=1,N_particle
  do j=1,N_face

    if pind(3,j,i) >= N_start(myid).AND.pind(3,j,i) < N_end(myid)
        - Compute probe and build support domain around the probe.
        - Perform MLS interpolation around the probe.
        - Compute pressure and viscous forces on faces.
        - Distribute the forces from faces to nodes.
    end if

  end do
end do
```

In step 4(b), we reduce the external forces ($\boldsymbol{F}_{\text{ext}}$) over all the triangle nodes immersed in the flow. `MPI_ALLREDUCE` is used to perform this operation which results in all the processors having information on the external forces acting on all triangular nodes. Here it is important to remember that the efficiency of the `MPI_ALLREDUCE` operation may depend on the system architecture and checks are necessary before proceeding to large scale runs with this algorithm. The total force acting on each triangular node is computed as the summation of the external forces (pressure + viscous) and the internal forces arising from the elastic potentials i.e. $\boldsymbol{F} = \boldsymbol{F}_{\text{ext}} + \boldsymbol{F}_{\text{int}}$; for the first time step the immersed body is in its reference state and all internal forces are equal to zero and in every succeeding time step F_{int} is the internal elastic forces computed in the previous time step. With this step every processor updates the position of the triangle nodes based on the total force.

Step 4(c) involves computing the internal elastic forces derived from the potentials on each immersed body. Since this requires the full body to be treated as a whole, we compute the location of the mean axial index of every individual immersed body from the information in the array `pind`. The processor responsible for this axial index takes care of computing all the internal elastic forces (i.e. in–plane deformation, out–of–plane deformation, volume constraint and area constraint) and computing the net internal force acting on each node belonging to its allocated immersed body. While computing the internal forces on each immersed body does not require any information from the Eulerian mesh, such an allocation ensures the computing load is distributed evenly across all processors. Also it is important to note that MLS interpolations which are the computationally expensive steps in this FSI–IBM code are still performed only by processors containing the Lagrangian markers. The pseudo code for this operation is given below.

```
do i=1,N_particle

    if z_ave(i) >= N_start(myid).AND.z_ave(i) < N_end(myid)
        - Compute forces from in-plane deformation.
        - Compute forces from out-of-plane deformation.
        - Compute forces from volume potential.
```

```
        - Compute forces from area potential.
        - Sum up forces from all potential on the nodes.
    end if

end do
```

In step 4(d), we reduce the internal forces ($\boldsymbol{F}^{\text{int}}$) over all triangle nodes with an `MPI_ALLREDUCE` operation similar to the operation in 4(b). With this we complete all the steps required for one full iteration of the flow solver and the IBM coupled with the deformation.

2.5.2 Scaling

In figure 2.14 we show the computational performance of the parallelization strategy just discussed. These simulations were performed on the thin nodes of the Dutch supercomputing facility 'Cartesius' where each node is composed of 2x12 core 2.6 GHz Intel Xeon E5–2690 v3 CPU's. As can be seen from the plots in figure 2.14 strong scaling is achieved up to 1000 cores. The Eulerian resolution was set to 720x720x3840 with a total of 25000 spherical particles each discretized using 320 faces, i.e. a total of 8 Million Lagrangian markers were simulated simultaneously. Due to global storage of the geometrical features and meta data of the Lagrangian markers, the memory consumption by the IBM–IP part of the flow solver for such simulation is approximately 600MB.

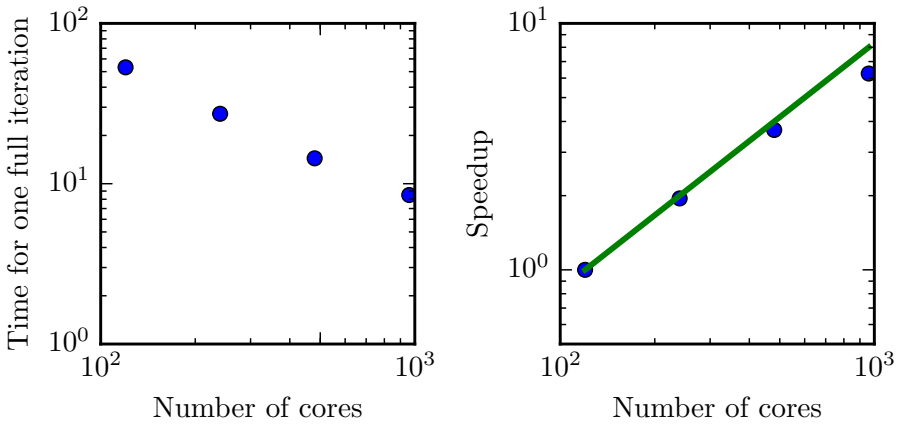

Figure 2.14: a) Scaling plot showing the time step for one full iteration of the solver versus the number of cores used. b) Corresponding speed up versus the number of cores.

For a given flow solver, the costliest steps in the IBM part of the solver are the ones involving MLS interpolation since each interpolation requires the construction of multiple coefficient matrices and a subsequent inversion of a 4x4 matrix (in 3D). For each Lagrangian marker (centroid) immersed in the flow two MLS interpolations are required; one at the Lagrangian marker itself to compute the IBM forcing and another at the position of the probe projected from the centroid which is used for the computing the value pressure and velocity gradients. Additional matrix operations are required for the velocity

gradients since instead of the shape function we need to compute the derivative of the shape function (Liu & Gu, 2005). On a single processor, increasing the number of Lagrangian markers by two times can result in a three to five fold increase in the simulation time. It is thus crucial to see how the parallel code performs with increase in the total number of Lagrangian markers or triangular faces.

In figure 2.15 we plot the non–dimensional time taken for one full iteration with increasing total number of faces for two different types of simulations. The time is normalized using the time taken for the first data point i.e. $N_{\text{face}} = 320$. For these simulations the Eulerian grid is kept fixed to 120x120x720 and a total of 120 cores were used. In the left panel of figure 2.15, the immersed bodies are kept fixed in position and shape i.e. the computation of the structural solver is fully eliminated. Such simulations are useful to compute the hydrodynamic forces acting on stationary bodies with a mean flow imposed in the domain. As can be seen, with increase in the number of faces there is negligible increase in the computational time. In comparison to simulations involving moving and deforming objects, IBM simulations with stationary and fixed bodies require only one MLS interpolation and this is the reason for the negligible time increase. On the right panel we show the increase in time for simulations involving both moving and deforming bodies. These simulations require an additional MLS interpolation at the probe and also the computation of shape function derivatives. For such simulations, a 100 times increase in the number of faces results in approximately 1.3 times increase in the computational time. This shows that the increasing cost of MLS interpolations on the Lagrangian markers can be offset by parallelizing the task over multiple processors.

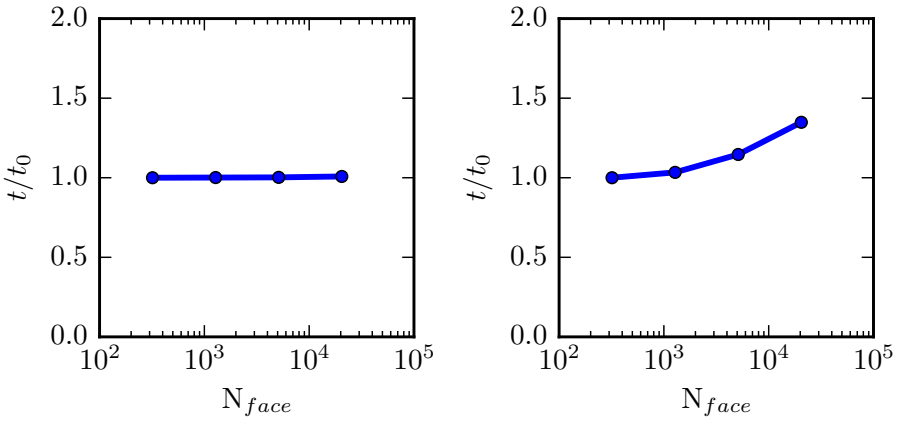

Figure 2.15: Time taken for one full iteration normalized using the time taken for the first data point versus the total number of triangular elements or faces immersed in the domain. In the left panel the immersed bodies are stationary and fixed in shape, while in the right panel the bodies can both move and deform.

2.6 Summary and outlook

In this chapter we have described the implementation of a finite–difference based flow solver capable of handling several deforming membranes where the deformation dynamics is computed through an interaction potential approach. An IBM based on MLS interpolation is used to enforce the boundary condition at the interface on the underlying flow, while the deformation dynamics is computed through minimizing the potential energy of a spring network spread over the surface of the immersed surface. The advantages of this approach, in comparison to conventional techniques, are its computationally efficiency and its great versatility. First we have discussed how it can be used to study multiphase flows involving deformation of thousands of drops and bubbles in highly turbulent flows; then we have shown another possible application to hemodynamics problems related to the deformation of the left ventricle coupled with mitral valve. In this latter case we have just introduced the subject that will be deeply analyzed in the following chapter, where we will study in detail the effects of different types (native and prosthetic mechanical or biological) of mitral valve on the intraventricular flow structure, paying attention to the valve dynamics and ventricle deformation.

Chapter 3

Flow structure in healthy and pathological left ventricles with natural and prosthetic mitral valves

Based on: Valentina Meschini, Marco D. de Tullio, Giorgio Querzoli & Roberto Verzicco, 'Flow structure in healthy and pathological left ventricles with natural and prosthetic mitral valves', to appear on *Journal of Fluid Mechanics*.

3.1 Introduction

The human heart is made of two separate volumetric pumps, the right and the left, respectively, shaded in blue and red in figure 3.1. The former is responsible for the pulmonary circulation, which controls the blood flow to and from the lungs, and therefore works with limited pressure differences ≈ 2000 Pa (15 mmHg). The left heart is instead the strongest since it feeds the systemic circulation that brings oxygenated blood to the whole body (except for the lungs and the heart itself). This implies that the left part has to withstand the largest pressure differences, between atrium and ventricle, that are in the range $1.6 - 2.1 \times 10^4$ Pa ($120 - 160$ mmHg).

The valves ensure the correct flow direction and prevent blood regurgitation. Those of the right heart are subjected to small fluid dynamic loads and usually are not impaired. In contrast, the aortic and mitral valves, that direct the blood from the ventricle to the aorta and from the atrium to the ventricle, respectively, are the most subjected to damage.

A very simple schematic of the whole heart is given in figure 3.1; here we limit the description to the dynamics only of the left part.

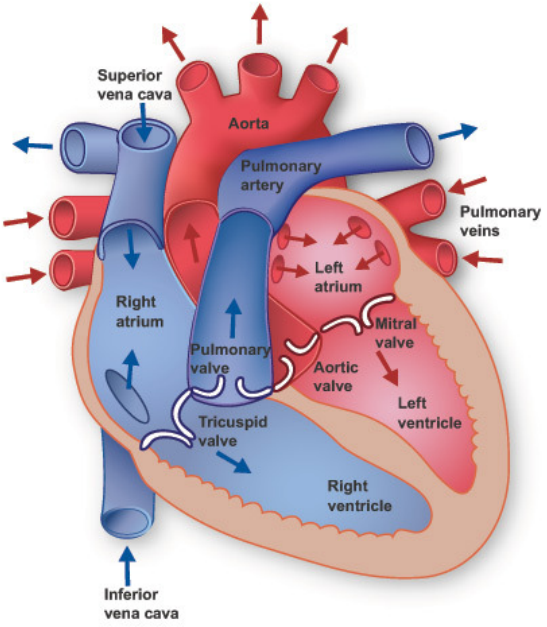

Figure 3.1: Schematic description of the heart functioning. (Picture adapted from www.texasheart.org)

During diastole the blood from the left atrium enters, through the mitral valve, the left ventricle and recirculates in it. As systole starts the myocardium contracts and the blood is ejected, through the aortic valve, from the left ventricle to the aorta from which it is distributed to the body. Although several surgical procedures are available to repair and remodel the natural valves, in some cases their replacement is unavoidable and, in those cases, choosing the optimal prosthesis is crucial. Worldwide 280000 valve replacements are performed each year and this number is constantly increasing with a projection of about 800000 by 2050 owing to the increasing age of the population and a

growing percentage of it accessing advanced medical care. Aortic and mitral valve replacement are almost equally distributed, (Pibarot & Dumesnil, 2009). However, while the former has already been the topic of extensive medical and scientific research, the latter has been less explored and its post–operative effects on the left ventricle dynamics still need to be analysed in details. The main reason for this difference is that the outflow of the aortic valve goes directly into the aorta that, even if a very complex and vital 'organ', operates passively. In contrast, the flow produced by the mitral valve interacts directly with the left ventricle whose dynamics is the result of the interaction between the active contraction/relaxation of the myocardium and the surface loads produced by the blood. Furthermore, the structure of the tissues composing the ventricular wall, and the ventricle as a whole, develop and change in response to the solicitations exerted by the intraventricular flow. This implies that any change in the flow through the mitral valve, either natural or prosthetic, produces an altered blood flow that, in turn, can lead to pathological conditions and ventricle impairing.

Accordingly, we aim to investigate how the flow structure inside the left ventricle is altered by a mitral valve replacement for different fractions of volume ejected by the left ventricle. This requires the simultaneous consideration of different prosthetic valve models (figure 3.2) and various levels of ventricle pumping efficiency. Concerning the first point two alternatives are available: Biological and mechanical valves. The former (figure 3.2b) are prosthetic devices made of biological tissues (bovine pericardium or porcine heart valves) and have three flexible leaflets differently from the native mitral valve which is made by two, asymmetrical, leaflets. These valves have good hemodynamics and reduced propensity to damage the blood cells (hemolysis) or produce clots (thrombogenesis), therefore they do not need lifelong anticoagulant treatments. The drawback is, however, that their lifetime is around $15 - 20$ years and they need to be replaced beyond this operating time. The semilunar mechanical valves (figure 3.2c), instead, are made of pyrolytic carbon. They regulate the flow direction by two rigid leaflets hinged to an annular frame. The main advantage of mechanical valves is their lifelong duration (about 80 years). Therefore they are indicated for patients with life expectation beyond 15 years. Their main drawback is the altered hemodynamics (Querzoli *et al.*, 2010; de Tullio *et al.*, 2009) which re res a lifelong anticoagulation therapy, to prevent clot formation, with its accompanying risk of bleeding and hemorrhagic events.

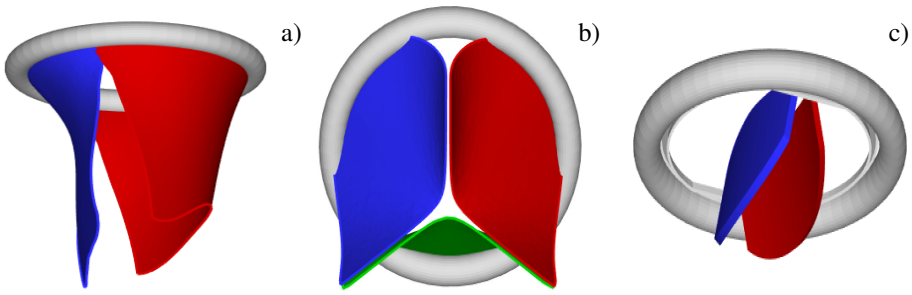

Figure 3.2: Different geometries of the mitral valve: a) natural, b) biological, c) mechanical.

The pumping function of the ventricle can be quantified by its ejection fraction (EF). Let $V^*(t)$ be the volume of blood in the ventricle during the heart cycle with a maximum V_M^* at the end of the diastolic phase, when the myocardium is fully relaxed, and a minimum V_m^* at the end of the systolic phase, when the myocardium ends its contraction. The difference $V_M^* - V_m^*$ is the amount of blood ejected from the ventricle during one cycle and the ratio $(V_M^* - V_m^*)/V_M^* = EF$ is the ejection fraction. Although this parameter has some variation among individuals, values $50\% \leq EF \leq 70\%$ are considered physiologic, $40\% \leq EF \leq 50\%$ pathological and $EF \leq 35\%$ life threatening.

Owing to the synergistic interaction between the mitral flow and the ventricle dynamics, it is natural to conjecture that the flow alterations induced by a prosthetic valve will have different impacts on the ventricular flow depending on its pumping efficiency. In the literature there is plenty of studies focusing on specific aspects of the mitral flow or on the mitral valve dynamics. Among many, Faludi *et al.* (2010), Querzoli *et al.* (2010) and Pedrizzetti *et al.* (2010) have underlined the strong influence the mitral valve has on the diastolic flow structure, and Einstein *et al.* (2005*b*), Griffith *et al.* (2009) and Wattona *et al.* (2008) have focused on the dynamics of mitral valve leaflets. Moreover Mcqueen & Peskin (2000) and Mihalef *et al.* (2011) have studied the effect of combining realistic intraventricular flow with physiological mitral valve using patient specific models without FSI. Vukićević *et al.* (2012) underlined the role of the asymmetrical structure of the native mitral valve and investigated the flow generated by a mechanical, asymmetrical prosthesis. Recently, Seo *et al.* (2014) have analysed how the morphology and kinematics of the mitral valve can affect the left ventricular flow using a physiological mitral valve. The motion of the leaflets was however prescribed, thus the synergistic interaction of flow and structure dynamics is imposed rather than captured by the solution.

In order to fill this gap and to simulate the complete system with the minimum number of assumptions, in this chapter a full FSI model for the left ventricle and the mitral valve is used, obtaining a more realistic representation of the phenomenon. In this way, both, the valve and the ventricle dynamics are determined by their interaction with the flow which, in turn, depends on the motion of the boundaries. To limit the computational effort we focus on two representative values of EF, 60% and 40%, respectively, for healthy and pathological ventricles. Each case is simulated over several heart cycles (10 for all production runs and 5 for the refined cases) and the system dynamics is phase averaged. First the configuration with the natural mitral valve is investigated, either for healthy and for impaired ventricles, and it is used as a reference case. Then the flows with a prosthetic biological and a mechanical bileaflet valves are analysed and their dynamics compared. By running additional dedicated simulations we assess also the differences between Newtonian and non–Newtonian fluid models for the blood and the sensitivity of the dynamics to the material properties of the valve leaflets. We believe that this study can give an important contribution to the assessment of the performance of biological and mechanical prosthetic valves for different ventricle efficiencies and this is a crucial information for the surgeons in the decision process of the heart valve replacement.

The structure of the chapter is as follows. In the next section the problem, the numerical model and its experimental counterpart are described. In the

same section also the the flow parameters, the validation and the convergence checks are given. In section 3 the results are presented and discussed, starting from the physiological flow produced by a natural valve. This will serve as a reference case against which evaluating the flows generated by biological and mechanical valves. In the same section additional simulations are presented to assess the robustness of the reference results to the specific fluid model (Newtonian vs shear–thinning non–Newtonian), to the thickness and material properties of the leaflets and to the geometrical lumen of the mitral channel. A general comment of the results is given in section 4 together with a discussion in the context of the clinical literature. The closing remarks, some comments about how the present physical model compares with the real flow in the heart and the perspectives for future studies are given in the final section.

3.2 The problem

3.2.1 Numerical and experimental set–up

The set–up of the problem is given in figure 3.3 showing the experimental realization and its numerical counterpart. Figure 3.3b focuses on the core of a pulse duplicator of the systemic circulation described in section 2.4.1; on an AC electrical motor, controlled by an inverter, is splined a cam that, in its rotary motion, pushes a piston driving water into a sealed plexiglass tank with a periodic mean velocity $U^*(t)$ (figure 3.4a). This flow induces a passive variation of the total volume of the system that, owing to incompressibility, is copied by the ventricle (figure 3.4b). The time evolution of $U^*(t)$ in figure 3.4a is that of a pathologic elderly heart in which the passive filling phase (E–wave) is much stronger than the active counterpart (A–wave) when the left atrium contracts. The cross–section of the piston and the law $U^*(t)$ determine the stroke volume that, in the experiments is fixed at $V_e^* = 90$ cm^3; the minimum ventricle volume V_m^*, in contrast, can be varied continuously by adding or removing water from the sealed Plexiglas box. In this way the ejection fraction $EF = V_e^*/(V_e^* + V_m^*)$ can be adjusted to the desired value.

The ventricle is a $2-3$–millimeter thick membrane made by a transparent silicon rubber of density $\rho_s^* = 1.04$ gr/cm^3 and Young modulus $E^* = 1.5$ MPa. The density of the rubber is almost identical to that of the myocardium (1040 Kg/m^3 vs 1060 Kg/m^3) while it is three times stiffer than the biological tissue ($E = 1.5$ MPa vs max $E = 0.5$ MPa) and this difference has been compensated by making the ventricle thickness ($\approx 2 - -3$ mm) about three times smaller than that of the myocardium (≤ 1 cm). This is however still far from the real case when considering that the myocardium is anisotropic, because of the fiber orientation, and hyperelastic (nonlinear). In addition during the heart cycle the myocardium changes its stiffness from 0.02 up to 0.5 MPa and it contracts actively rather than passively adapting to the imposed inflow as in the present study.

The ventricle is connected to two rigid pipes of inner diameter 19 mm and 24 mm that mimic, respectively, the aortic and mitral channels. The distal extrema of the pipes accommodate two rigid rings (dashed line in figure 3.3b) in which different valves can be fit; any of the valves of figure 3.2, or a simple check valve, can be used in both positions. For the present experiments a

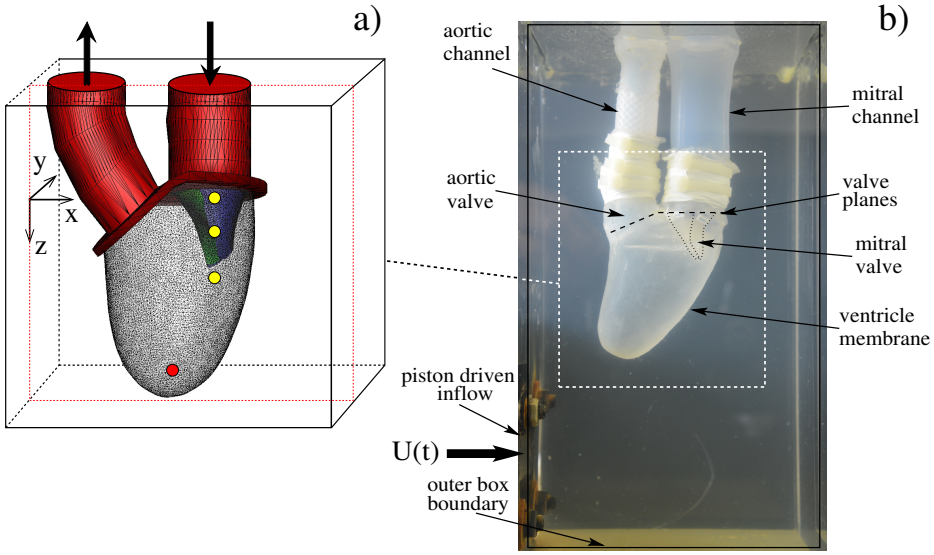

Figure 3.3: a) Numerical set–up for the left ventricle. The bullets indicate the position, in the symmetry x–z plane, of some relevant numerical probes: the red one is the 'apex' probe used to detect the apical flow stagnation; the yellow ones are used to compute the transvalvular pressure drop and the velocity in the mitral jet; the green one is located at the ventricle centroid ($x = 0.1$, $y = 0$, $z = 1.15$), at the end–systole configuration. b) Experimental set–up containing the left ventricle.

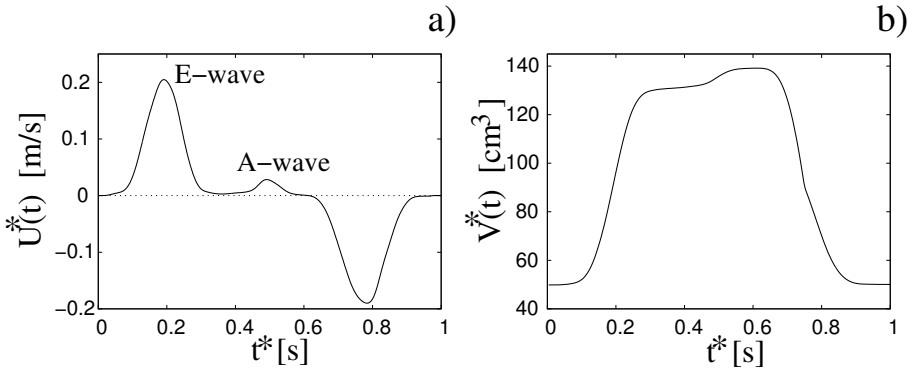

Figure 3.4: a) Time evolution of the inflow/outflow velocity $U^*(t)$ over a cardiac cycle. b) Time evolution of the volume $V^*(t)$ of the left ventricle. Both plots are in dimensional units.

check valve was used in aortic position whereas a model of the native valve, made of silicon rubber, was placed in mitral position.

The working fluid is water whose kinematic viscosity $\nu^* = 1.2 \times 10^{--6}$ m^2/s is about four times smaller than that of the whole blood (considered as a Newtonian fluid and with a hematocrit, the volume fraction of solid cells over the total volume, of 45 %). Being the Reynolds number $Re = U_M^* D^*/\nu^*$, and $Wo = D^*/\sqrt{T^*\nu^*}$ the Womersley number, with U_M^* the maximum of $U^*(t)$ over the diastolic phase, T^* the period of the cardiac cycle and D^* the diameter of the mitral channel, with a full scale model ($D^* = 24$ mm) the velocity U_M^* has to be four times smaller than in a real heart if we have to operate in dynamic similarity. In our experiment this implies that the cam frequency must be four times smaller than that of the heart in order to operate in dynamic similarity. Accordingly, the rotation rate was fixed to 15 rpm on order to reproduce a heart at 60 beats per minute. For an ejection fraction $EF = 60\%$ we have $Re = 4229$ and $Wo = 11$ which are typical values for a physiologic condition.

The fluid was seeded with pine pollen particles and the system illuminated by a laser sheet so that the flow in the vertical x–z symmetry plane could be recorded by a high–speed camera at 1000 fps. An advantage of having an experiment running four times slower than the real phenomenon is the higher time resolution of the flow measurements achievable within a given frame rate of the available camera. This time stretch, however, affects also the fluid/structure interaction that, is not in dynamic similitude unless the elastic properties of the material are changed. We note that in the present set–up all the structures are very thin and the deformable ones relatively soft; this implies that their dynamics is dominated by the balance between external loads and added mass (see the results of section 3.3.3) and not on the density and stiffness of the material. Of course the latter would change considerably the magnitude and distribution of the structural internal stresses that have not been investigated in this study. Images (1024×1280 pixels, 0.11 mm per pixel) have been processed by the variant of the classical PIV algorithm, described in details in Falchi *et al.* (2006), in order to compute the two–dimensional, instantaneous velocity field. The final size of the interrogation windows was 31×31 pixels, with a 50% overlap. The uncertainty in the particle displacement measurement was about 0.1 pixel. An evident advantage of having an experiment running four times slower than the real phenomenon is the higher time resolution of the flow measurement achievable within a given frame rate of the available camera.

The computational model is aimed at reproducing as close as possible the above described experiment. In the set–up of figure 3.3a it is shown the computational domain that is periodic in the two horizontal directions and allows for inflow/outflow in the vertical ones. Over the upper surface the inflow is imposed through the mitral channel according to $U(t)$ when it is positive and an outflow through the aortic channel when $U(t)$ is negative. The flow rate through the bottom wall is adjusted at each time step so to ensure the incompressibility and to preserve the total fluid volume. In the numerical model all the variables are presented in non dimensional form with the velocities scaled by U_M^*, the lengths by D^* and the times by the cycle period T^*; the non dimensional variables are indicated without the superscript $*$.

The mitral and aortic channels together with the valve planes (in red in figure 3.3a) are modeled as a rigid structure that is used as a frame to anchor the deformable ventricle and the valve leaflets, respectively in gray, green and blue in 3.3a.

In the experimental set–up a simple check valve was placed in aortic position. In order to replicate this simple behaviour we have used a porous medium in the aortic channel with a time–dependent porosity (de Tullio *et al.*, 2011*c*). During diastole the medium porosity goes to zero thus obstructing the duct and preventing the fluid from entering the aortic channel, during systole the porosity tends to infinity and the fluid can leave the ventricle to enter the aorta.

The reference frame is as shown in figure 3.3a with the positive z pointing vertically downward and the origin $z = 0$ at the mitral annulus. The x–z plane at $y = 0$ is a symmetry plane for the system.

The flow volume is disseminated with 36 numerical probes that provide a continuous pointwise sampling of all velocity and vorticity components and of the pressure. The most relevant are the 'apex' probe (the red bullet in figure 3.3a at $z = 2.5$), the 'centroid' probe (the green bullet in figure 3.3a at $x = 0.1$, $y = 0$, $z = 1.15$) and the three 'mitral' probes (the yellow bullets at $z = 0$, 0.75 and 1.5) that are used to analyse the time evolution of velocity and pressure.

3.2.2 The numerical method

The computational model is basically that described by de Tullio & Pascazio (2016) and Spandan *et al.* (2017), which consists of a flow solver two–way coupled with a structure solver; the resulting assembly is computationally efficient and flexible enough to allow for the solution of a wide range of problems ranging from multiphase flows to turbulence in complex geometries. All the details of the algorithms, the validations and the convergence checks can be found in the above references, only the main features are summarized here.

In this study the package has been used for a bio–fluid–dynamic problem, namely the blood dynamics in a realistic left heart ventricle with several different types of mitral valves and physiological flow parameters. The flow is incompressible and viscous thus its motion is described by the Navier–Stokes equations, which in non dimensional form read:

$$\begin{aligned} &\frac{\partial \mathbf{u}}{\partial t} + \mathbf{u} \cdot \nabla \mathbf{u} = -\nabla p + \nabla \cdot \boldsymbol{\tau} + \mathbf{f}, \\ &\nabla \cdot \mathbf{u} = 0. \end{aligned} \tag{3.1}$$

Here $\mathbf{u}$ is the velocity, p is the pressure and $\mathbf{f}$ is a specific body force term that is used, within the immersed boundary context, to enforce the boundary condition at the various fluid–structure interfaces. In the present study for all but one case the blood has been considered as a Newtonian fluid since it is known that its non–Newtonian features become relevant only in vessels of diameter smaller than $15 - 20$ red blood cell diameters ($\sim 80 - 100$ μm) (Siginer *et al.* (1999)): in these cases the viscous term of equation (4.1) reads $\nabla \cdot \boldsymbol{\tau} = \nabla^2 \mathbf{u}/Re$. The flow solver, however, can simulate also more complex constitutive relations as already done in De Vita *et al.* (2016). In one case, described in section 3.3.2, in order to show that indeed for the present problem

the non–Newtonian nature of blood plays only a minor role on the overall dynamics, the Carreau–Yasuda shear–thinning model has been used. In this fluid the kinematic viscosity ν depends on the magnitude of the rate–of–strain tensor $S = |\mathbf{S}| = |\nabla\mathbf{u}+\nabla\mathbf{u}^T|/2$ according to $\nu(S) = \nu_\infty+(\nu_0-\nu_\infty)[1+(\lambda S)^2]^b$. This function gives a decreasing viscosity for increasing shear stresses with the plateau ν_0 and the asymptotic values ν_∞, respectively, for the limiting cases $S \to 0$ and $S \to \infty$. With this fluid model the viscous term of equation (4.1) becomes $\nabla \cdot \boldsymbol{\tau} = \nabla \cdot [2\nu(S)\mathbf{S}]/(\nu_\infty Re)$, the Reynolds number being computed using the ν_∞ viscosity. As already done in De Vita *et al.* (2016), also in the present study we have selected the parameters of the fluid model to mimic an adult healthy male with an hematocrit (ratio of the cell volume to the whole blood volume) of 40% which yield $\lambda = 3.313$s, $b = -0.3216$, $\nu_\infty = 3.7 \times 10^{-6}\mathrm{m}^2/\mathrm{s}$ and $\nu_0 = 4.3\nu_\infty$.

The structure deformation is solved using a spring–mass method which is based on an interaction potential approach (Tanaka *et al.*, 2012) and applied to different problems by de Tullio & Pascazio (2016) and Spandan *et al.* (2017). Here, the wet surfaces of the ventricle and mitral valve are discretized using triangular elements with a uniform distribution of the body mass on their vertices. The nodes are connected by springs of elastic constant k_e and two triangles sharing an edge have a bending stiffness k_b. When the resulting network deforms owing to external forces, internal potential energy is stored into the system according to $W = k_e(\ell - \ell_0)^2/2 + k_b(1 - \cos(\theta - \theta_0))$ where ℓ and θ are, respectively, the vector connecting two vertices of an edge and the angle between the normals of two triangles sharing that edge; ℓ_0 and θ_0 are the same quantities in the reference stress–free configuration (figure 3.5). Once the potential energy for each node is known the internal forces in the structure can be computed through $\mathbf{F}_{int} = -\nabla W$ that, together with the external forces $\mathbf{F}_{ext}$ (hydrodynamics loads, gravity and other body forces), allows for the solution of the second Newton's law for each node $m_n\ddot{\mathbf{x}} = \mathbf{F}_{int} + \mathbf{F}_{ext}$ with m_n the mass associated to the node. From the acceleration, by successive integrations the velocity $\dot{\mathbf{x}}$ and the position $\mathbf{x}$ of the nodes is computed thus yielding the updated configuration of the structure.

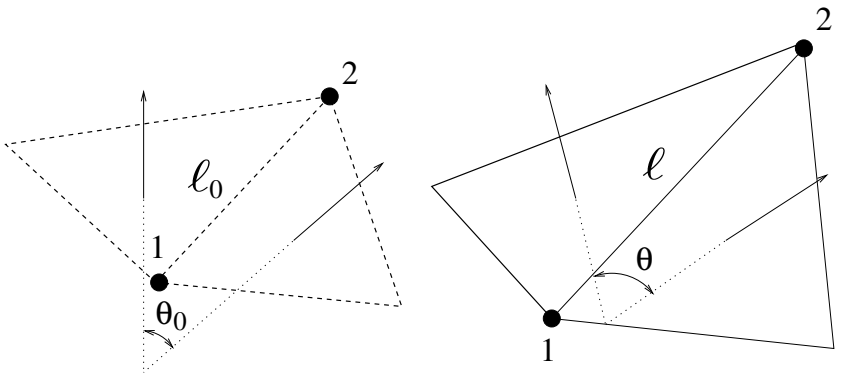

Figure 3.5: (left) Undeformed and (right) deformed configuration of the structure.

In the present study, in which the structures are essentially isotropic membranes, the elastic constants k_e and k_b are computed using the Van Gelder model (1998) via $k_e = Eh(A_1 + A_2)/\ell_0^2$ and $k_b = B2/\sqrt{3}$ being E and B, re-

spectively, the Young modulus of the material and the bending stiffness of the structure, h the local membrane thickness, A_1, A_2 the area of the two triangles sharing the edge ℓ_0. As shown in de Tullio & Pascazio (2016) the method can be extended to non–linear as well as anisotropic materials; this is certainly the case of the biological tissues that are hyperelastic and orthotropic. In this investigation, however, with reference experiments performed with rubber silicon as membrane material this additional feature was not necessary and it has not been activated in our simulations.

The presence of the structure on the fluid, and vice versa, is enforced through IBM that avoid body fitted meshes and handle moving and/or deforming boundaries within the ease and efficiency of simple meshes. The present problem involves rigid as well as deformable structures therefore two different IBM are implemented in the code; the direct–forcing of Fadlun *et al.* (2000) is used for the rigid, still parts since the method is robust, computationally inexpensive and it does not require a fine and even triangulation of the surface. On the other hand, for the moving and deformable surfaces the MLS approach of Vanella & Balaras (2009) is used because, even if computationally more expensive, it yields smooth hydrodynamic loads at the immersed interfaces that result in a more accurate description of the structure dynamics.

All the ingredients described above are controlled by a FSI algorithm that is implemented either in the 'strong' and in the 'loose' coupling mode. In the former, the fluid and structure problems are solved together as a single large dynamical system through an iterative procedure, while in the latter the fluid is solved first and the generated hydrodynamic loads are used to update the structure in which the fluid evolves at the successive time step. The strong coupling is robust and reliable although it is computationally demanding since it requires iteration steps (typically $2-4$) between fluid and structure solvers (de Tullio *et al.* (2009)). In contrast, the loose coupling approach is considerably faster although it can easily become unstable especially when used for problems, like the present one, where the added mass plays an important role. After an extensive series of preliminary simulations, convergence checks and validations, it has been determined that the most effective strategy is a loose coupling approach combined with a time substepping for the structure dynamics. In few words, from the flow and structure at the time t^n the flow at the new time ($t^{n+1} = t^n + \Delta t$) is computed; the hydrodynamic loads at the old and new time are then used to advance the structure with a time substep $\Delta t_s = \Delta t/S$, S being the number of substeps, until the time t^{n+1} is reached. This procedure needs the flow solution and the IBM only once per time step and requires multiple solutions only of the structure part that, being much faster than the rest, does not penalize the overall performance.

Since the present problem involves the dynamics of membranes in a fluid, an important component of the simulation is the model of their contact. A common practice is to introduce a repulsive force that increases as the distance between two bodies decreases (Tanaka *et al.*, 2012) to induce a 'rebound' when they get close enough. This would be very easy to prescribe in these simulations owing to the definition of forces through potentials. However, when a heart valve closes, the leaflets must stay in contact in order to prevent the regurgitation and the approach based on the repulsive force generates instabilities and stiffens the numerical problem. As an alternative we have

defined, over the computational mesh, an array that is null in the fluid phase and assumes a specific (integer) value in the cells occupied by each body. Its values are updated every time step and when, during the integration, a triangle ends up in a non null cell it means that the position is already occupied by another triangle. In this case the velocities of both surface elements are set to their average so that they can still freely move together in space but cannot compenetrate. On the other hand, when the system dynamics brings two contacting triangles far apart they can evolve according to the computed trajectory; we will see in the following that this approach allows the valve to close without prescribing a contact surface but, at the same time, it prevents the compenetration between the leaflets and between leaflets and ventricle.

Before concluding this section, we wish to mention that at the initial stage of this study, in order to save computational time, we have tried to prescribe the motion of the valve leaflets and to limit the FSI only to the ventricle dynamics. This approach resulted in considerable computational savings (above $60 - 70\%$) but it yielded results that were strongly dependent on the plausibility of the assigned (guessed) leaflet motion. Any mismatch between the true and the assigned leaflets position resulted in the generation of vortex structures that were shed from the valve and propagated into the flow. In addition we will see that there is a substantial cycle–to–cycle variation in the flow, therefore even if the valve dynamics is properly guessed in a cycle, it might be not in another thus spoiling the overall quality of the solution.

3.2.3 Simulation parameters, grid convergence and experimental validation

All the numerical simulations discussed in this chapter have been run for a set–up as in figure 3.3a on a mesh of 129^3 nodes evenly distributed in all three directions. The ventricle has been discretized by 3×10^4 triangles while the two leaflets of the natural mitral valve (figure 3.3a) have a total of 8×10^3 triangles. The Lagrangian (triangle) resolution is about 70% the local Eulerian grid spacing, in order to correctly impose the boundary conditions on the bodies. The time integration has been performed at constant Courant number $CFL = 0.2$ with a dynamic time step that adjusts during the integration so to maintain the CFL constant. The substepping for the integration of the structure is fixed at $S = 50$. The specific values of the time step size depend on the ejection fraction of the ventricle; typical figures for $EF = 40\%$ ($EF = 60\%$) are 1.5×10^4 (3×10^4) time steps per cycle with a single–processor equivalent CPU time of ≈ 20 h (≈ 40 h). The computational load increases steeply as the simulation is refined: For a run at $EF = 60\%$ on a mesh of 193^3 nodes with 4.2×10^4 triangles for the ventricle and 1.2×10^4 for both leaflets the number of time steps per cycles ramps up to 5×10^4 and the single–processor equivalent CPU time to ≈ 170 h. For the same physical case, in a further refined simulation, the number of computational nodes has been increased to 257^3, the triangular elements for all the structures to 6.8×10^4 and the required number of time–steps per cycle increased to $\approx 9.2 \times 10^4$ and the single–processor equivalent CPU time slightly smaller than 2000 h. Owing to the large computational cost of the refined cases the simulations on the 193^3 and 257^3 grids have been run 'only' for 5 heart cycles while all the other production cases for 10 heart cycles.

As an aside we note that the steeply increasing CPU time requirement for more refined Eulerian and Lagrangian meshes makes the parallelization of the computational method unavoidable as detailed in Spandan *et al.* (2017).

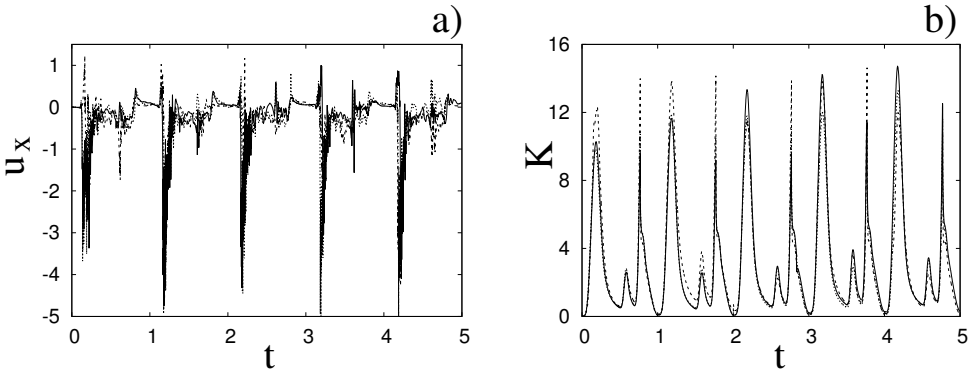

Figure 3.6: a) Instantaneous values of x–velocity component at the probe placed at the apex of the left ventricle. b) Kinetic energy of the flow inside the left ventricle. ····· grid with 257^3 nodes, ---- grid with 193^3 nodes, —— grid with 129^3 nodes. Inflow/outflow curve as in figure 3.4a.

Figure 3.6 shows the time series for the x component of the velocity sampled at the ventricle apex probe (see figure 3.3a) and of the kinetic energy of the flow inside the ventricle: the results are shown for the very fine (257^3), refined (193^3) and the basic (129^3) cases. There is substantial agreement among the results although it can be noted a considerable cycle–to–cycle variation that makes difficult the instantaneous comparison of the various quantities. This is due to the dynamics of the small scales that are produced by the turbulent cascade transferring energy from the largest flow scales up to the smallest dissipative structures. The small flow scales tend to have chaotic dynamics and can only be described statistically. In the present case, in order to filter out these turbulent fluctuations, the data have been phase averaged over 10 cycles (5 for the finer grids) and the results are reported in figure 3.7ab evidencing an improvement of the agreement that, however, still shows non negligible differences. For this reason, in figure 3.7a, in addition to the phase averaged data, three instantaneous profiles from each case are reported in the background. It can be noted that the amplitude of the instantaneous fluctuations can be up to five times bigger than the differences between the phase averaged profiles thus suggesting that it is the insufficient statistical convergence rather than the inadequate spatial resolution that produces the discrepancies. As a confirmation of this conjecture we note that the largest deviations occur in those parts of the cycle where the fluctuations are the largest and not all over the cycle. Additional evidence of the resolution quality comes from the instantaneous flow snapshots and the spatial profiles (later shown in this chapter) which do not evidence the δ–waves (or wiggles) that typically appear when an energy–conserving integration scheme is employed with coarse spatial resolution.

Since in these simulations not only the flow but also the structure dynamics is part of the solution, in figure 3.7cd we report the time evolution of the $\overline{X}$– and $\overline{Z}$–centroids of the ventricle obtained from spatial averages over instantaneous configurations and phase averages over the cycles.

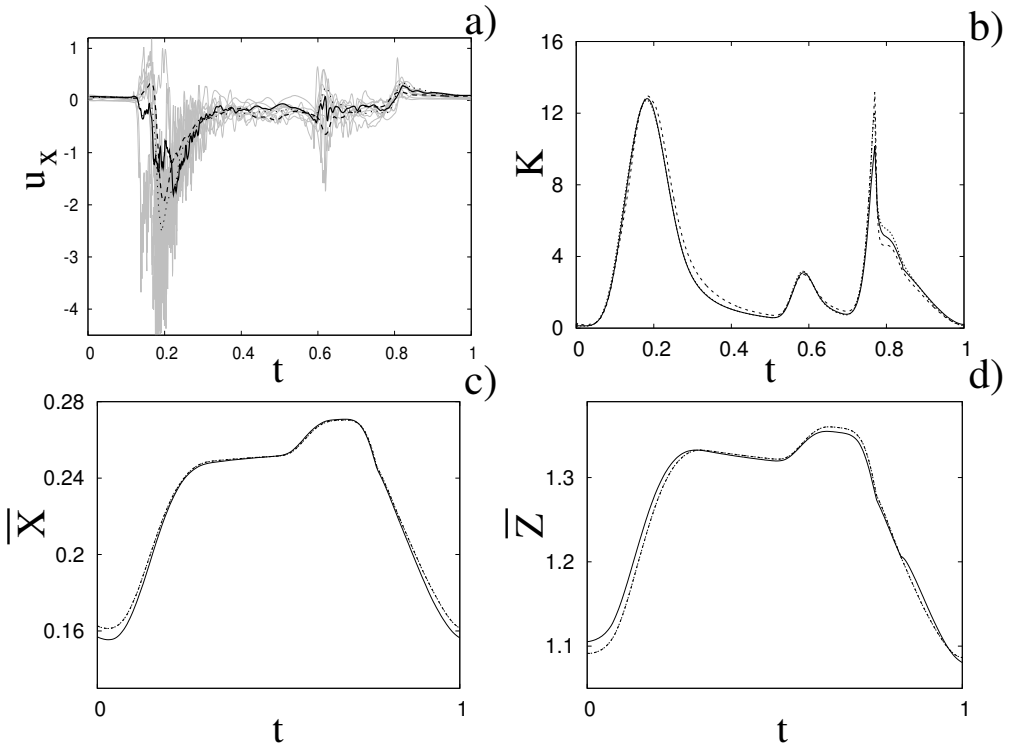

Figure 3.7: a) Phase–averaged values of x–velocity at the apex probe. b) Phase–averaged kinetic energy of the flow inside the ventricle. c) Phase averaged X–centroid of the ventricle contour. d) Phase averaged Z–centroid of the ventricle contour. ····· grid with 257^3 nodes, ---- grid with 193^3 nodes, —— grid with 129^3 nodes. Inflow/outflow curve as in figure 3.4a.

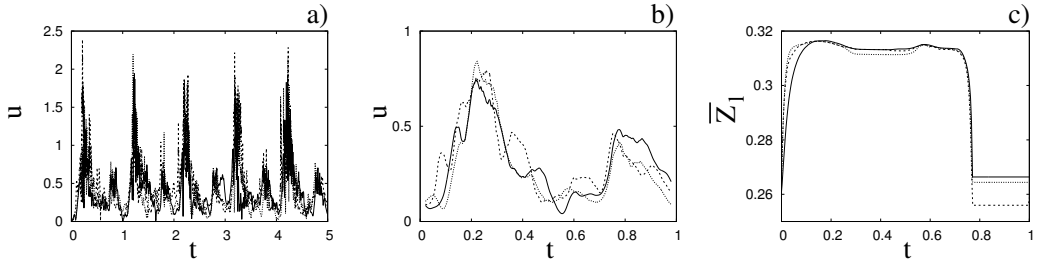

Figure 3.8: a) Instantaneous values of the velocity magnitude at the probe placed at the ventricle centroid (green probe of figure 3.3a). b) The same as a) but for phase–averaged velocity. c) Phase–averaged Z–centroid of the posterior leaflet of the mitral valve. ····· grid with 257^3 nodes, ---- grid with 193^3 nodes, —— grid with 129^3 nodes. Inflow/outflow curve as in figure 3.4a.

An additional quantity that has been monitored in this grid refinement check is the evolution of the velocity magnitude at the probe located at the centroid of the ventricle and the instantaneous as well as the phase–averaged values are reported in figure 3.8. Again, it can be noted a considerable cycle–to–cycle variation of the dynamics that makes the instantaneous values difficult to compare quantitatively even if the qualitative behaviour looks similar. Nevertheless, when the data are phase–averaged, the large fluctuations cancel

out and similar values are obtained. Also in this case the agreement between the three cases is more than satisfactory thus giving us confidence that the mesh for the simulations was adequate for the investigated parameter range. Also the motion of the valve leaflet results properly captured by the the combination of Eulerian/Lagrangian meshes of this study as shown in figure 3.8c for the posterior mitral leaflet. Of course an even better agreement could be obtained by increasing the number of simulated cycles to further smooth the phase averaged profiles; on account of the computational cost of the more refined cases however computing more than 5 cycles has not been a practical option.

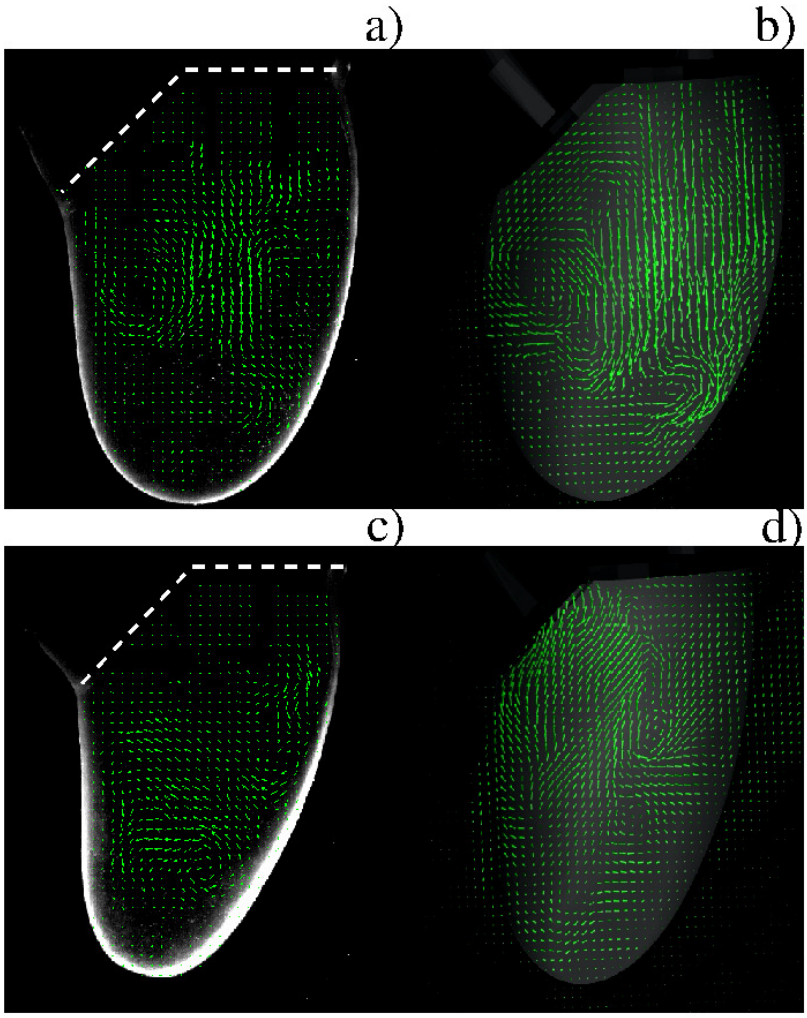

Figure 3.9: Comparison between experimental measurements (a), c)) and numerical results (b), d)) of the flow inside the left ventricle, respectively at the peak of the E-wave $t = 0.2$ and late systole $t = 0.9$. Inflow/outflow curve as in figure 3.4a.

Before concluding this discussion on the grid refinement check, it is worthwhile to mention that the Reynolds number $Re = 4229$ of the flow is computed using the peak velocity of the E–wave (figure 3.4a) that lasts only for a small fraction of the cycle. In this problem the cycle–averaged velocity is zero and

its rms is only 0.158 V_{peak} with the Reynolds number reduced proportionally. In addition the flow is pulsatile and the time window during which the Reynolds number remains large is too short to allow the flow to transition to fully developed turbulence (in which the energy cascades down up to the Kolmogorov scale). This implies that the usual order of magnitude estimates used for homogeneous isotropic turbulence of for statistically steady flows do not apply directly here and the only reliable check is a grid refinement as above described.

Of course, even if the output of the numerical code is grid independent this does not imply that the results are physically reliable and that they reproduce correctly the intended problem. For this reason we have also compared the numerical data with an ad hoc laboratory experiment run for identical dynamical conditions. We measured the instantaneous two–dimensional velocity field in the x–z symmetry plane and the shape of the ventricle that are shown for representative phases of the cycle in figures 3.9–3.11. It can be observed that the dynamics of the main jet and the main recirculations are satisfactorily matched and also the motion of the ventricle compares well.

Also satisfactory can be considered the comparison of the horizontal profiles of vertical velocity extracted at the symmetry plane $y = 0$ in a section at $z = 1$ during the diastole and systole (figure 3.10). When evaluating the quality of the agreement it should be considered that while the numerical data are phase averaged over 10 cycles, the experimental points are extracted from a single snapshot since quantitative acquisitions were run only for one cycle. This implies that for a phase of the cycle when the flow rate is stagnant or further downstream in the ventricle where the fluctuations dominate the velocity field, the same comparison as in figure 3.10 gives less satisfactory results.

As already evidenced in figure 3.6, the small–scale dynamics shows some differences that, however, should be ascribed to cycle–to–cycle variations rather than to mismatches between the numerical simulations and the experiment.

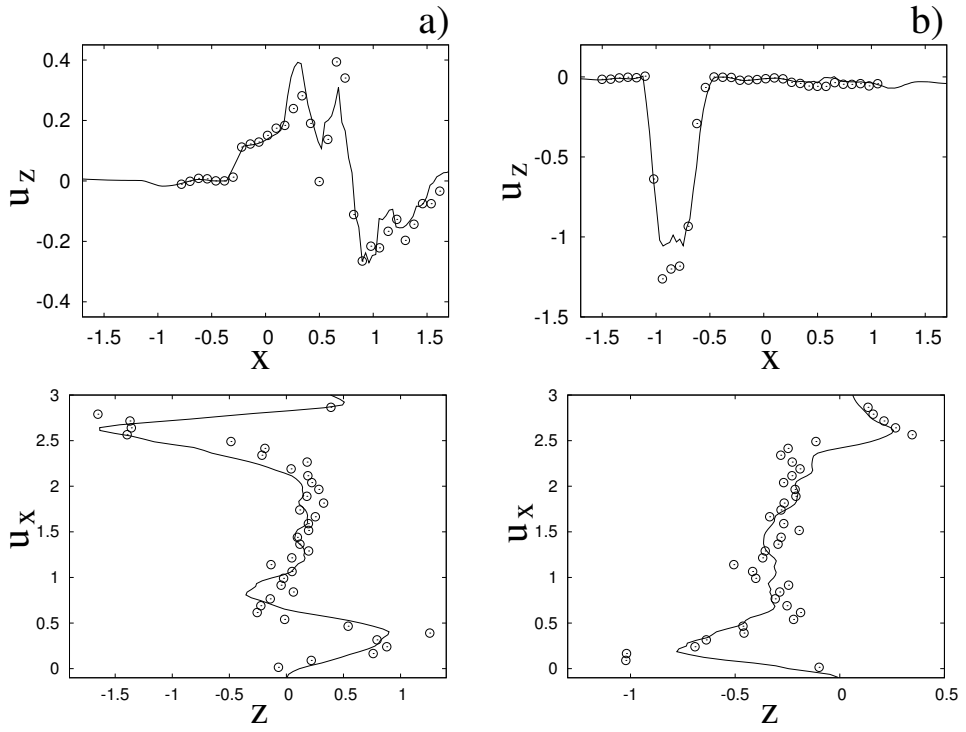

Figure 3.10: Comparison between experimental measurements ($\circ$) and numerical results (——) for velocity profiles in the symmetry plane ($y = 0$). Top, horizontal section at $z = 1$: a) E-wave $t = 0.25$, b) peak systole at $t = 0.8$. Bottom, vertical section at $x = 0$: c) E-wave $t = 0.25$, d) peak systole at $t = 0.8$. The velocities u_x and u_z are normalized with the peak value of the E–wave.

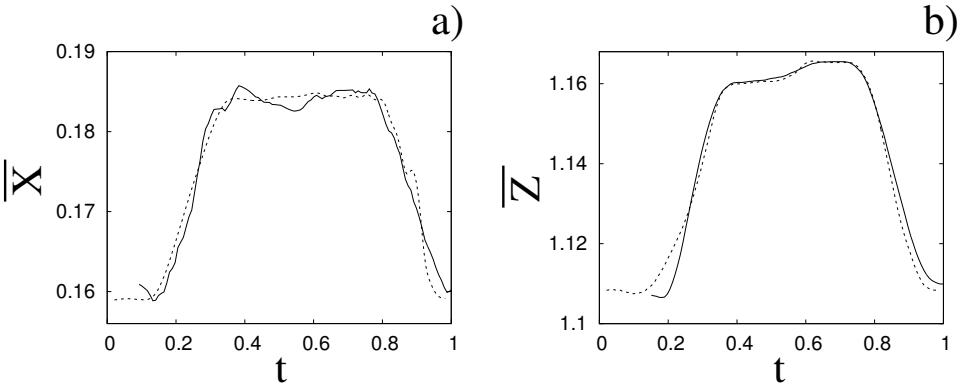

Figure 3.11: a) Phase–averaged X–centroid of the ventricle contour. b) Phase–averaged Z–centroid of ventricle contour. —— numerical, ---- experimental results. Inflow/outflow curve as in figure 3.4a.

3.3 Results

In this section the results obtained for two different ejection fractions and three types of mitral valves are discussed and compared. The first reference case, that will be used as a guideline to distinguish between physiologic and pathologic behaviours, is that of an efficient ventricle ($EF = 60\%$) with a

natural mitral valve (figure 3.2a) that is the normal condition for a healthy human being. In this case the flow rate during the cycle is that shown in figure 3.12 with a ratio of the inflow peaks at the E– and A–waves ≈ 0.5.

In a successive section the same healthy ventricle configuration will be simulated with a non–Newtonian shear–thinning (Carreau–Yasuda) fluid model in order to validate the Newtonian fluid assumption used for the rest of the chapter.

Section 3.3.3 is devoted to assess the sensitivity of the solution to the material properties and membrane thicknesses used to model the natural and biological valves. This analysis has been performed since there is a lot of variability among individuals of the biological tissue properties and if the solution were too sensitive to a specific set of values any conclusion should be limited only to that specific case and would not be general. In the same section also the effects of a reduced section available to the flow (stenotic valve) are briefly described to further stress the importance of comparing different valve models within the same mitral orifice area.

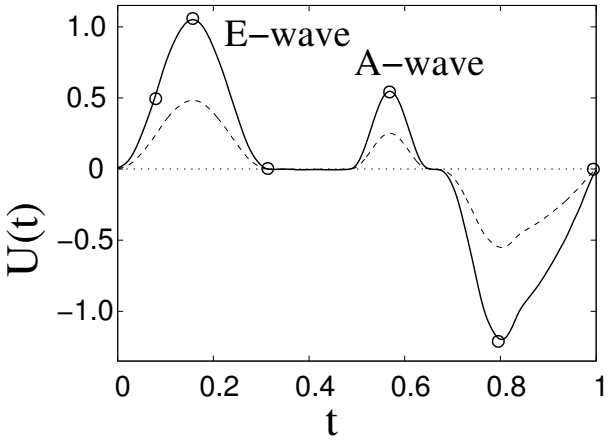

Figure 3.12: Flow rate in the ventricle $U(t)$ during the cycle. —— $EF = 60\%$, ---- $EF = 40\%$. The $\circ$ on the $EF = 60\%$ line indicate the representative times of the cycle in which the solution is shown later.

The flow in a ventricle with low pumping efficiency (figure 3.12, dashed line) will be then considered in order to assess the effect of a deteriorated ejection fraction, characterizing an unhealthy ventricle, on the system dynamics. As already mentioned the Reynolds number for $EF = 60\%$ is $Re = 4229$ and it is based on the dimensional peak velocity at the E–wave. If the same velocity were used to compute the Reynolds number at $EF = 40\%$ a smaller value would be obtained (≈ 2000). However, in order to have a more immediate comparison between the two cases, we have decided to leave the Reynolds number fixed at $Re = 4229$ and to rescale the inflow/outflow velocity profile as in the dashed line of figure 3.12.

Both ventricle conditions have been then evaluated either with a trileaflet biological and with a bileaflet mechanical mitral valve to analyse the effects of a prosthetic valve on the ventricle and flow dynamics.

It is worth mentioning that all the valves (figure 3.2abc) are such to fit into a mitral orifice of $D^* = 24$ mm and their geometries have been obtained by drawings and anatomical sketches. In reality, depending on the specific valve

model (stented or stentless, curved or straight leaflets, etc.) and on the surgical implantation technique (balloon–expandable transcatheter or open heart) different valve sizes can be positioned within a given D^*. It is possible to implant different valve sizes in the same patient also by resorting the 'oversizing' practice (Blanke *et al.*, 2014) or by positioning the valve in 'supra–annular' position (Sung *et al.*, 2008). This implies that the present results should be interpreted as a general trend of the system rather then as a performance assessment of a specific device; for the latter a one–to–one geometric replica of the device and the exact knowledge of its positioning are necessary.

3.3.1 The reference case: Healthy ventricle and natural valve

The reference case consists of a left ventricle with an ejection fraction of 60% and a natural mitral valve with the anterior leaflet, the one closer to the aortic channel, slightly longer than the posterior (figure 3.2a).

Following the curve of figure 3.12 we see that at the beginning of the diastole the E–wave strengthen, the flow rate through the mitral orifice increases and the valve opens, thus producing an intense jet. Owing to the asymmetry of the leaflets, the jet is initially directed towards the ventricle wall where it starts sweeping the endocardium (figure 3.13a). Once the peak of the flow rate is reached, the valve leaflets open wider and the jet points vertically downward reaching the ventricle apex (figure 3.13b) and generating a strong recirculation (figure 3.13c). The process repeats during the A–wave with a new injection of momentum that further strengthens the large–scale vortex. This recirculation lasts for a large fraction of the cycle (about 50%) and it is very beneficial for the hemodynamics since it constantly sweeps the endocardium and prevents the formation of stagnant flow regions (Fortini *et al.*, 2013). When the systole starts, the flow leaves the ventricle both from the aortic and mitral channel. The orientation of the mitral leaflets, however, is such to prevent a continuous regurgitation and the low pressure, induced by the incipient back flow accelerating between the leaflets, seals them (figure 3.13e). Beyond this point the flow can leave the ventricle only through the aortic channel, the ventricle shrinks and the outflow decreases until the initial volume is recovered and the ventricle is ready for a new cardiac cycle.

Similar features, in a somehow more quantitative way, can be deduced from figures 3.14 and 3.15 showing phase averaged mean and rms vertical velocity profiles along the horizontal sections $z = 1$ and $z = 2$ in the symmetry plane $y = 0$. In the sake of conciseness the profiles are shown only for the peaks of the E– and A–waves when the strongest mitral jets are produced; for these instants of the cycle the position of the sections is evidenced by dashed lines in figures 3.13b,d. Figures 3.14–3.15 show the same quantities also for a biological trileaflet and a mechanical bileaflet prosthetic valve in order to compare the different flow behaviours: each case will be discussed in each dedicated section.

The natural valve, at the peak of the E–wave (figures 3.14a and 3.15a), produces a smooth and regular jet that induces a ventricle flow recirculation evidenced by the negative velocity region to the left of the jet. Despite the relatively large excursions of the valve leaflets, discussed later in this section, the mitral jet remains compact in space thus providing, within a fixed momentum (in turn depending on the ejection fraction) the highest penetration capability and the smallest pressure losses among all the valves (see also the discussion

in Section 3.4): both features are beneficial to prevent flow stagnation inside the ventricle.

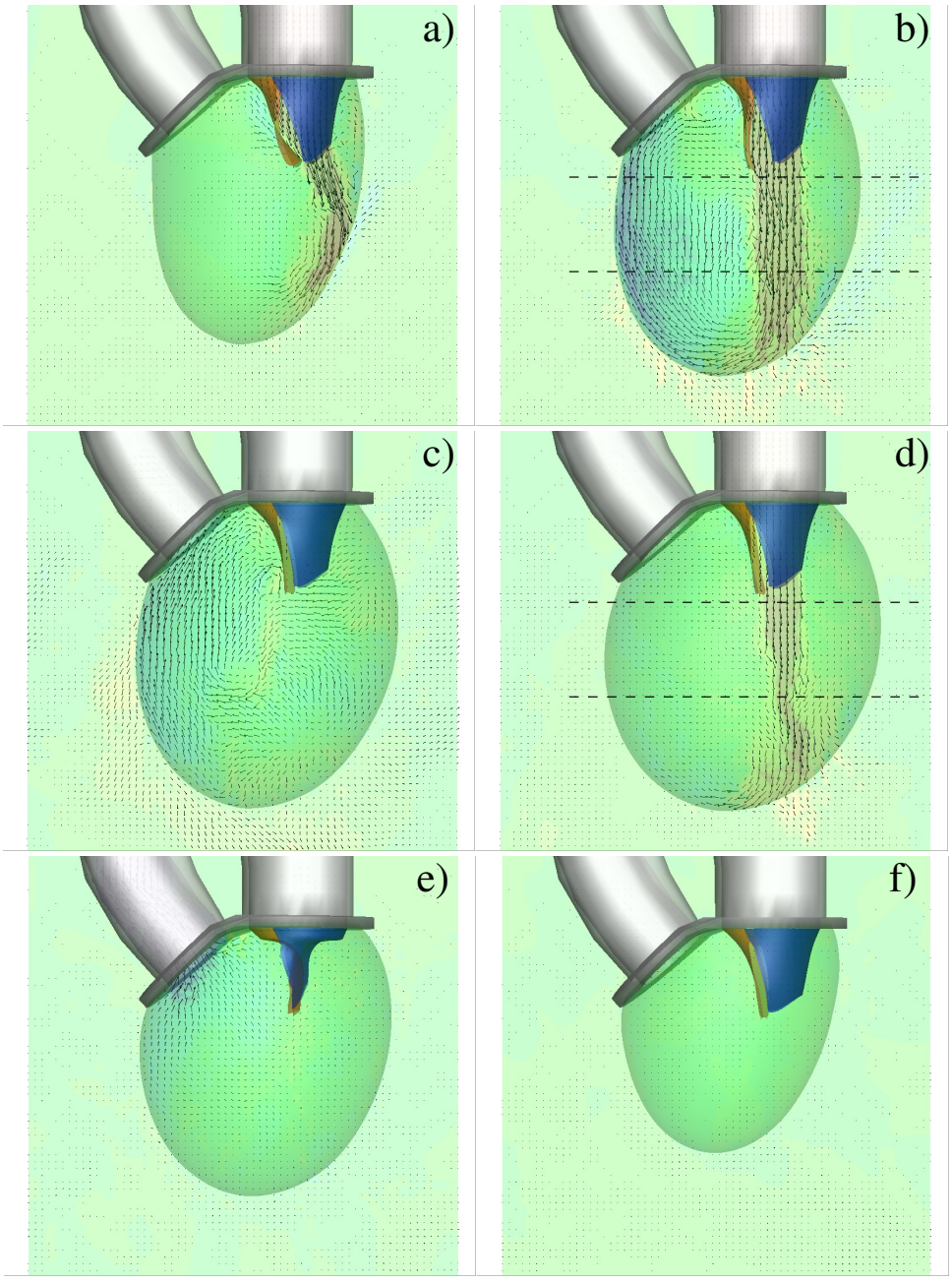

Figure 3.13: Snapshots of the velocity vector in the x–z symmetry plane and contours of vertical velocity (range is $-2 \leq v_z \leq 2$ from blue to red) at $EF = 60\%$ with natural mitral valve. The different instants of the cardiac cycle are indicated in figure 3.12 by the symbol $\circ$ a) early E–wave, b) peak of the E–wave, c) diastole, d) peak of the A–wave, e) peak systole, f) end of systole. The ---- lines of panels b) and d) evidence the sections at $z = 1$ and $z = 2$ over which the velocity profiles in figures 3.14 and 3.15 are reported.

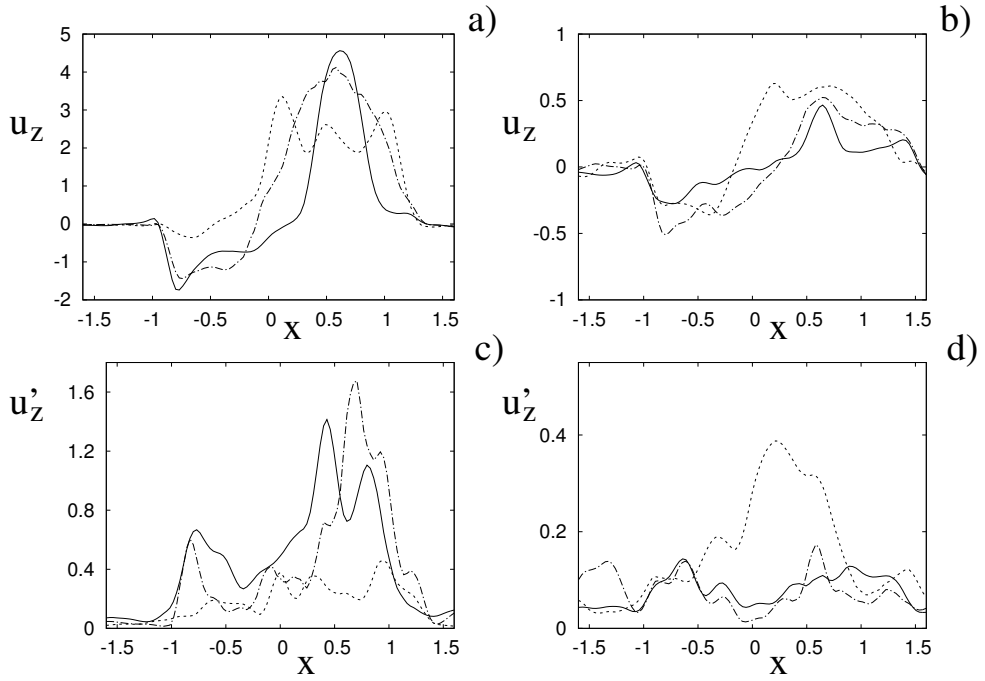

Figure 3.14: Phase–averaged vertical z velocity profiles at the section $z = 1$: top panels for mean velocity, bottom panels for rms fluctuations. a) and c) peak of the E–wave, b) and d) peak of the A–wave. —— natural valve, - - - - mechanical valve, —·— biological valve.

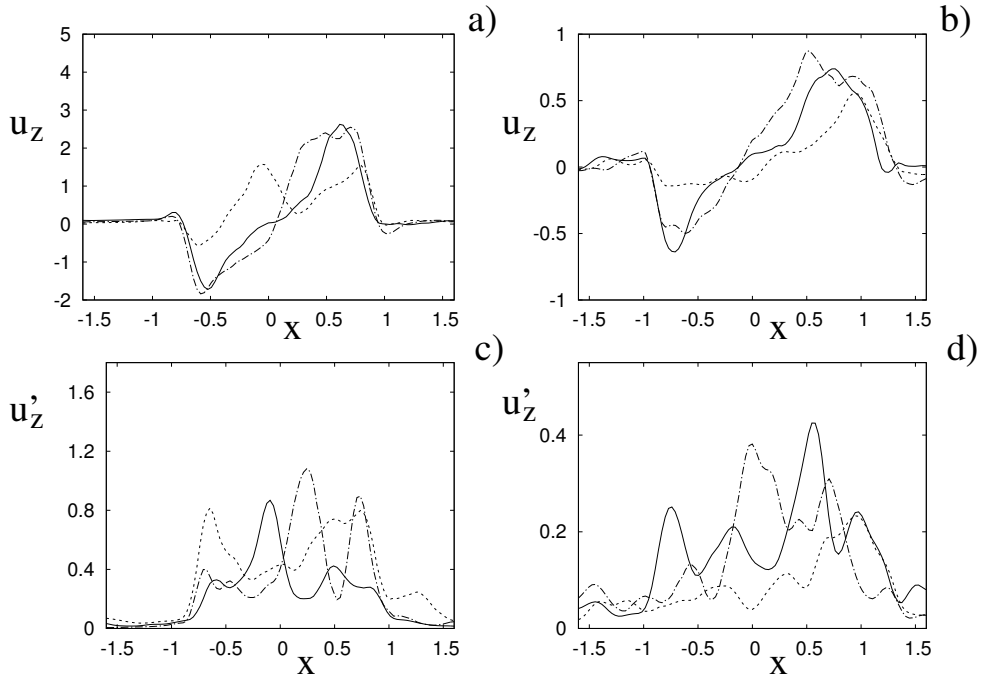

Figure 3.15: The same as figure 3.14, but for the section $z = 2$.

This strong jet assures the presence of a persistent vortex during most of the heart cycle that constantly sweeps the ventricle surface and avoids the formation of regions of stagnant fluid, a phenomenon referred to as blood stasis. The latter is a particularly undesired condition since the blood in dead recirculations tends to coagulate and produce clots that, once again in the systemic circulation, can obstruct vital arteries and cause infarction or stroke (Cordero *et al.*, 2015).

In order to monitor the motion of the fluid during the cycle we report in figure 3.16a the time evolution of the velocity magnitude sampled at the apex probe shown in figure 3.3a. It can be noted the peak of the velocity at $t = 0.2$, caused by the maximum of the E–wave ($t \approx 0.16$), followed by the velocity decay during the diastasis ($0.3 \leq t \leq 0.5$); even at the end of the diastasis, however, the fluid is not at rest and the occurrence of the A–wave ($t \approx 0.56$) produces a new velocity peak although with reduced magnitude. Similar information is obtained by the kinetic energy of the fluid within the ventricle shown in figure 3.16b; here we note also that during the systole ($0.65 \leq t \leq 1$) the energy of the fluid increases again owing to the intense velocities in the region around the aortic channel. The sudden energy drop at $t \approx 0.78$ indicates the fast closure of the mitral valve that prevents the blood regurgitation toward the left atrium and allows the flow only through the aorta.

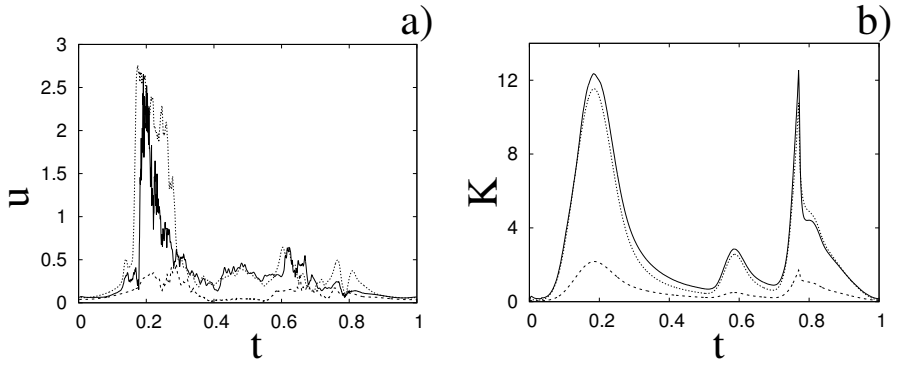

Figure 3.16: a) Phase–averaged evolution of the velocity magnitude u at the apex probe with the natural mitral valve. b) Kinetic energy of the flow inside the ventricle. —— $EF = 60\%$, - - - - $EF = 40\%$, ····· $EF = 60\%$ with non–Newtonian fluid model.

The plot of figure 3.17 confirms the above argument by showing the strong leaflets retraction during the closing phase that occurs approximately at 78% of every cycle. It is also evident a strong cycle–to–cycle variability caused by the transitional nature of the flow; the latter is characterized by explosive bursts of turbulence, produced during the flow decelerations, separated by turbulence decay phases during the quiescent parts of the cycle (Fortini *et al.*, 2015). Another important feature evidenced by figure 3.17a is the very different mobility of the anterior and posterior leaflets; although both of them are made by the same tissue and have the same thickness, their different curvature and shape make the posterior leaflet stiffer and this is evidenced by the reduced vertical excursion, $\overline{Z}_l$, during the cycle with respect to the anterior one. Similar dynamics is observed also for the mean horizontal coordinate,

$\overline{X}_l$, not shown here in the sake of shortness. It is worth mentioning that this effect is independent of the chordae tendineae that, in the real heart, connect the edges of both leaflets to the myocardium through the papillary muscles. The chordae, in fact, only act at the end of the closing phase by exerting a tension that prevents the leaflets from everting into the mitral channel. The kinematic effect of the chordae tendineae has been modelled in our numerical simulation by freezing the vertical dynamics of the leaflets during the systole once the valve had closed.

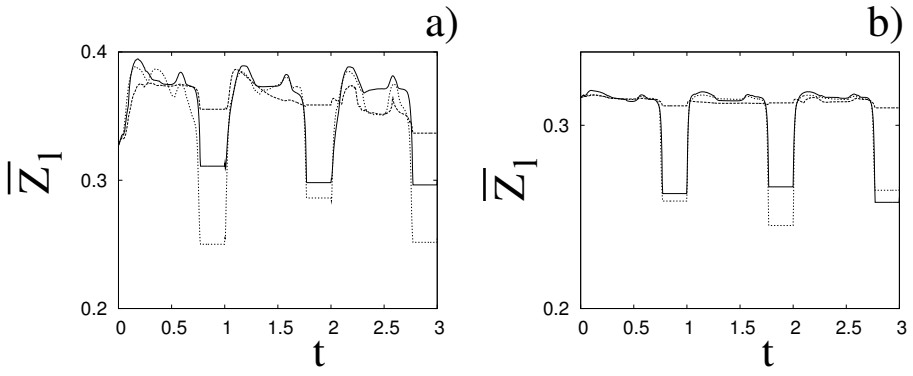

Figure 3.17: Time evolution of the mean vertical coordinate $\overline{Z}_l$ of the a) anterior and b) posterior leaflets of the natural mitral valve. —— $EF = 60\%$, ---- $EF = 40\%$, ····· $EF = 60\%$ with non–Newtonian fluid model.

3.3.2 Healthy ventricle with natural valve and non–Newtonian fluid model

In this section we briefly report the results obtained for the same configuration as in the previous section ($EF = 60\%$ and natural valve) but for a non–Newtonian shear–thinning fluid. The comparison between the two cases is shown in figures 3.16–3.18 confirming that either globally and locally the differences are minor and very likely due to cycle–to–cycle variation or marginal time convergence of the local phase averaged statistics. In particular, the dynamics of the valve leaflets as well as the kinetic energy of the flow hardly show any difference while the mitral jet at the peak of the E–wave (figure 3.18a) looks slightly more compact than its Newtonian counterpart (figure 3.13b). The effect on the velocity magnitude at the apex probe is to maintain the peak value for a slightly longer time (figure 3.16a) even if the features of ventricular flow have very similar cycle evolution. A similar conclusion had been drawn in De Vita *et al.* (2016) for the flow through a mechanical bileaflet valve in a realistic aortic root. In that study the large–scale dynamics of the flow was found independent of the fluid model and the only feature that showed appreciable sensitivity was the hemolysis which turned out about 15% larger for the shear–thinning fluid than for the Newtonian one.

3.3.3 Healthy ventricle with stiffened or stenotic natural valve

As mentioned previously the membrane mechanical properties in the numerical simulations have been taken from the companion experiment in which a

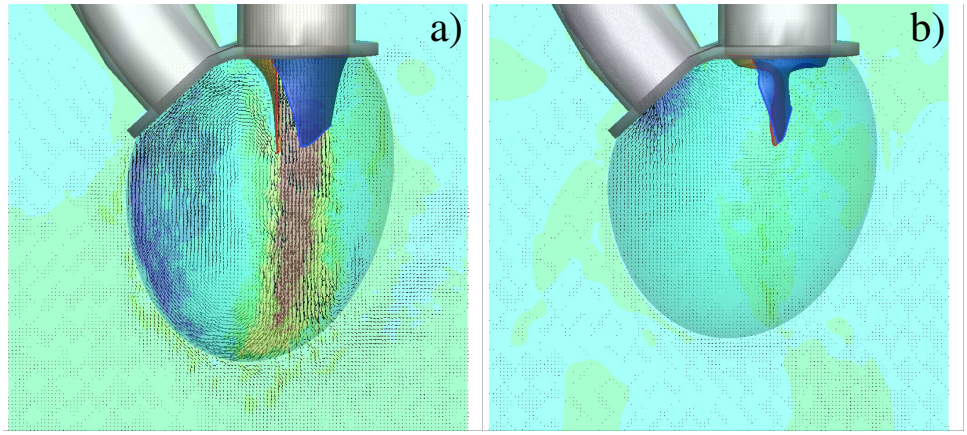

Figure 3.18: The same as figure 3.13, but for non–Newtonian fluid model. a) Peak of the E–wave, b) early systole.

two component transparent silicon rubber was used to realize the ventricles and the natural valve. This material is linear elastic and isotropic, therefore totally different from the biological tissues which are normally hyperelastic and anisotropic (usually orthotropic depending on the orientation of the fibers). We believe that this difference is not very important for the ventricle since its volume evolution in time depends on a flow rate that is prescribed as a boundary condition and therefore independent from the structure dynamics, (figure 3.4). The situation is more delicate for the valves, whose dynamics is determined by the fluid structure interaction and, thus on the mechanical properties of the leaflets. Since in this chapter we aim at studying the flow changes induced by different mitral valves it is crucial to separate the effects of the deliberately modified geometry from those of the less known material properties. In order to asses the effects of the latter factor, we have run an additional simulation identical to the reference case of section 3.3.1 but with the mitral leaflets doubled thickness (from 0.1 to 0.2) and considering a higher elastic constant for the material (three times larger than the one of the reference case).

The results of figures 3.19–3.21, show that the solution is relatively insensitive of the specific leaflet properties, at least for the range of parameters explored here. This is true either for the global integral quantities, like the flow kinetic energy (figure 3.21c), and for the more local ones as the lateral displacement of the leaflets (figure 3.21d) and the pressure drop across the valve (figures 3.20ab). Although at a first glance this insensitivity might seem surprising it can be easily estimated that for a rectangular ($a \times b$) membrane of thickness s of density approximately equal to that of the ambient fluid, the added mass overcomes the membrane mass for $s < 4b/10$. On the other hand the external pressure moments exceed the internal structural reaction for $s < (5\Delta p a^2 b/E)^{1/3}$ with, Δp the maximum pressure difference in the fluid. Since in these membranes it results $s \ll a, b$ and the elastic constant at most one order of magnitude bigger than the pressure difference ($E \approx 2 \times 10^5$ Pa and $\Delta p \approx 2 \times 10^4$ Pa for the human mitral valve) the above conditions are always satisfied and the leaflet dynamics is determined mainly by the external

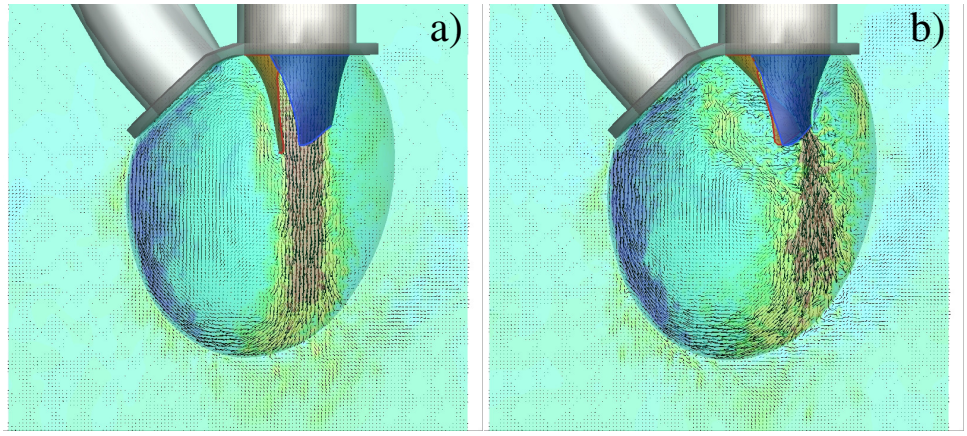

Figure 3.19: The same as figure 3.13 at the peak of the E–wave for a) stiffened natural valve, b) stenotic natural valve.

loads.

A further quantitative measure of the little sensitivity of the solution to the specific properties of the valve leaflets is given by the mean transvalvular pressure drop that is $\Delta p \simeq 0.49$ and $\simeq 0.45$ (3.66 and 3.38 mmHg), respectively, for the reference and 'stiffened' mitral valve.

A more relevant parameter for this problem is instead how the valve leaflets are connected (constrained) to the structure. In the physiological condition the deformable leaflets are attached to a fibrous ring that behaves very much like a rigid frame. For the prosthetic valves the conditions can vary since there are models (stented) in which the leaflets are connected to a rigid or flexible frame while in other models (stentless) there is no frame and the leaflets are stitched directly to the fibrous ring. Other pathologic constrains may be present in the natural and prosthetic valves because of calcification that occurs at the junction between the leaflets and the fibrous ring: the progressive growth of the calcium deposit reduces the section available to the flow and limits the mobility of the leaflets (valve stenosis). For all the simulations performed in this chapter we have constrained the deformable leaflets to the frame (the red structure in figure 3.3) only by keeping fixed in time the position of the triangle edges crossing the rigid plate. Therefore regardless of the specific valve type in all the cases the lumen of the mitral channel is the same. However, in order to test the effects of more constrained leaflets or the occurrence of stenotic conditions, we have simulated also a case in which all the triangle nodes whose vertical coordinate is smaller than $z = 0.5$ are kept fixed in time; this condition prevents the motion of the portion of the leaflets within the dashed line of figure 3.20c and reduces the area of the mitral channel by 72%. Figures 3.19–3.21 now indicate that relevant changes are produced in the flow and the limited mobility of the leaflets is accompanied by a higher velocity of the mitral jet (given the imposed constant flow rate) that in turn produces higher kinetic energy of the ventricular flow. The faster jet however is not as efficient as the physiological one since, while its velocity is ≈ 3.4 times bigger than the reference case, the apex peak velocity is only $\approx 16\%$ more intense (figure 3.21d). On the other hand the stenosis generates a larger pressure drop

across the valve (figure 3.20c) whose mean value is $\Delta p \simeq 3.05$ (22.93 mmHg) much larger than $\Delta p \approx 0.5$ obtained for the above valves with full mobility. It should be pointed out however that while the described trends are general the specific values depend heavily on the detailed geometry of the obstruction (calcification) that, not only can reduce the available area but also induce asymmetries.

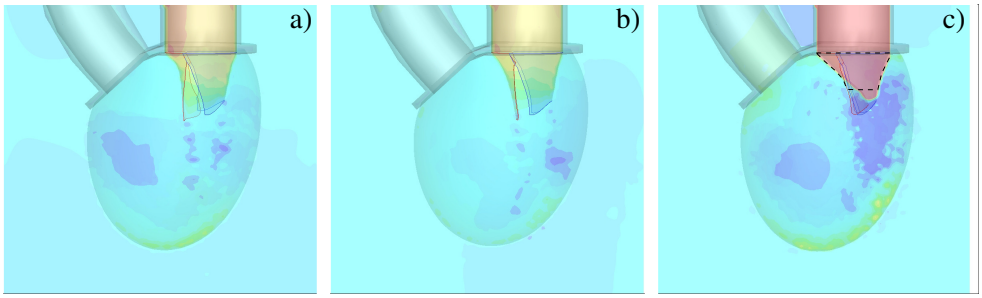

Figure 3.20: Instantaneous snapshots of the pressure field at the peak of the E–wave ($EF = 60\%$) for a) physiological natural valve, b) stiffened natural valve, c) stenotic natural valve. The ---- line highlights the region where the valve is forced to maintain a fixed geometry in order to mimic the stenosis. The colors range from dark blue $p_{min} = -1.5$ to purple $p_{Max} = 2$.

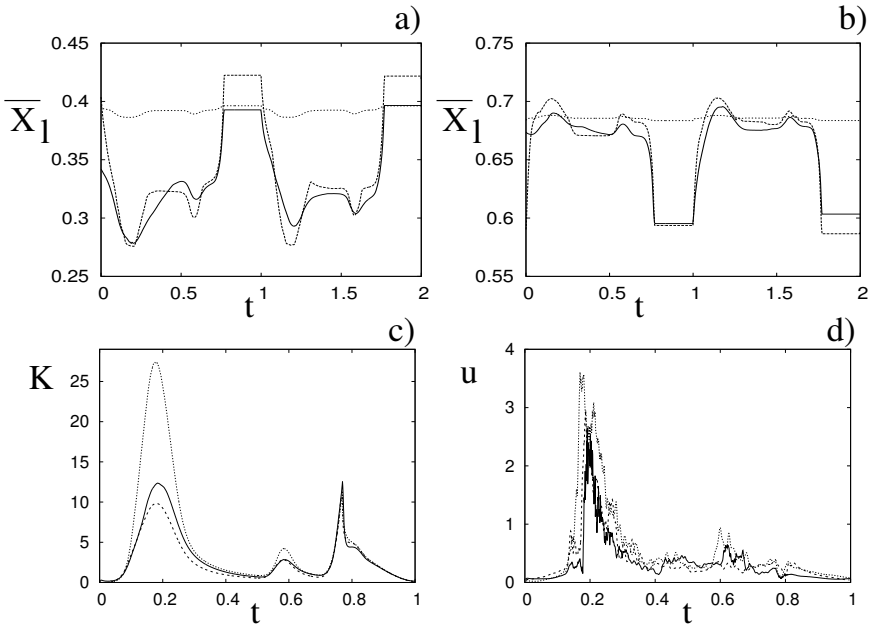

Figure 3.21: a) Instantaneous mean horizontal coordinate $\overline{X}_l$ of the anterior mitral valve leaflet. b) the same of a) but for the posterior mitral valve leaflet. c) Phase–averaged kinetic energy of the flow inside the left ventricle. d) Phase–averaged velocity magnitude at the apex probe. —— physiologic natural valve, ---- stiffened valve, —·— stenotic valve.

3.3.4 Pathological ventricle with natural valve

In order to isolate the effect of a reduced ejection fraction, here we consider the same case as in the previous section except for the ejection fraction that is reduced to the lower end of the pathological value $EF = 40\%$. The comparison between the panels of figure 3.13 and 3.22 immediately evidences the weakened flow within the ventricle that, however, can still reach the apex of the ventricle and 'wash' that region. A similar picture emerges from the apex probe in figure 3.16a and the kinetic energy in figure 3.16b. An important difference with the case at $EF = 60\%$ is that now the recirculation dies out during the diastasis therefore the A–wave, rather than reinforcing the vortex previously generated by the E–wave, produces a new weaker recirculation that is expelled from the ventricle during the systole. The time evolution of the leaflets motion of figure 3.17b is consistent with the described picture: Again the posterior leaflet moves less than the anterior one and there is some cycle–to–cycle variability. In this case, however, the displacements are quite small and the reduced momentum of the mitral jet is not enough to open completely the valve. From a comparison of figures 3.13e and 3.22b we note that, in this case, the weak contraction of the ventricle during systole can still close the valve although does not squeeze the leaflets one against the other; this could cause some valve leakage known as mitral insufficiency. Phase averaged profiles, as in figures 3.14 and 3.15, not reported here for the sake of shortness, show a similar behaviour as in the case of section 3.3.1 although with reduced amplitude for the mean and rms velocity profiles. The smaller level of fluctuations is consistent with the fact that an ejection fraction of $EF = 40\%$ yields a peak Reynolds number about half of the case at $EF = 60\%$ (see the curves of figure 3.12).

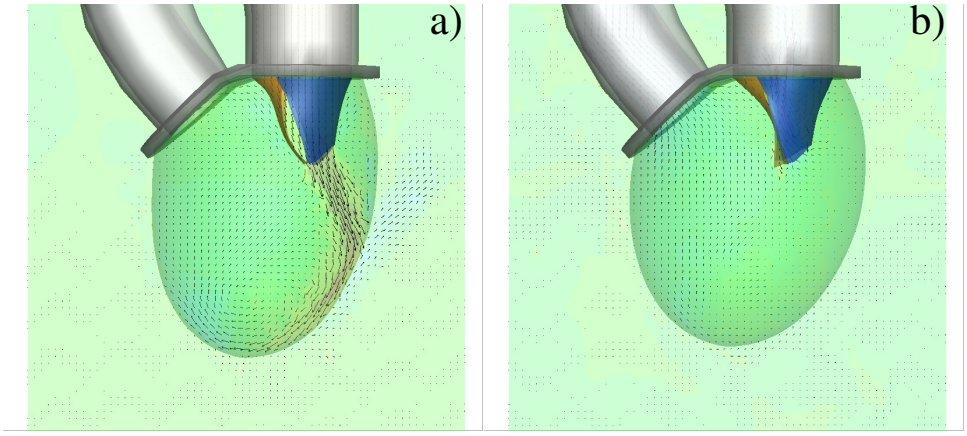

Figure 3.22: The same as figure 3.13, but for $EF = 40\%$. a) Early E–wave, b) early systole.

3.3.5 Ventricle with mechanical bileaflet valve

As mentioned above, if the mitral valve has to be replaced, and the life expectation of the patient goes beyond fifteen years, the most common choice is a mechanical bileaflet valve as that in figure 3.2c. In this device, two semilunar

rigid leaflets are hinged to a circular frame and they passively rotate about the pivots as a result of the pressure and viscous forces exerted by the fluid on their surfaces. The kinematics of this prosthesis is such that the leaflets always occupy part of the mitral channel, even when the valve is fully open (figure 3.23c) and this is a crucial difference with respect to the natural and biological prosthetic valves in which the flow pushes the flexible leaflets towards channel boundary leaving the orifice completely clear (figure 3.23ab). The problem is further exacerbated by the necessity of giving the rigid leaflets in fully open position an inclination ($\approx 10^o$) in order for the incipient reverse flow to generate a moment closing the valve. This implies that the leaflets do not behave as thin flat plates but rather as obstacles shedding unstable shear layers and vortices in the flow that are responsible for the poor hemodynamics of the prosthesis. In a few words, the increased turbulence level downstream of the valve produces augmented mechanical stresses on the corpuscular part of the blood that cause red blood cells damage (hemolysis) and platelets activation Grigioni *et al.* (2001). These phenomena both concur to the formation of clots whose aggregation is countered by a lifelong anticoagulant therapy that, in turn, increases the risks of bleeding and hemorrhagic events.

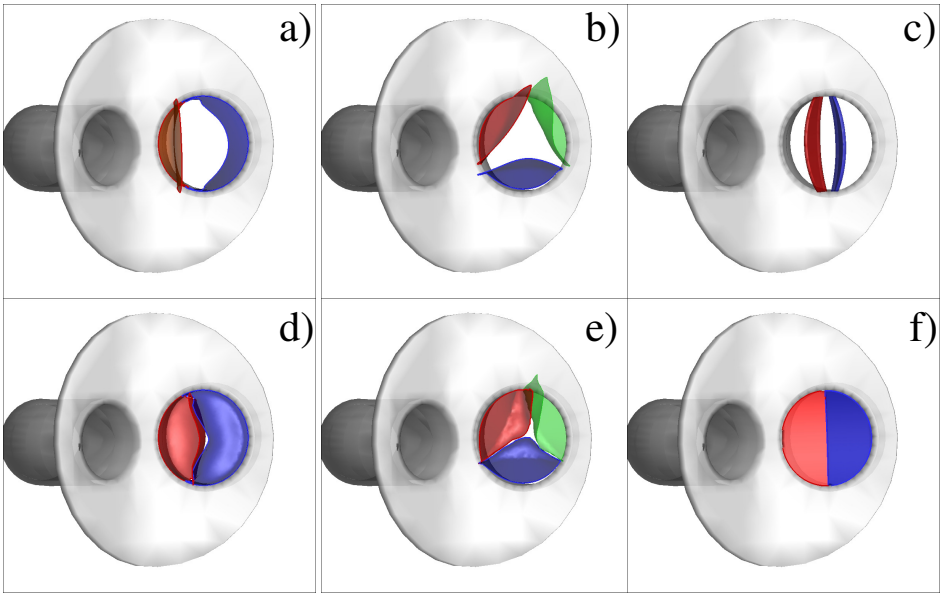

Figure 3.23: Snapshots of the three different mitral valves: natural (a,d), biological (b,e) and mechanical (c,f), respectively in fully open and closed position in the case of a healthy left ventricle ($EF = 60\%$).

The altered flow dynamics is shown in figure 3.24 for an ejection fraction $EF = 60\%$ which models a healthy ventricle. It is evident that the mitral jet during the E–wave is much less regular and smooth with respect to the analogous field in figure 3.13a and the augmented turbulence enhances the lateral spreading of the jet to the detriment of its vertical penetration. A more quantitative view of this phenomenon can be obtained by the time evolution of the phase averaged velocity magnitude at the apex probe (figure 3.25a) showing a strongly fluctuating signal with a mean component that is much weaker than in the case of the natural valve (figure 3.16a). Another important

difference is that the mitral jet, that has lost part of its momentum into small–scale fluctuations, generates a weak large–scale recirculation whose intensity hardly lasts up to the A–wave as confirmed by the velocity signal during the diastasis that decreases continuously. The A–wave, on the other hand, undergoes a dynamics similar to that previously described but now, being weaker, produces an effect at the ventricle apex of the same order as the underlying velocity fluctuations. This picture is confirmed by the evolution of the kinetic energy of the flow within the ventricle evidencing a less energetic flow throughout the cycle (figure 3.25b).

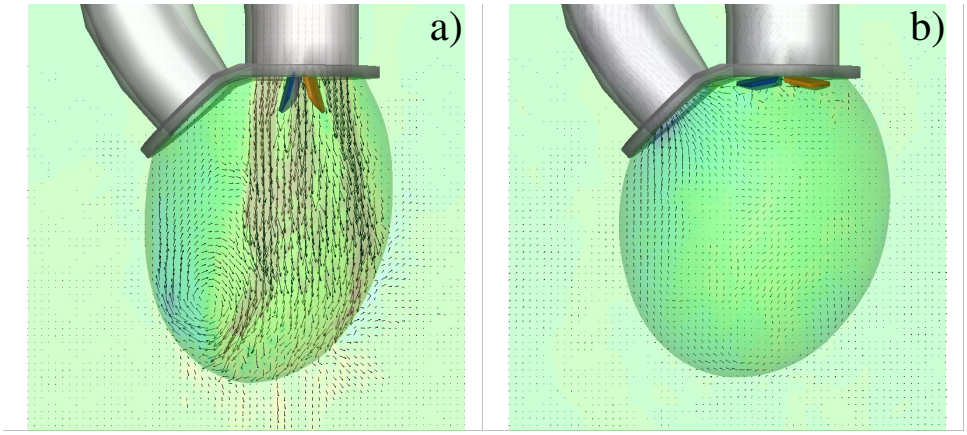

Figure 3.24: The same as figure 3.13, but for a mechanical valve at $EF = 60\%$. a) Early E–wave, b) early systole.

The velocity profiles of figures 3.14 and 3.15 reinforce the analysis made above. In particular the panel 3.14a evidences the typical 3–jet configuration of the mean flow whose peak velocity is the smallest among all valves. Being the flow rate identical for all the valves (and imposed as a boundary condition) a smaller peak velocity suggests a larger lateral spreading and a weaker ventricular recirculation as indicated by the small amplitude negative velocity. The same dynamics is observed farther downstream in figures 3.15ac ($z = 2$) with the mean flow still maintaining more than one peak and the vanishing ventricular recirculation.

The dynamics during the A–wave (figure 3.14bd and 3.15bd) partly benefits from the fact that, differently from the natural and biological valves, the leaflets remain in fully open position during all the diastole and no inflow momentum is used for the valve opening. Nevertheless, the disturbances of the leaflets on the ventricular flow are still visible from the highest level of fluctuations in figure 3.14d and the weakest mean and rms flow shown in figure 3.15bd. The fact that even within a healthy ventricle ($EF = 60\%$) the flow with the mechanical valve has a reduced intensity at the section $z = 2$ suggests that an impaired ventricle with a mechanical valve could generate regions with stagnant flow; that indeed this is the case will be shown in the remaining part of this section.

It is worth mentioning that the above described dynamics occurs for a prescribed inflow, as that in figure 3.12, which is exactly the same as that used for the cases with the natural mitral valve. This implies that the energy

and momentum injected into the system is the same in both cases and the differences must be ascribed only to the different interaction between incoming flow and structure dynamics.

As anticipated above the scenario considerably worsens if the pumping efficiency of the ventricle drops below the healthy range; in this chapter we have considered the case at $EF = 40\%$ whose results are reported in figures 3.25–3.26. The dynamics is similar to the case at $EF = 60\%$ with the fundamental difference that now the reduced momentum of the inflow, combined with the perturbations introduced by the valve leaflets, further decreases the penetration capability of the mitral jet and produces a stagnant fluid region at the ventricle apex. This is quantitatively confirmed by the velocity sampled at the apex probe that shows negligible values over the whole cycle and by the time evolution of the flow kinetic energy (figure 3.25b) that results at least twice lower than the analogous flow with the natural valve.

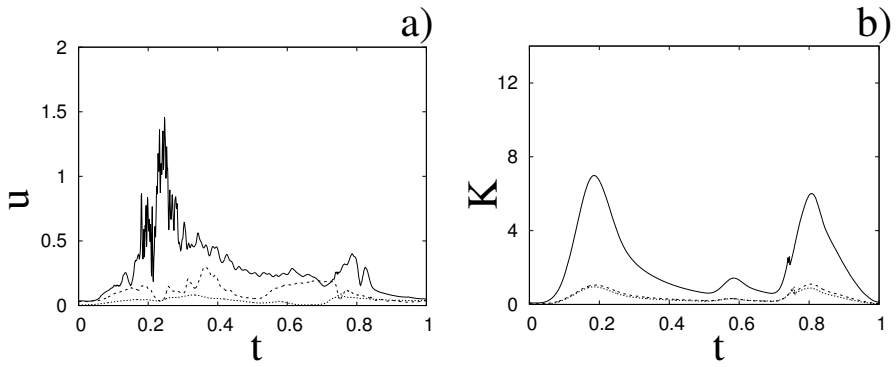

Figure 3.25: The same as figure 3.16, but for a mechanical valve.—— $EF = 60\%$, ---- $EF = 40\%$, ····· $EF = 40\%$ with the valve in the anti–anatomical position.

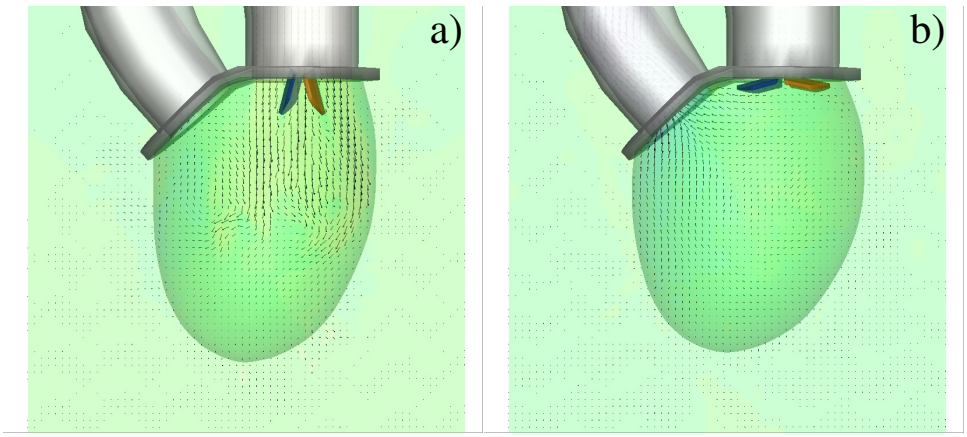

Figure 3.26: The same as figure 3.13, but for a mechanical valve at $EF = 40\%$. a) Early E–wave, b) early systole.

In some studies (Choi *et al.*, 2014; Machler *et al.*, 2004) it has been investigated whether the implantation of the mechanical valve in anti–anatomical position, i.e. with the leaflets orthogonal with respect to the natural configu-

ration, could give a better hemodynamics with respect to the latter implantation. The issue has been the subject of many discussions among cardiac surgeons and a clear evidence of some advantage has not emerged. Here we have simulated the anti–anatomical configuration in the case of a ventricle at $EF = 40\%$, the critical case that would benefit most from some improvements. We have found that, consistently with the available literature, no appreciable differences have been observed with respect to the standard case. In fact, apart from the obvious different orientation of the jet leaving the valve (figure 3.27), the velocity magnitude at the apex probe is even smaller than the case of anatomical implantation as observed in Choi *et al.* (2014). Anyway, the flow velocity at the apex remains negligible during all the cycle and also the kinetic energy of the ventricular flow is essentially the same as the original case (figure 3.25).

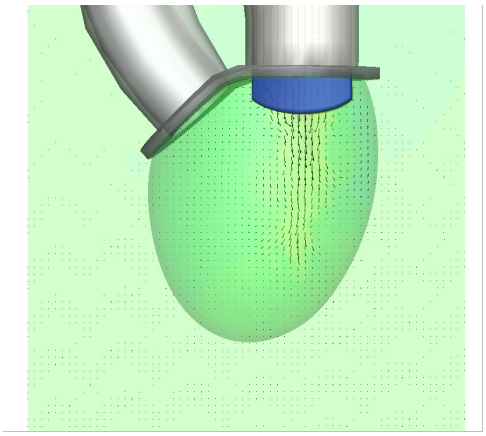

Figure 3.27: The same as figure 3.26, but for a mechanical valve at $EF = 40\%$ in anti–anatomical position at the early E–wave.

3.3.6 Ventricle with biological valve

The same simulations as in the previous sections are repeated here with a trileaflet biological prosthesis, as that of figure 3.2b, in mitral position. As shown in figure 3.23 when this valve opens the lumen remains free from obstacles and the mitral jet enters the ventricle as a compact vertical stream capable of penetrating the ventricle volume up to the apex. However, since the three leaflets are all identical they open in a nearly symmetric way and the emerging jet always points vertically downward during all the E–wave injection (figure 3.28a). This is a relevant difference with the natural valve that, owing to the leaflets asymmetry, initially produces a jet pointing laterally to the sidewall (figure 3.24a) and only at the peak of the E–wave is bent vertically (figure 3.24b) and directed towards the ventricle apex. It is worth pointing out that, during the implantation, a surgeon could, in principle, position the trileaflet prosthesis with some tilting angle so to obtain an inclined mitral jet. The latter, however, would always point in the same direction during all the diastole and a variable pitch jet, as emerging from a natural valve, could not be obtained.

The fact that, with a trileaflet valve, the mitral jet constantly points to-

wards the ventricle apex is further confirmed by looking at figures 3.16a and 3.30a; although in both cases the inflow is the same ($EF = 60\%$ of figure 3.12) the peak velocity at the apex probe occurs earlier for the prosthetic than for the natural valve. Comparing these results with those of the mechanical valve (figure 3.25a) it is evident that the hemodynamic performance of the biological valve is better than the mechanical prosthesis although both of them produce strong enough recirculations to avoid ventricular hemostasis during the diastolic part of the cycle.

For the present trileaflet valve the velocity profiles of figures 3.14 and 3.15 show flow features that are comparable to those of the natural valve and with a definitely better hemodynamics than that of the mechanical prosthesis. More in detail, the present valve can produce relatively compact mitral jets capable of penetrating the ventricle up to the apex and generating the beneficial recirculation (figures 3.14a and 3.15ab) that prevents the hemostasis. This suggests that the biological valve might operate adequately even in an impaired ventricle with a reduced ejection fraction that generates low momentum mitral jets.

In fact, when a mitral biological valve is combined with a pathologic ventricle ($EF = 40\%$), the superiority with respect to the mechanical valve is amplified and, differently from the latter, the former still operates correctly with a hemodynamics similar to the natural one.

More in detail as shown in figure 3.29a, although the mitral jet has a reduced momentum, the ventricular recirculation still extends up to the apex and the peak of the E–wave has a distinct signature in the probe signal (figure 3.30a).

The time histories of the ventricular kinetic energy (figures 3.16b, 3.25b and 3.30b) tell a similar story with the biological prosthesis that outperforms the mechanical one for all ejection fractions. It is however well known that the better hemodynamics of the biological valves comes at the price of a durability of the order of $15 - 20$ years to be compared with a lifetime of 80 years of the mechanical devices (Hoffmann *et al.*, 2008). This is a crucial decision factor in the valve replacement when a choice has to be made between the two classes of artificial valves; presently the common practice is to implant biological valves in those patients whose expectation of life is less than $15 - 20$ years and mechanical valves in all other cases (apart from particular conditions like diseases or women pregnancy). In this study we have however shown that the pumping efficiency of the ventricle could be another relevant factor that should be taken into account when selecting the valve to be implanted.

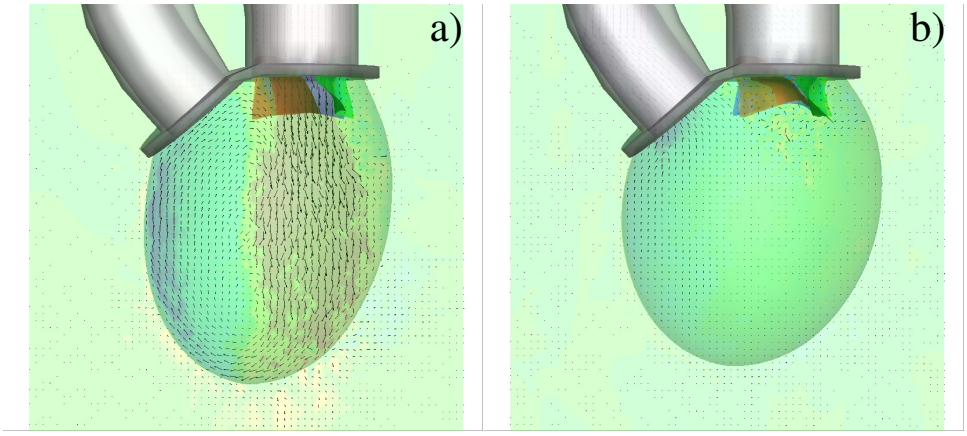

Figure 3.28: The same as figure 3.24, but for a biological valve at $EF = 60\%$. a) Early E–wave, b) early systole.

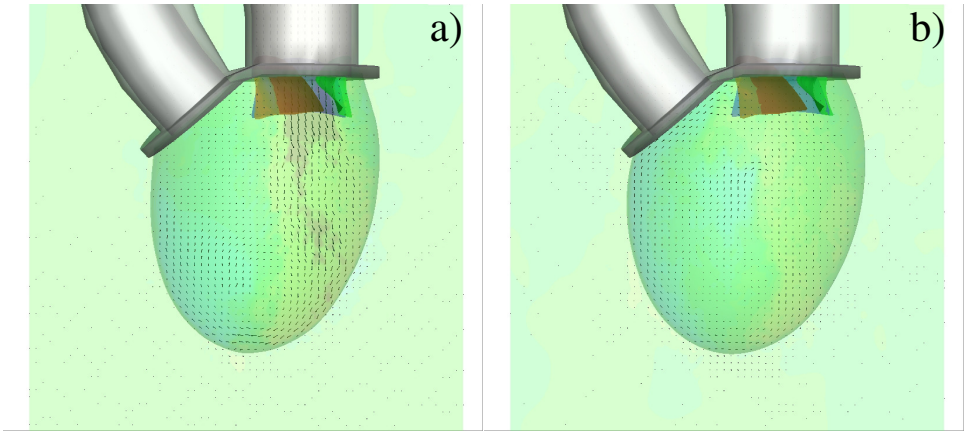

Figure 3.29: The same as figure 3.28, but for $EF = 40\%$. a) Early E–wave, b) early systole.

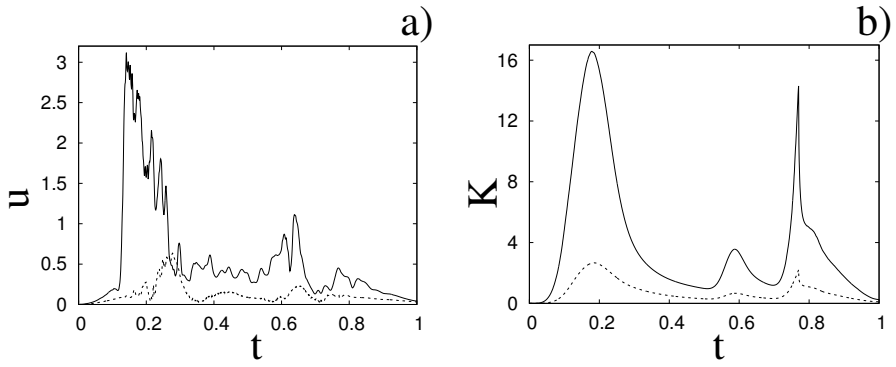

Figure 3.30: The same as figure 3.16, but for a biological valve. —— $EF = 60\%$, ---- $EF = 40\%$.

3.4 Discussion

The main finding of this investigation is summarized by the snapshots of figure 3.31 showing the streamtraces in the x–z symmetry plane at the end of the diastole ($t = 0.69$) when the ventricle attains its maximum volume. All three flows are computed for an ejection fraction of 40%, an inflow curve as that of figure 3.12 and for otherwise identical conditions except for the type of mitral valve. It is evident that the large–scale recirculation is strongly determined by the specific valve model and in the case of a mechanical valve the large–scale vortex does not reach the ventricle apex. It is worth mentioning that for all the three cases of figure 3.31 the E–wave propagation index (EPI) described in Harfi *et al.* (2017) would be nearly identical since it is given by the ratio of the propagation length of the mitral jet L_{MJ} and the vertical length of the ventricle at the maximum expansion L_{LV}. As shown by Harfi *et al.* (2017), for all practical purposes, L_{MJ} can be estimated in a echocardiography through the velocity time integral $VTI = \int_0^{T_E} V_M(t)\mathrm{d}t$ being T_E the duration of the early wave and V_M the jet velocity at the mitral leaflets. Since all the inflows are identical and L_{LV} depends on the ejection fraction, in all cases the E–wave propagation index is the same and indeed a direct calculation for $EF = 40\%$ yields $EPI = 1.24,\ 1.35,\ 1.31$, respectively, for the natural, biological and mechanical valve.

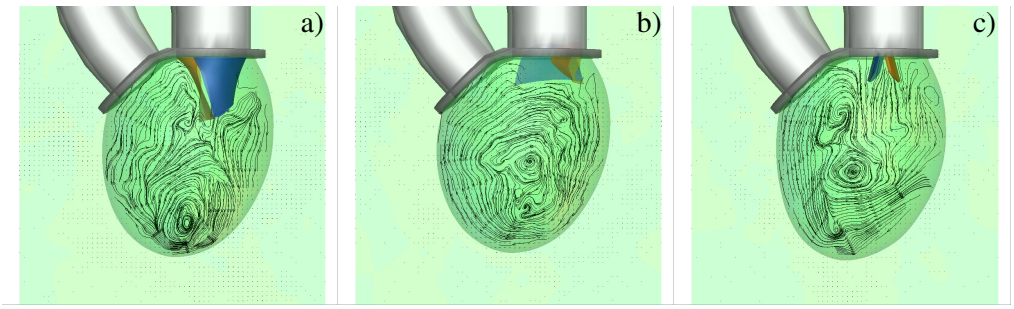

Figure 3.31: Streamtraces in the x–z symmetry plane at the end of the diastole ($t = 0.69$) for $EF = 40\%$. a) natural valve, b) biological valve, c) mechanical valve.

This is fully consistent with the time evolution of the vertical velocity component (as obtained from the mitral probes of figure 3.3b) at the center of the jet and halfway of the mitral leaflets $z = 0.75$ (figure 3.32a) showing a very similar evolution for all mitral valves. On the other hand, the same quantity further downstream at $z = 1.5$ (figure 3.32b) indicates a different evolution of the mitral jet with the natural valve that produces the largest velocity and the mechanical valve the smallest. This is due to the disturbances induced by the valve on the flow whose momentum tends to cascade to the small scales because of turbulence. The velocity profiles of figure 3.32b might be more relevant for the clinical diagnosis than those of figure 3.32a since in the echocardiography the mitral flow Doppler is not measured at the base of the valve but rather at a downstream section. The EPI computed with these profiles yields $EPI =$ 1.52, 1.38 and 0.69, respectively, for the natural, biological and mechanical valve thus confirming all the discussion of the previous sections.

As an aside, we note that during the systole, the intensity of the back

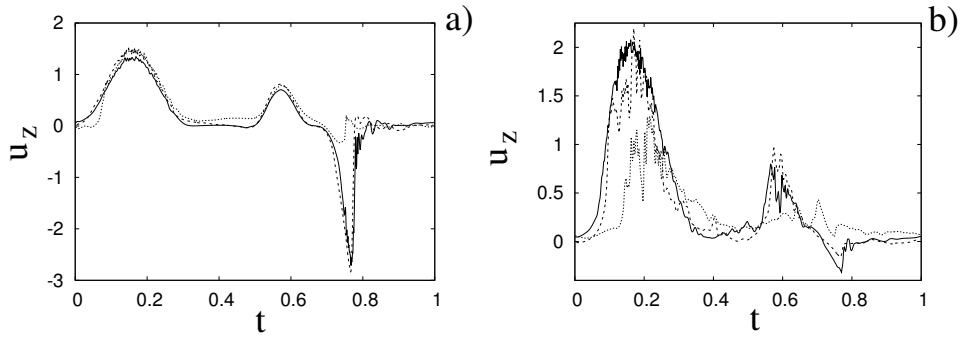

Figure 3.32: Phase–averaged vertical velocity at the a) 'mitral' probe $z = 0.75$ and b) 'tip' probe $z = 1.5$ for $EF = 40\%$. —— natural valve, - - - - biological valve, ····· mechanical valve.

flow in figure 3.32a is different for the various valves and it is the smallest for the mechanical prosthesis; the reason is that as the flow accelerates in the retrograde direction, the semilunar leaflets quickly rotate about the hinges and seal the mitral orifice without deformations. In contrast, the natural and biological valves, even after having sealed the leaflets, keep deforming and retract towards the mitral channel thus inducing a local backward velocity that, however, does not produce a valve leakage: this phenomenon is referred to as 'false regurgitation'.

To provide further evidence of the above described dynamics also the wash–out curves for a passive scalar have been computed. Taking as initial condition a ventricle filled with a passive scalar at concentration $q = 1$ the flows have been evolved injecting 'clean' fluid ($q = 0$) from the mitral inflow and the time evolution of the total scalar $Q = \int_{V_v} q \mathrm{d}V$, ($V_v$ being the time–dependent ventricle volume) has been computed for all the cases. The convection/diffusion equation for the scalar concentration has been integrated using the velocities from the previous numerical simulation and the Schmidt number of the scalar has been set to $Sc = 1$.

In figures 3.33ab instantaneous snapshots of q are reported for a representative case showing the incoming jet of the clean fluid that eventually partially mixes with the q–concentrated fluid inside the ventricle. During the diastole (figure 3.33a), although the mean q concentration decreases, owing to the dilution with the clean fluid, the total scalar remains constant. In contrast, during the systole (figure 3.33b), the mixed fluid is ejected from the ventricle through the aortic channel and Q decreases in time. Figure 3.33cd shows that this behaviour is common to all the mitral valves although the amount of wash–out is different. This is especially true for the cases at $EF = 40\%$ for which it is confirmed that the mechanical valve produces the minimum ventricle wash–out.

The fact that each valve perturbs the mitral jet by a different amount is confirmed also from figure 3.34 showing the histograms of the peak pressure drops across the valve during the cycle which occurs at the peak of the E–wave; it is evident that the mechanical valve in the fully open position produces the biggest pressure losses that are responsible for the velocity drop observed in figure 3.32 and for the disgregation of the initially coherent jet into small incoherent flow scales.

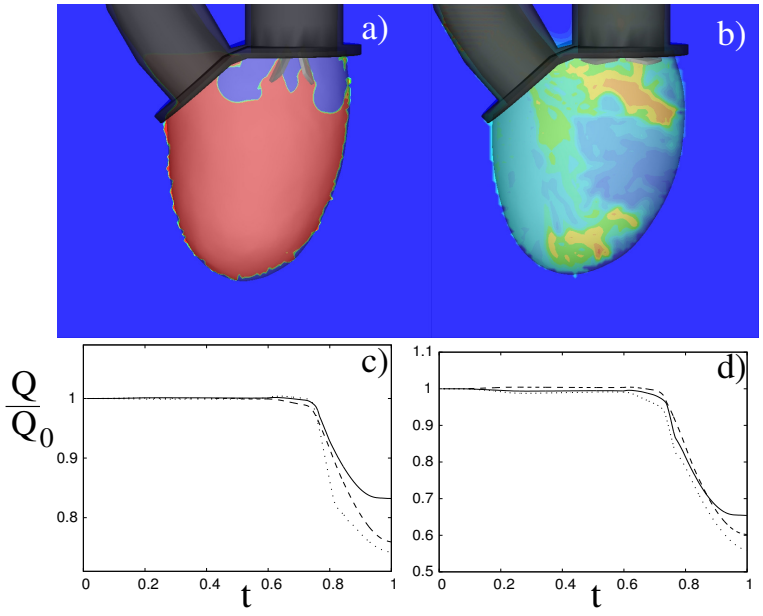

Figure 3.33: (Top) Instantaneous distribution in the x–z symmetry plane of a passive scalar q for a bileaflet mechanical valve and $EF = 40\%$: a) beginning of the diastole ($t = 0.1$); b) end of diastole ($t = 0.9$). The colour contours of the passive scalar range from $q = 0$ (blue) to $q = 1$ (red). (Bottom) Time evolution of the normalized total scalar Q/Q_0 during a heartbeat (Q_0 is the initial value of Q), —— bileaflet mechanical valve, ---- biological valve, ····· native valve; c) $EF = 40\%$, d) $EF = 60\%$.

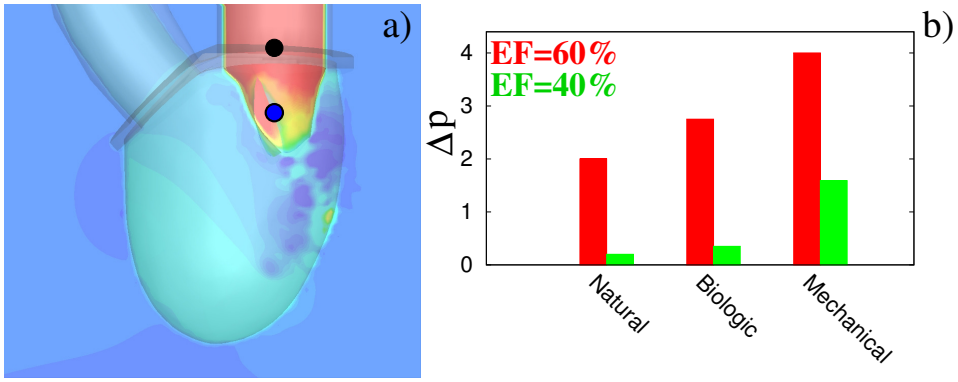

Figure 3.34: a) Snapshots of the pressure field values of left ventricle with natural mitral valve at early diastole. The two bullets indicate the representative positions among which the pressure drop is evaluated. b) Maxima pressure drops at the peak systole for the natural, biological and mechanical mitral valves in both cases of $EF = 60\%$ and $EF = 40\%$.

A popular quantity used to characterize the valve performance is the effective orifice area (EOA) defined as the ratio of the peak flow rate to the maximum velocity (averaged over the jet section) that can be interpreted as the minimum cross section of the mitral jet that is smaller than the geometrical area because of vena–contracta effects. Depending on the flow kinematics the EOA can be quite different from the lumen of the mitral orifice; for example,

in the present case the lumen area is $A = \pi/4 = 0.785$ (4.52 cm^2) while for the effective orifice area it results $EOA = 0.628$, 0.445 and 0.550 (respectively 3.62, 2.56 and 3.17 cm^2) for the natural, biological and mechanical valves. The fact that mechanical valves have EOA generally larger than biological prosthesis is consistent with the clinical literature (Pibarot & Dumesnil, 2012); this quantity, however, takes into account only the geometry of the valve and the continuity equation therefore it might not be adequate to characterize the dynamic performance of the valves. In fact, the transvalvular pressure drop (referred to as 'pressure gradient' within the clinical community) shown in figure 3.34b, does not correlate with the EOA since its value depends also on the balance of momentum in the flow.

A final global view of the above described dynamics is given in figure 3.35 showing the time integrated circulation of the 'core' ventricular flow. More in detail, in the symmetry x–z plane we have (arbitrarily) isolated the square region S ($-0.5 \leq x \leq 0.5$ and $1.0 \leq z \leq 2.0$), far enough from the boundaries, and integrated the out–of–plane vorticity component ω_y to obtain a circulation $\Gamma_y(t) = \int_S \omega_y \mathrm{d}S$. This quantity has been time–averaged over the cycle through $\Omega(t) = (\int_0^t \Gamma_y(\tau)\mathrm{d}\tau)/t$ and the result is reported for the three mitral valves at $EF = 40\%$ in figure 3.35. The strongest mean flow rotation is produced by the natural valve while the biological prosthesis misses the initial peak. The reason for this difference is that the jet from the natural valve initially points to the right towards the sidewall (figure 3.22a) and induces a clockwise rotation in all the ventricle. The mitral jet from the biological valve, in contrast, points always vertically downward (figure 3.29a) thus inducing counterclockwise vorticity to its right region and weakening the overall circulation. Again the mechanical valve is the one inducing the weakest large–scale rotation of the core flow because of the flow transition to small scales that cross diffuse one into another and prevent the formation of a strong coherent vortex.

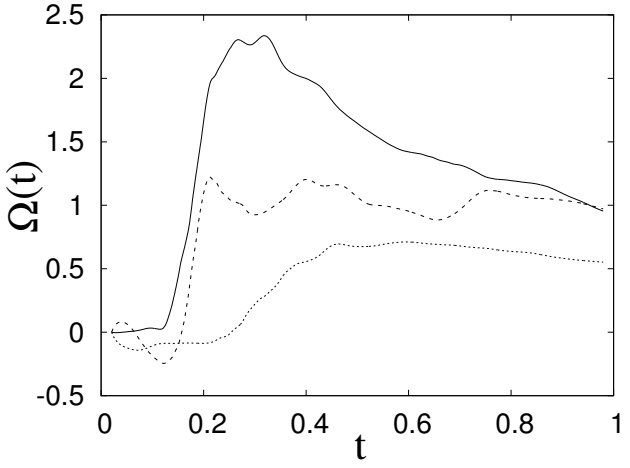

Figure 3.35: Time evolution of the averaged circulation $\Omega(t)$ of the ventricular flow at $EF = 40\%$. —— natural valve, - - - - biological valve, ····· mechanical valve.

Before concluding this discussion we wish to comment on how the present findings relate to the clinical literature according to which the free event survival curves of mitral valve replacement in a five–year follow–up (but also ten–

or fifteen–years) are very similar for mechanical bileaflet and bio–prosthetic valves despite the superior hemodynamics of the latter claimed in this study. In the paper by Chikwe *et al.* (2015) a cohort of 3433 patients, all in the age $50 - 69$ and with mitral disease requiring valve replacement, showed that indeed 'No survival difference was observed between use of mechanical prosthetic and bioprosthetic mitral valves'. However the break–up of the data evidenced that the causes of deaths are very different for the two classes of prostheses with 'the incidences of stroke and bleeding events ... significantly higher in those who received mechanical prosthetic mitral valves' and 'the incidence of reoperation ... lower in the mechanical prosthesis group' (Chikwe *et al.*, 2015). More quantitatively, for the bileaflets implantation strokes account for 15% of the lethal events while for bioprosthetic valves they are only 6.8%, thus evidencing a higher propensity of the mechanical valves to generate clots. The other relevant difference is the bleedings that are 14.9% for mechanical valves and 9% for the biological ones; the increased bleeding is a consequence of the lifelong anticoagulant therapy that the recipients of mechanical valves have to take to prevent clot formation. On the other hand, bioprosthetic valves degenerate more rapidly especially in non elderly patients and the deaths caused by reoperation amount to 5% for the mechanical and 11% for the bioprosthetic valves. It appears that these numbers miraculously balance so that the overall fatality rate is roughly the same (Chikwe *et al.*, 2015).

Analogous figures come from Hammermeister *et al.* (2000) that analysed two groups of 88 and 93 patients who had the mitral valve replaced, respectively, with a mechanical or a biological prosthesis. The follow–up at 15–years showed that the fatality rate from any cause was almost the same (81% vs 79%) although the single causes were different with 53% of bleeding events for the mechanical valve and 31% for the bioprosthesis, but 25% vs 50% for reoperation and 5% vs 40% for primary valve failure.

Unfortunately, the analyses of Chikwe *et al.* (2015) and Hammermeister *et al.* (2000) do not distinguish the patients for different ejection fractions while Qiu *et al.* (2010), who consider mechanical and biological mitral valve replacements in dysfunctional ventricles, do not separate the deaths occurred with different valve models. Nevertheless, the statistics reported in Cen *et al.* (2001) confirm that for physiological ejections fractions (in the range of 50%) both the mechanical and the prosthetic valves perform adequately while De Bacco *et al.* (2009) report that in mechanical mitral valve replacement, a low ejection fraction ventricle is one of the most negative prognostic factors: both results are consistent with our findings.

As a relevant point we note that the acceptable performance of the mechanical valves comes at the cost of a heavy anti–coagulant therapy that has to be carefully tuned in order to prevent clot formation but, at the same time, to avoid hemorrhagic events: in developed countries, even under a close surveillance, it induces a 2% fatality event rate per year (Cannegieter *et al.*, 1994, 1995). At present, this therapy aims at maintaining the INR ('international normalized ratio' an indicator of the blood coagulation time) above a given threshold whose value depends on the presence of a mechanical valve prosthesis but it does not change for different ejection fractions of the left ventricle; it might be possible that if the anti–coagulant dose were tailored also to the ventricle efficiency some of its negative side effects could be mitigated.

3.5 Closing remarks

In this chapter the flow in the left ventricle with different types of mitral valves has been analysed, by high–fidelity numerical simulations, for different pumping efficiencies of the system. The reference case, obtained for a natural valve, has evidenced the highly synergistic nature of the flow with an interplay between the ventricle and valve dynamics that prevents the formation of stagnant flow regions considered as a negative predictive factor for infarction and stroke.

The results have shown that for a healthy ventricle with an ejection fraction $EF = 60\%$ either the biological and the mechanical prostheses perform adequately even if the former has a better hemodynamics than the latter. Both of them produce a mitral jet that is strong enough to penetrate up to the apex of the ventricle and generates a beneficial large–scale recirculation that 'washes' the inner ventricular wall (endocardium). In contrast, in a ventricle with a reduced efficiency ($EF = 40\%$), which is a possible condition when a valve replacement is required, the mitral jet has a reduced momentum and the perturbations induced by the prostheses can decrease the penetration of the jet below the required level. This is the case of the mechanical bileaflet valve that produces the highest transvalvular pressure drop and causes the transition of the coherent mitral jet to incoherent small scales; this prevents the jet from reaching the ventricle apex and causes blood stagnation (Badas *et al.*, 2016).

This observation could be a novel factor to be taken into account when deciding whether a biological or a mechanical prosthetic valve should be used for a mitral valve replacement. Presently, the best practice, gives the highest weight to the balance between the life expectation and the prosthesis durability: since a biological valve is expected to perform for $15 - 20$ years, patients with a life expectation beyond $15 - 20$ years receive a mechanical valve. The results of the present investigation suggest that among the decision factors also the efficiency of the ventricle should be considered since a mechanical valve implanted in a ventricle with ejection fractions of 40% or below, might lead to flow stasis and the formation of dangerous clots.

These findings are fully consistent with the clinical literature that, even if report nearly identical fatality rates for the follow–up of mitral replacement with mechanical valves or bioprostheses (Chikwe *et al.*, 2015; Hammermeister *et al.*, 2000), indicate that the causes of deaths are very different. In addition Cen *et al.* (2001) confirms that for ejections fractions in the range of 50%, both the mechanical and the prosthetic valves perform adequately while De Bacco *et al.* (2009) states that an impaired ventricle is among the most negative prognostic factors for a mitral valve replacement with a mechanical prosthesis.

As mentioned at the beginning of Section 3.3 the shapes of the natural and prosthetic mitral valves have been reconstructed from anatomical sketches or available designs and it has been assumed that all of them could fit into a $D^* = 24$ mm diameter annulus. While these geometries reproduce the main features of generic devices, in reality there is plenty of different models each one with its own peculiarities and with different hemodynamic performance. The picture is further complicated by the possibility for the surgeons to implant the prostheses in slightly different positions or to accommodate, within the

same annulus, valves of different sizes. This suggests that the present results should be intended as guidelines for the behaviour of different classes of valves and not as the performance assessment of a specific device.

Before concluding this chapter we wish to make a few comments about the similarities and the differences between our computational model and the real ventricular flow. As mentioned in section 3.2.1 the development of the numerical model was initially guided by the companion experimental apparatus of which the former is a digital replica. The final result is a quite complex numerical tool that can cope with a full FSI with rigid and deformable bodies within realistic geometries and flow parameters. Despite the considerable computational effort, still there are relevant differences between the present model for the left ventricle and the intended real of the human heart that should be taken into account when applying the results to clinical cases.

For example, the model has a fixed mitral plane and a movable apex while real left ventricles have a movable mitral plane and (nearly) fixed apex. Since the (base–apex) pressure gradient is proportional to the time derivative of the velocity, this might introduce differences between the present model and the real flow. However if, by a linear extrapolation, we assume that the apex displacement is twice that of the centroid, from figures 3.7cd we can estimate a maximum non dimensional apex acceleration of $a_A \approx 8$ (a maximum displacement of 0.54 unit lengths in 1/4 of the cycle period). On the other hand, from figure 3.12, using a sine to approximate the inflow curve during the first 1/3 of the cycle, it can be computed a non dimensional acceleration for the fluid at the inflow of $a_F = U_{peak} 2\pi/(0.3T) \approx 25$. The fluid acceleration at the ventricle base must be 4–5 times bigger since that the flow further accelerates through the mitral valve and the peak velocities in the ventricle are 4–5 times bigger than at the inflow (see figure 3.14). According to these estimates, the apex acceleration is at lest one order of magnitude smaller than the accelerations induced in the fluid by the imposed inflow/outflow and we expect the effect of the former to be minor.

Another difference is that in our model the mitral annulus is planar and rigid while in the real heart the shape changes during the heartbeat and it assumes a saddle shape. According to different papers in the literature, (Levine *et al.*, 1987; Mahmood *et al.*, 2010; Salgo *et al.*, 2002; Votta *et al.*, 2008), the mitral annulus is flat during diastole and it becomes saddle shaped only during systole. In particular Salgo *et al.* (2002); Votta *et al.* (2008) found that the annulus non–planarity affects mainly the mobility of the posterior leaflet and facilitates the valve closure. In this paper however we are mainly concerned with the diastolic phase when the mitral valve opens and the ventricular flow is generated, therefore we expect this feature not to affect significantly our conclusions. A similar argument can be used to assess the effects of the different dimensions of the anterior and posterior leaflets of a native mitral valve: in our model the vertical length of the leaflets is comparable while in the real heart the posterior is about 1/3 shorter.

Moreover also the smooth surface for the left ventricle modelled here is far from the inner structure of the endocardium that is characterized by irregular grooves (trabeculae). As shown by Vedula *et al.* (2016) the flow within the trabeculae is closely linked to the active contraction of the myocardium but this feature affects mainly the near wall region and much less the large–scale

features that we have analysed here.

Another difference is the presence, in the natural valve, of the chordae tendineae, flexible and inextensible 'filaments', that link the leaflets tips to the myocardium through the papillary muscles; these structures tense during the systole and prevent the leaflets from everting into the atrium. In this chapter only their kinematic effects on the leaflets dynamics of the natural valve has been simulated using 'numerical artifices' without considering their physical interaction with the ventricular flow. The physical inclusion of chordae tendineae in the 3D geometry of the natural mitral valve and the investigation of their effects on the flow dynamics and ventricle deformation will be the focus of the next chapter.

Chapter 4

Effects of chordae tendineae on the flow in the left heart ventricle

Based on: Valentina Meschini, Marco D. de Tullio & Roberto Verzicco, 'Effects of chordae tendineae on the flow in the left heart ventricle', submitted to *European Journal of Physics E* special issue on *Fluids and Structures: Interaction and Modeling.*

4.1 Introduction

The left side of the heart, and especially the left ventricle, is the most exposed to cardiac pathologies, like valve failure or myocardium impairing, because of the high pressure differences it has to withstand (120–160 mmHg or 1.6–2.1 $\times$ 10^4 Pa). Accordingly, among all hearth diseases, those of the left side account for most of the direct and morbidity related deaths.

Thanks to advances in surgical techniques and diagnostic tools the prognoses for these disorders have considerably improved over the last decades and research has given a fundamental contribution. Unfortunately the ageing of the population and a growing percentage of it accessing advanced medical care is projecting the health care costs to worrisome figures and innovative tools are needed to revert this unfavourable tendency, Mittal *et al.* (2016). The combination of computational engineering and medical research has the potential to help in this direction by producing new technologies and improving treatment outcomes without concurrently increasing the costs.

Motivated by the above arguments, in this chapter we present the results of a computational model geared towards complex cardiovascular flows. Here we consider the left ventricle with the mitral valve and both structures are two–way coupled with the fluid that is evolved in physiological conditions.

In the heart, the left ventricle has two valves: the aortic that assures the correct direction of ventricular flow to the aorta and the mitral that guides the atrial flow into the ventricle. The former regulates the outflow while the latter is responsible for the inflow therefore it has the strongest influence on the intra–ventricular flow, Sacks *et al.* (2009); for this reason in this chapter we focus on the analysis of the mitral valve features and their effects on the flow dynamics.

The mitral valve, of which a cartoon is given in figure 4.1, is the most complex of the four heart valves. It is a bi-leaflet valve located between the left atrium and the left ventricle. The two leaflets are asymmetric, with the anterior one longer than the posterior, and they extend into the left ventricle where they are fastened to the papillary muscles by the chordae tendineae, Millington S. *et al.* (1998). These consist of a complex web of chords that depart from the leaflets edge and prevent their prolapse into the atrium during systole. The functioning of the chordae is assisted by the papillary muscles, protrusions of the myocardium, which relax during isovolumic systole and contract during the ejection (diastolic) phase.

Different computational models for the mitral valve have been proposed in the literature. The first finite element three–dimensional model to simulate both healthy and impaired mitral valves was developed by Kunzelman *et al.* (1993, 1997*a*,*b*); then Prot *et al.* (2009) used that model to study also the effect of the shape of the valve annulus on the flow dynamics. The main limitation of those works was the assumption of a symmetric valve whose real shape is crucial to determine the correct intra–ventricular flow. This topic was partially addressed by Lim *et al.* (2005) who analyzed how the annulus profile and papillary muscles evolve in time, using *in vivo* data from sheep. Nevertheless this paper, as well as the other ones, was mainly concerned with structural mechanics and missed the fluid–structure interaction (FSI) that characterizes the valve dynamics. Einstein *et al.* (2005*a*, 2003); Kunzelman *et al.* (2007)

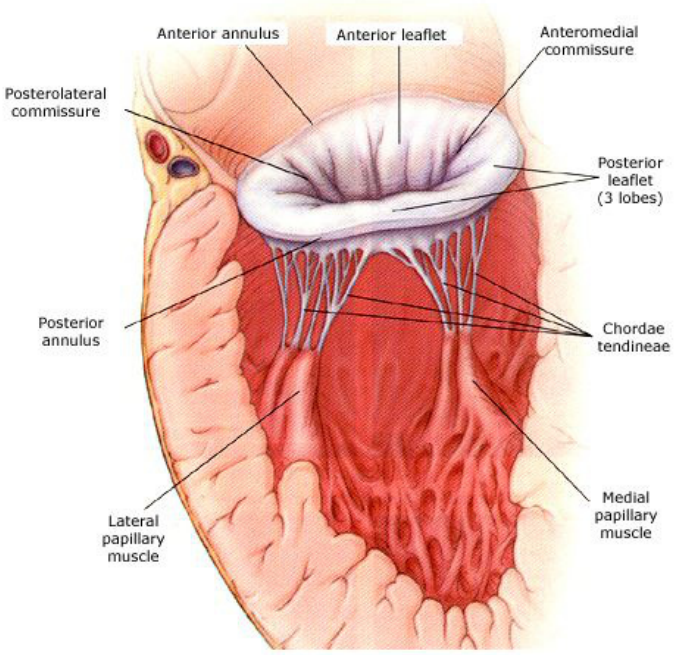

Figure 4.1: Sketch of the mitral valve apparatus (adapted from http://www.oncologynurseadvisor.com/anesthesiology/mitral-valve-replacement/article/580656/).

presented a realistic model with the three–dimensional coupling of fluid and structure although the valve was considered isolated and its interaction with the ventricle was neglected. Watton *et al.* (2008) analyzed the dynamics of a chorded mitral valve by assigning the kinematics of the chordal–ventricle attachment points according to data obtained by high–resolution magnetic resonance image: in this case the chordae/ventricle interaction was properly accounted but the intra–ventricular flow could not be described.

Recently, in Meschini *et al.* (2017), it has been underlined that the mitral valve interacts directly with the ventricle through the flow and the leaflet dynamics results from the interaction with the surrounding flow that, in turn, is determined by the leaflet configuration. In order to cope with this coupled dynamics a full FSI computational tool has been developed and the flow has been analyzed considering either the native mitral valve and the deformable left ventricle. The mitral valve in Meschini *et al.* (2017), however, was modeled without chordae tendineae and their functionalities were replaced by ad hoc kinematic conditions; these mainly prevented the leaflets from everting into the mitral channel during systole and the flow from regurgitating into the 'atrium'.

In this chapter we aim at moving one step further towards an uncompromised model of the ventricle by adding physical chordae tendineae to the mitral valve and removing the ad hoc conditions; this allows the model to be self–consistent and to fully capture the synergistic mechanisms within the ventricle.

The chapter is structured as follows. In the next section the model and the flow parameters are described and its experimental validation is given.

In section 4.3 the results for the chorded mitral valve are presented and the comparison with the non chorded one is shown. The closing remarks and the perspectives for future studies are given in the final section.

4.2 The model

4.2.1 The numerical method

The computational model consists of two–way coupled flow and structure solvers, wand it is essentially that described by de Tullio & Pascazio (2016), Spandan *et al.* (2017) and Meschini *et al.* (2017). For a detailed description of the specific algorithms and the convergence checks of the model we refer to the previous references; here we report only the features of the building blocks.

The motion of the blood is described by the Navier-Stokes equations which, in non dimensional form, read:

$$\begin{aligned} &\frac{\partial \mathbf{u}}{\partial t} + \mathbf{u} \cdot \nabla \mathbf{u} = -\nabla p + \frac{1}{Re} \nabla^2 \mathbf{u} + \mathbf{f}, \\ &\nabla \cdot \mathbf{u} = 0. \end{aligned} \tag{4.1}$$

Here $\mathbf{u}$ is the velocity, p the pressure and Re the Reynolds number, later defined. $\mathbf{f}$ is a specific body force, related to the immersed boundary (IB) technique, used to impose the correct boundary condition at the immersed surface. Even though the blood is a non-Newtonian fluid, here it is assumed Newtonian since it is known that its non–Newtonian nature is relevant only in vessels of diameter smaller than 15–20 red blood cell diameters ($\sim$ 80–100 μm), Siginer *et al.* (1999). In Meschini *et al.* (2017) it has anyway been shown by direct numerical simulations that the above statement applies also to the present flow.

An interaction potential approach is employed to capture the structure dynamics. This idea was introduced in Tanaka *et al.* (2012) and then applied to several phenomena in de Tullio & Pascazio (2016), Spandan *et al.* (2017) and Meschini *et al.* (2017). The structures are discretized by a triangular mesh and the vertices are connected by elastic springs, the total mass of the body is distributed on the vertices of the triangles. When this complex network deforms it stores potential energy (given by elastic, bending, area and volume energy) whose gradient yields the internal forces. These, summed to the local hydrodynamic loads and other external forces (like gravity), are used to evolve the dynamics of each network node according to the second Newton's law. By successive integrations, from the acceleration, the velocity and then the position of the nodes is computed and the structure configuration updated.

The effect of complex–geometry bodies on the flow is imposed by the IB method and two different techniques are employed. For the moving and deformable structures we rely on the moving–least–squares approach of Vanella & Balaras (2009) since, despite the computational cost, it yields smooth hydrodynamic loads at the interface thus resulting in accurate structure deformations. In contrast, for rigid structures the computationally inexpensive direct–forcing approach of Fadlun *et al.* (2000) is adopted.

The core of the model is the fluid–structure interaction algorithm and a loose coupling approach, in which the fluid is solved first and the hydrodynamic

loads are used to evolve the structure, has been selected after extensive convergence checks. The procedure can be outlined as follows: starting from the flow and structure at the time t^n, the flow is advanced at the time ($t^{n+1} = t^n + \Delta t$). The new flow field is used to compute the hydrodynamic loads by the pressure and the wall shear stresses. Interpolating the loads between t^n and t^{n+1} the structure can be evolved up to t^{n+1} with a time substep $\Delta t_s = \Delta t/S$, where S is the number of substeps.

4.2.2 The set–up

As already evident from figure 4.1 the mitral valve is a very complex structure and this is stressed in figure 4.2 where the circumferential geometry is represented on a plane. It can be noted that although there are two main leaflets, the anterior and the posterior, these have characteristic regions called segments and various chordae tendineae depart from each segment to the papillary muscles. The precise description of such an involved structure would be very difficult and also of reduced use on account of the high physiological variability among different individuals. We have therefore decided to extract the essential features of the valve by modeling the anterior and posterior leaflets of different dimensions and to gather all the chordae tendineae into four main bundles as in figure 4.2. Each chorda, which is essentially a band with zero thickness, departs from the edge of a leaflet and connects directly to the ventricle without the papillary muscle. The resulting geometry is close enough to the native valve to retain the main functionalities but, at the same time, simple enough to be handled within a simulation in which also the ventricle and the three-dimensional flow are considered.

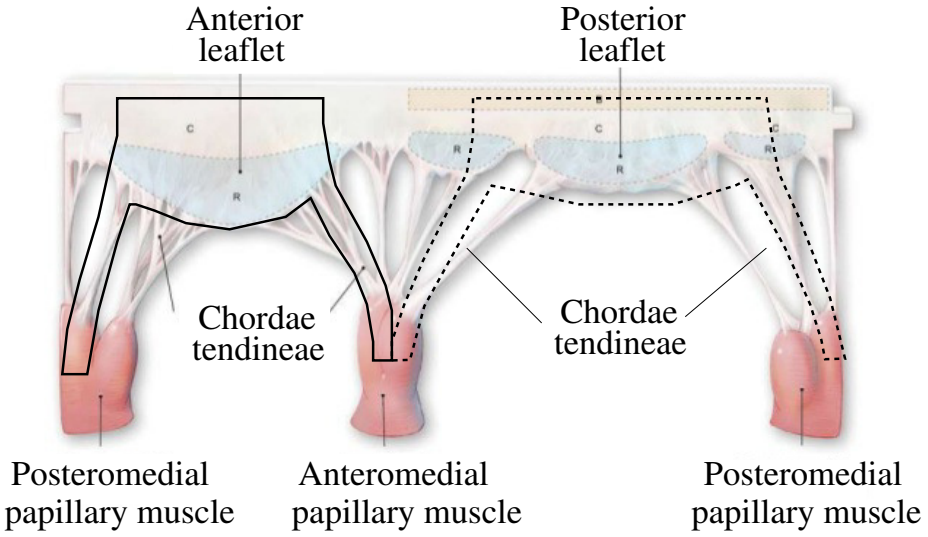

Figure 4.2: Sketch of the mitral valve geometry used in this study. In the background it is reported, for comparison, the geometry of a real native mitral valve.

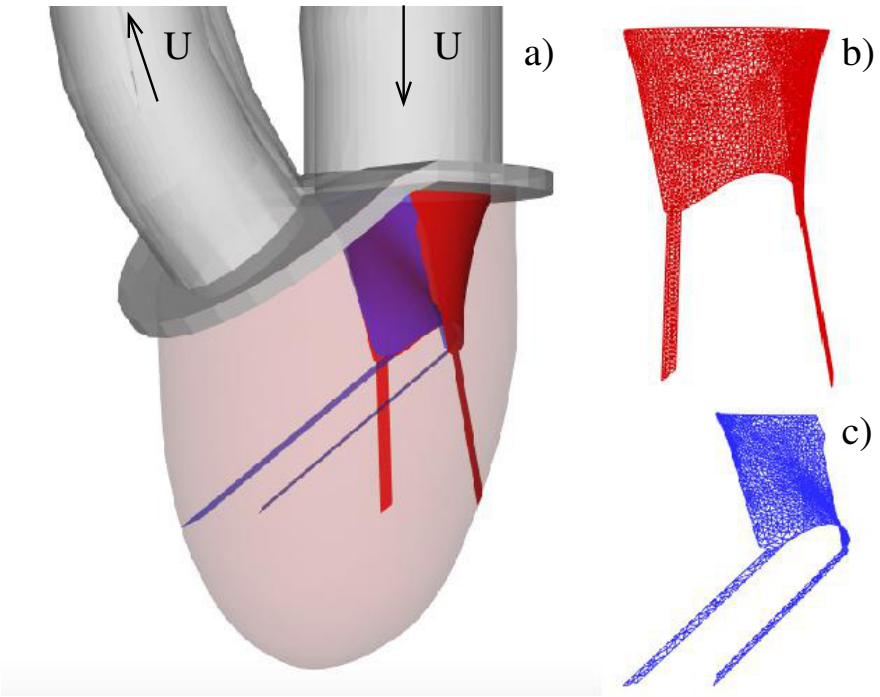

Figure 4.3: a) Numerical set-up for the chorded mitral valve with attachment points to the left ventricle wall. b) 3D mesh of the posterior leaflet provided of chordae tendineae. c) 3D mesh of the anterior leaflet provided of chordae tendineae

The overall assembly is shown in figure 4.3 in which the deformable valve and ventricle are both attached to a rigid frame which mimics the fibrous trigone of the real heart. The two ducts above the frame, referred to as mitral and aortic channels, are used to drive and extract fluid into the ventricle according to the profile of figure 4.4. This physiological law has two phases: the inflow made of two positive pulses, the E–wave and the A–wave, corresponding to the diastole of the left ventricle, and the outflow phase, the systole, when the fluid leaves the left ventricle through the aortic channel.

The inflow/outflow function is scaled to reproduce the function of a healthy left ventricle which is characterized by an ejection fraction $55\% \leq EF \leq 70\%$. Let $V(t)$ be the volume of blood in the ventricle during the heart cycle with a maximum V_M at the end of the diastole and a minimum V_m at the end of the systole. The difference $V_M - V_m$ is the volume of blood ejected from the ventricle and the ejection fraction is defined as the ratio $EF = (V_M - V_m)/V_M$: in this chapter we run all the simulations for an ejection fraction of 60%.

Similarly to Meschini *et al.* (2017) we do not model the aortic valve since it only regulates the flow between the ventricle and the ascending aorta and has a negligible influence on the ventricular flow and mitral valve dynamics. Nevertheless, in order to mimic the opening and closing of the aortic channel we fill the latter with a porous medium whose porosity tends to zero during diastole, thus obstructing the duct, and to infinity during systole to allow the fluid to leave the ventricle.

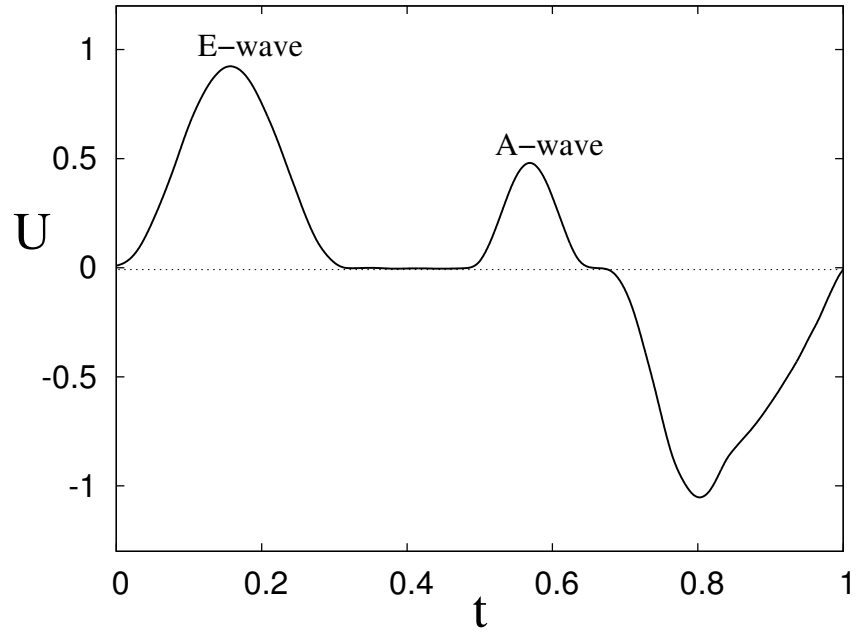

Figure 4.4: Time evolution of the inflow (positive values) and outflow (negative values) boundary conditions during a heart cycle.

4.2.3 Simulation parameters and experimental validation

The time integration of the model is performed with a variable time step which dynamically adjusts during the integration so to maintain the Courant number constant at $CFL = 0.2$. All the flow parameters and material properties are made dimensionless; the scaling length is the mitral orifice $D = 24$ mm while the velocity $U \simeq 0.75$ m/s is that at the peak inflow. As a result the Reynolds number is $Re = 4200$ for a blood with kinematic viscosity $\nu = 4.5 \times 10^{-6}$ m^2/s. A heart rate of 72 bpm has a period $T = 0.833$ s that corresponds to $T_{ad} = 25$ non–dimensional time units; throughout the chapter the phases of the cycle will be always scaled by T_{ad} so that they range in between 0 and 1.

All the simulations are run for a minimum of 5 heart cycles and the data collected for phase averages.

All the numerical simulations are run on a mesh of 129^3 nodes evenly distributed in all three directions. The grid spacing of 129^3 is chosen after convergence check analyses extensively discussed in Meschini *et al.* (2017). In that paper the case with the native valve without chordae has been run also on meshes 193^3 and 257^3 obtaining a substantial agreement. We add that although a mesh of 129^3 nodes might look coarse for a flow at $Re = 4200$ we should keep in mind that this is just the peak Reynolds number attained only in one instant of the cycle and the same parameter computed with the rms velocity is only $Re_{rms} = 660$. In addition, as shown in figure 4.4, the flow rate is pulsatile with accelerations, decelerations and stagnant phases therefore the flow is never forced for a long enough time to allow the energy to cascade from the largest to the smallest (Kolmogorov) scales.

A mesh of 129^3 nodes allows the modeled chordae tendineae to be discretized by 4–5 Eulerian cells and this has been found to be the marginal

resolution to capture their interaction with the flow. We wish to point out that an advantage of gathering several chordae into a single bundle is that the resulting structure has a bigger transversal (cross) section and a coarser Eulerian resolution can be used to describe its interaction with the fluid. Even within this simplifying hypothesis, a simulation with a chorded valve resulted 30–40% more expensive than the analogous without chordae the reason being a larger number of triangular elements for the structure and a smaller time step size for the system integration.

The ventricle is discretized by 3×10^4 triangles, while the two leaflets of the native mitral valve, including the four chordae tendineae, have a total of 9×10^3 triangles. These triangles are as close as possible to equilateral and the edges are about 70% of the local Eulerian grid spacing, in order to have the optimal efficiency of the immersed boundary method de Tullio & Pascazio (2016).

Even if the numerical results are grid independent this does not imply that they correctly describe the intended problem. For this reason we have performed an experimental validation of the numerical model by realizing a laboratory replica of the numerical set–up. Details of the experimental apparatus and measurement techniques can be found in Meschini *et al.* (2016, 2017); Spandan *et al.* (2017); here we show only the key element of the experiment in figure 4.5, The ventricle evolves into a sealed Plexiglas box which, when illuminated from the side, allows for measurements of the velocity field in a vertical symmetry plane by particle–image–velocimetry (PIV). If the same box is lighted from below the characterization of the mitral valve dynamics can be performed by recording the phenomenon from above.

In figure 4.6 we report the comparison of the velocity field for one representative instant of the cycle that, considering the cycle–to–cycle variability, is satisfactory.

Since the focus of this study is on the mitral valve we have also compared the time evolution of the mitral orifice area and the instantaneous results are illustrated in figure 4.7 for two representative phases of the cardiac cycle. The mitral orifice area is defined as the area delimited by the leaflets edges. We have scaled the instantaneous values to the maximum attained in the fully open position. The results are given in figure 4.8 and the agreement between numerical and experimental measurements is more than satisfactory. This is an important point to support the robustness of our computational model as well as the reliability of the numerical results.

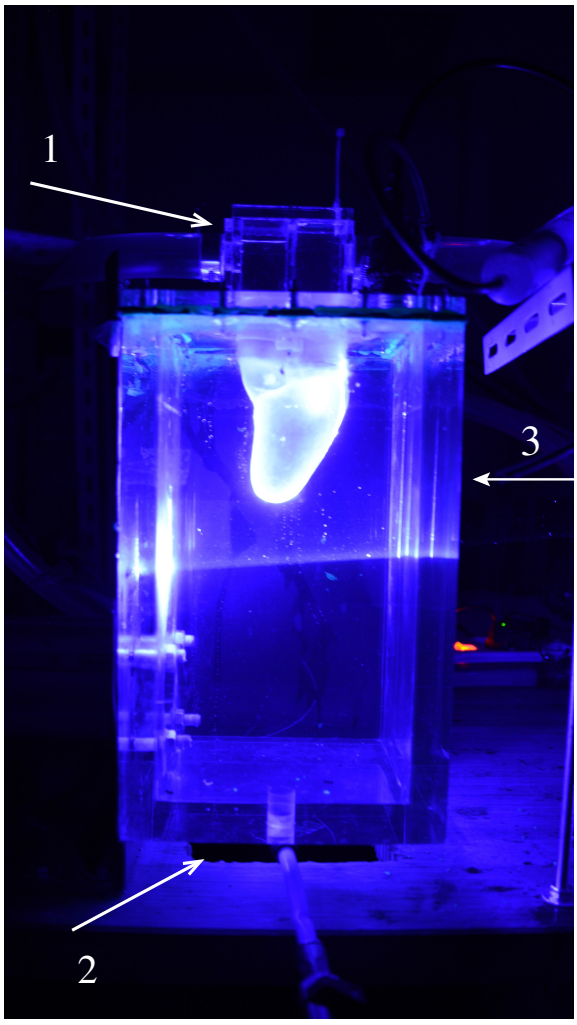

Figure 4.5: Detail of the experimental set–up with the left ventricle; by illuminating the system from below (**2**) it is possible to follow in time the dynamics of the mitral valve from above (**1**). Illuminating the ventricle from the side (**3**) the velocity field inside the ventricle in the vertical symmetry plane can be measured.

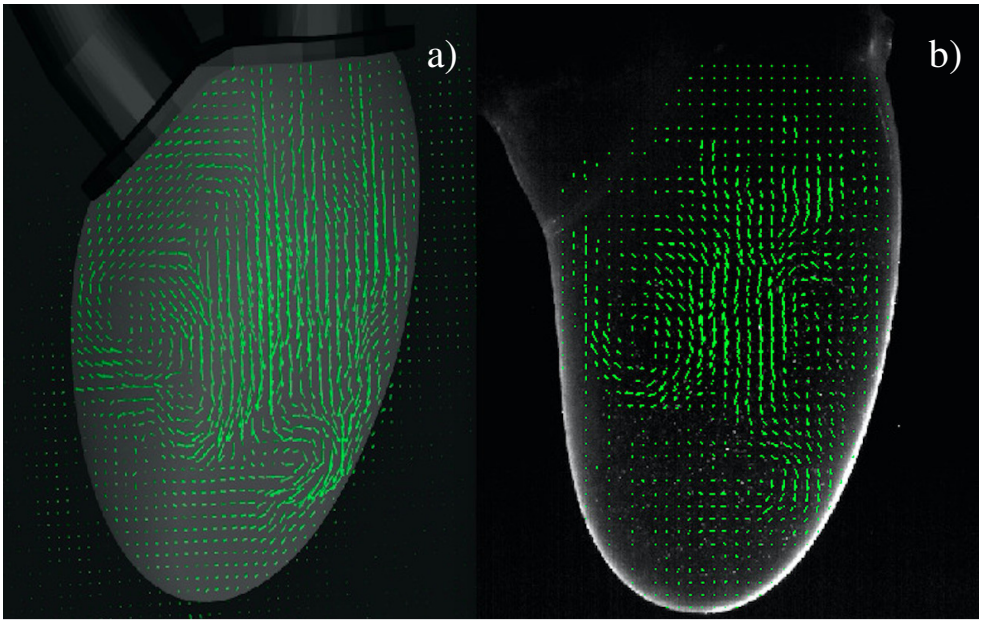

Figure 4.6: Two–dimensional velocity field in the vertical symmetry plane at $t = 0.25$ of the heart cycle: a) numerical simulation, b) laboratory experiment.

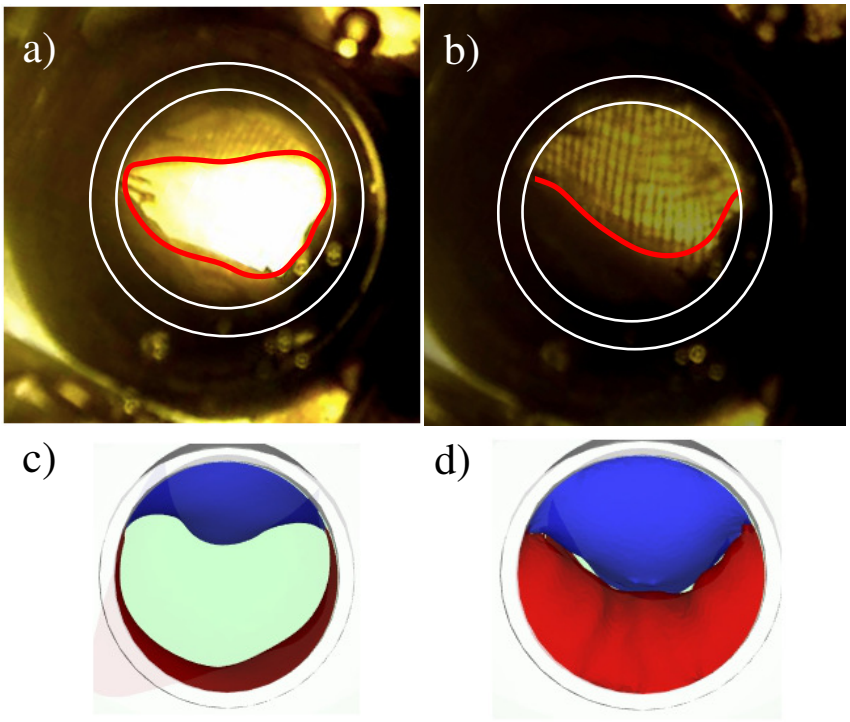

Figure 4.7: Instantaneous snapshots for the mitral valve dynamics during two phases of the cycle: a) and c) peak of the E–wave, b) and d) peak systole. a) and b) experimental visualization, c) and d) numerical simulation

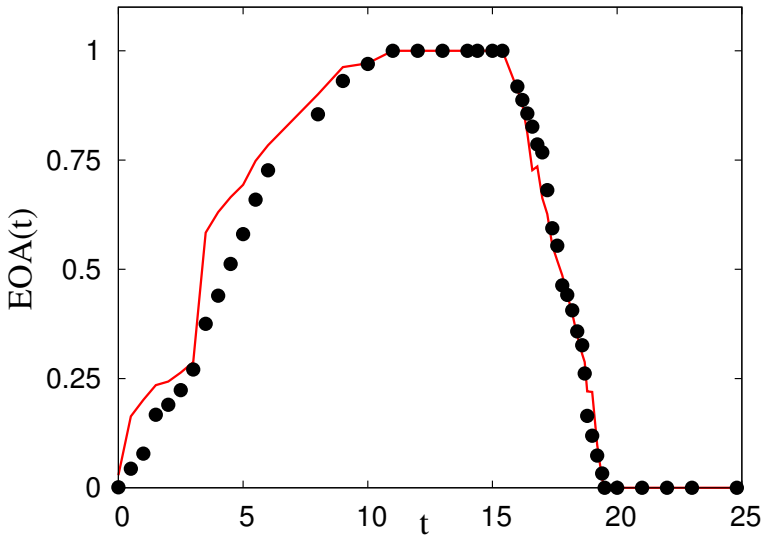

Figure 4.8: Comparison of the geometric orifice area (GOA) over a cardiac cycle between experimental measurements (continuum red line) and numerical results (dotted black line).

4.3 Results

We take as a guideline the curve in figure 4.4 to describe the different ventricular flow features in the cycle; during early diastole the E–wave accelerates the flow through the mitral orifice opening the valve and producing a strong jet. This jet is initially bent towards the ventricle surface owing to the asymmetry of the leaflets and it sweeps the lateral wall (figure 4.9a). In this part of the cycle the chordae are inactive since when the leaflets open the chordae can not resist compression and they crumple. As the peak E–wave is attained, the leaflets open wider and the jet points vertically downward to reach the ventricle apex (figure 4.9b) and generating a strong recirculation (figure 4.9c). During the A–wave another jet is produced and the previous process repeats although with weaker intensity. During late diastole ($t = 0.65$) the ventricle attains its maximum volume and the chordae their maximum elongation. At the beginning of systole, the fluid leaves the ventricle both, from the aortic and the mitral channel. However, the low pressure induced by the accelerating back flow through the mitral leaflets seals them thus closing the valve and preventing further leakage (figure 4.9e). In this phase, the same pressure force that keeps the leaflets pressed one against the other would also evert them into the mitral channel if a reaction force did not oppose. The chordae tendineae, with their pull back tension, have exactly this function; they assure the perfect closure of the leaflets and maintain the correct valve configuration all over the systole. With the mitral valve closed the flow can leave the ventricle only through the aortic channel, the ventricle shrinks and also the chordae tendineae shorten (figure 4.9f) until the initial configuration is recovered and a new cardiac cycle can start.

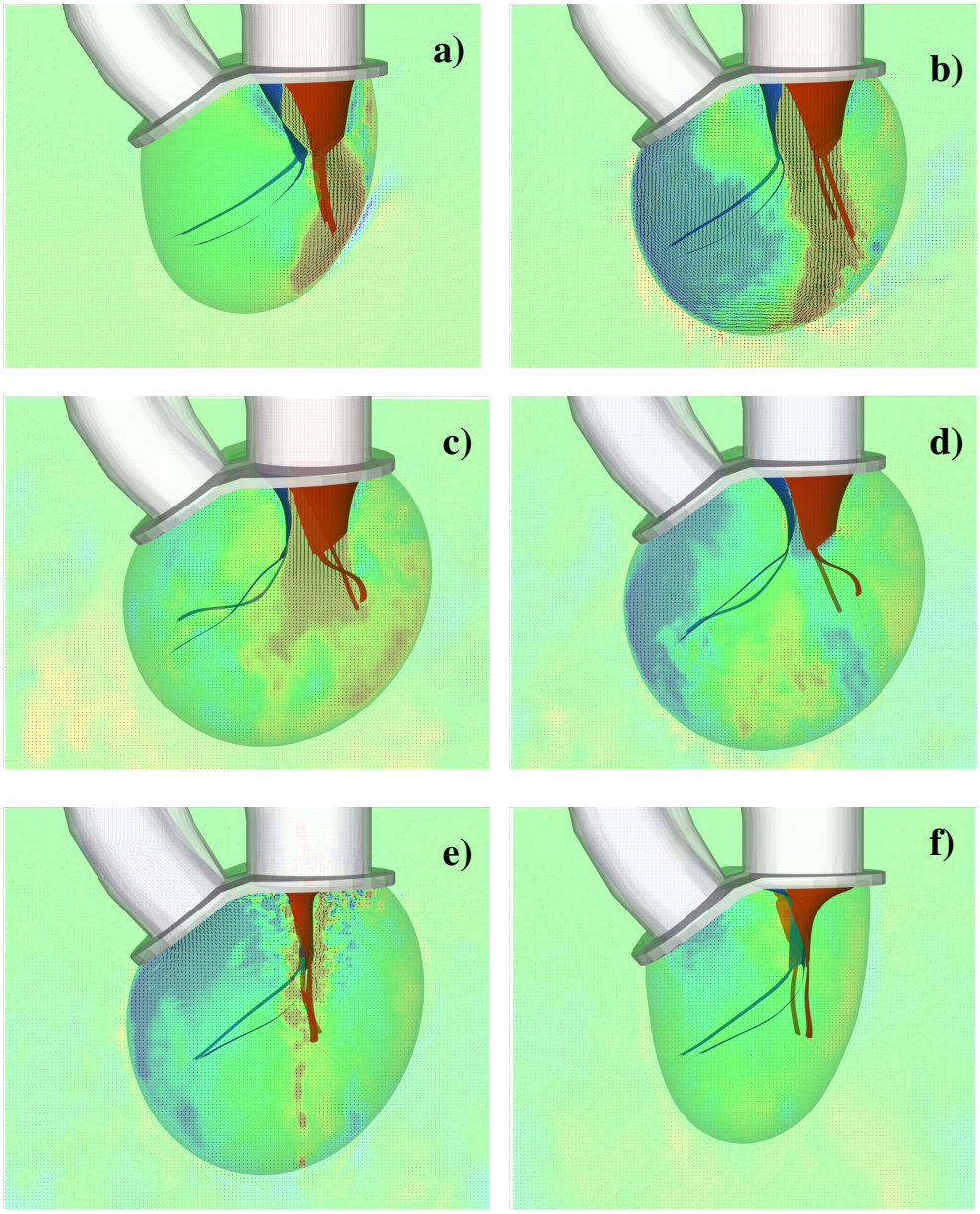

Figure 4.9: Snapshots of the velocity vector in the x–z symmetry plane and contours of vertical velocity (range is $-2 \leq v_z \leq 2$ from blue to red) at $EF = 60\%$ with chorded mitral valve: *a)* early E–wave, *b)* peak of the E-wave, *c)* peak of the A-wave, *d)* early systole, *e)* peak systole and *e)* end of systole.

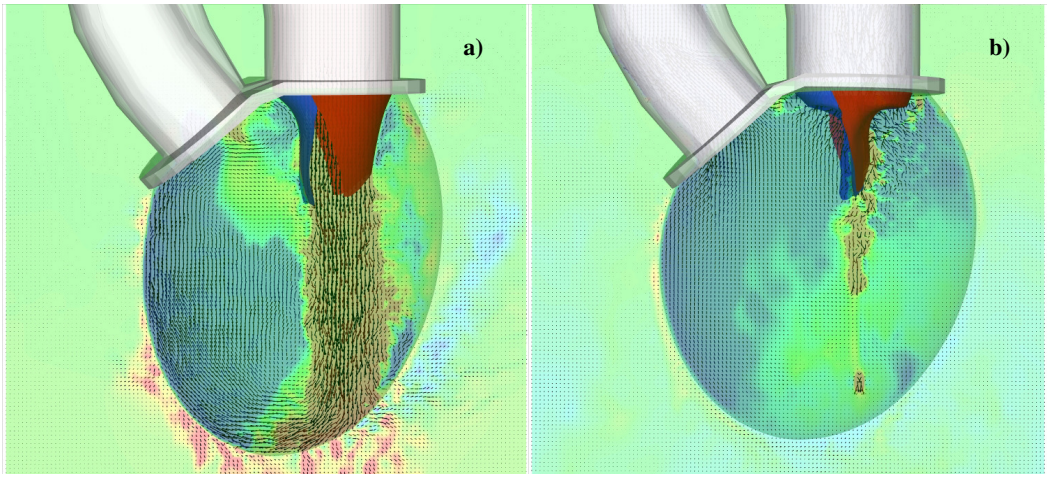

Figure 4.10: Snapshots of the velocity vector in the x–z symmetry plane and contours of vertical velocity at $EF = 60\%$ with non chorded mitral valve: *a)* peak of the E–wave, *b)* peak–systole.

We compare these results with those obtained for a non chorded mitral valve. In figure 4.10 two snapshots, respectively, at the peak E–wave and peak systole are shown: figures 4.10a and 4.10b therefore correspond to the same instants as in figures 4.9b and 4.9e. It can be noted that, thanks to the pulling action of the chordae tendineae, the mitral valve opens wider while during systole the leaflets get closer to each other. Another difference is the shape of the ventricle that is more elongated axially for the non chorded valve. Since at any instant the volume ventricle is fixed by the flow rates of figure 4.4 the different shapes are clearly due to the presence of the chordae. In fact, the same pulling force that keeps the leaflets in place during systole reduces also the axial deformation of the ventricle during diastole. It is worthwhile to point out, however, that this result deserves further investigation in order to separate the real effects on the heart from the artifacts of the present model; in the latter, in fact, the ventricle is modeled as a thin membrane that passively adapts to an imposed flow rate while the myocardium has an average thickness of ≈ 1 cm and contracts actively owing to an electrical signal that propagates from the apex along a complex spiraling path. This implies that the traction of the chordae is likely to have different effects on the two systems and a more realistic ventricle model should be implemented before drawing conclusions.

The above description of the mitral leaflet dynamics is confirmed by the time evolution of the leaflets centroids shown in figures 4.11 and 4.12; clearly the most relevant differences with the non chorded valve occur during the closure since for the chorded valve the pulling back of the chordae keeps the leaflets in place while for the non chorded valve the prolapse is prevented by imposing a kinematic condition that ‘freezes’ the leaflet position immediately after the initial systolic closure up to the end of the cycle. Figures 4.11 and 4.12 also show that the posterior leaflet is the one most affected by the action of the chordae whereas the dynamics of the anterior one is hardly influenced except for the part of the cycle when the valve is closed.

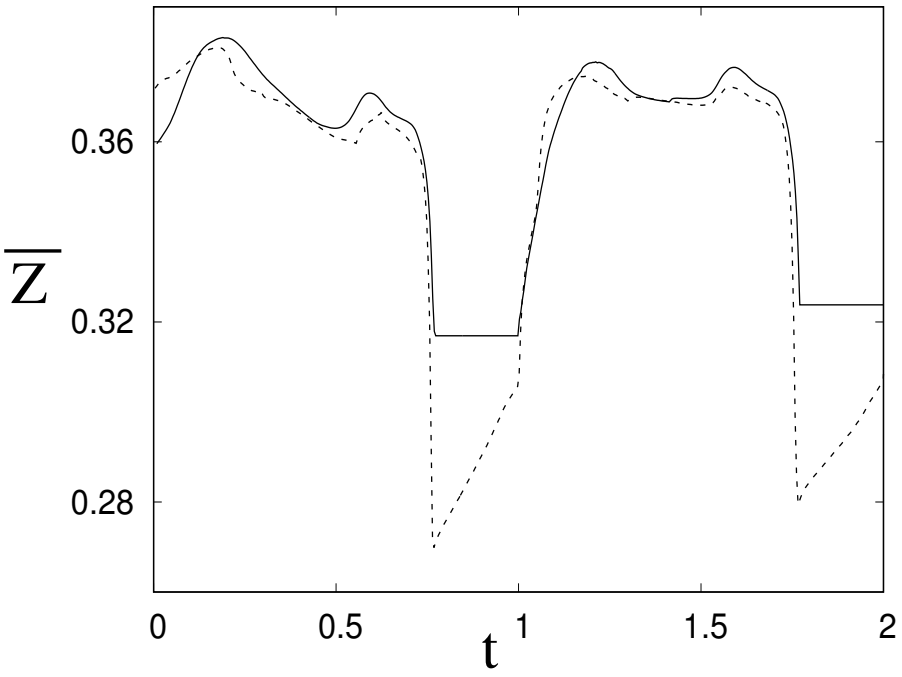

Figure 4.11: Mean z–displacement of the anterior mitral leaflet: —— non corded–, ---- corded–valve.

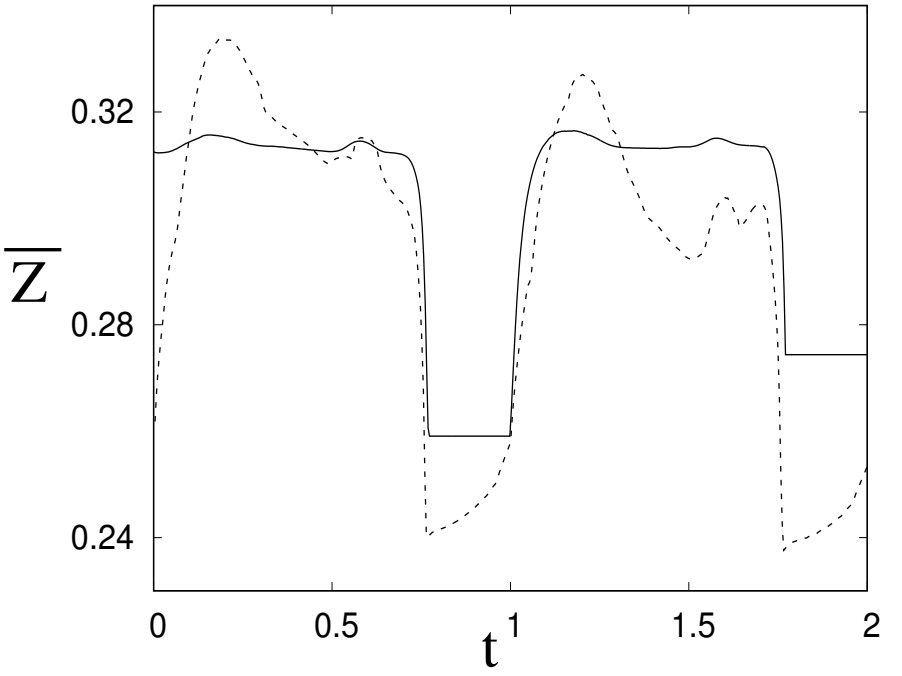

Figure 4.12: Mean z–displacement of the posterior mitral leaflet: —— non corded–, ---- corded–valve.

In figure 4.13 the phase averaged velocity magnitude sampled from a probe located at the ventricle apex is shown; although the behaviours are similar, the velocity for the chorded valve is more intense either during the E–wave and the A–wave thus indicating a more efficient ventricle 'washing' produced by the chorded valve. The stronger apical flow is beneficial for the ventricle physiology since it avoids the blood stagnation (referred to as hemostasys) that could generate clots, Badas *et al.* (2016).

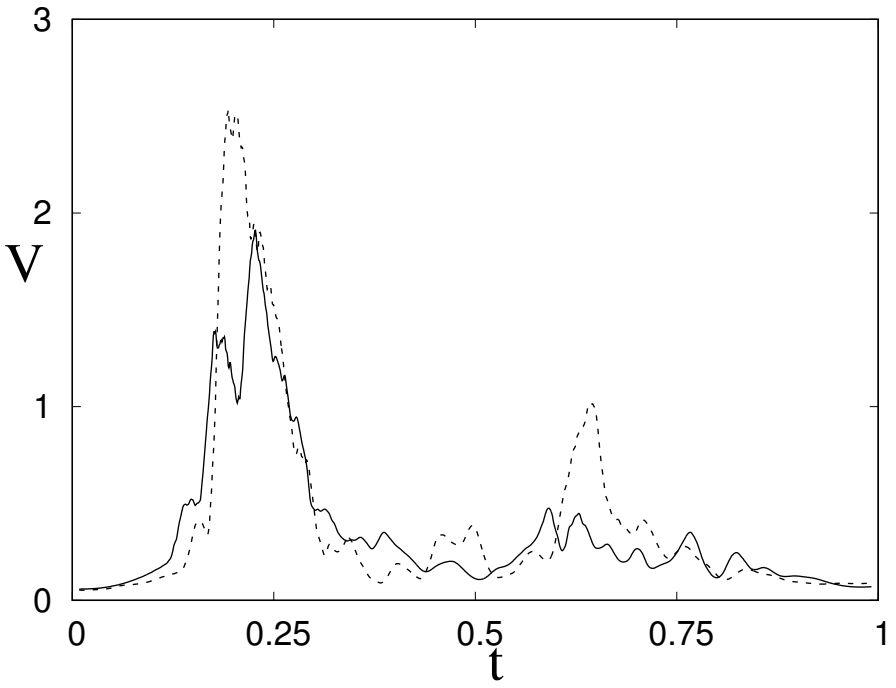

Figure 4.13: Time evolution of the velocity magnitude at a probe in the ventricle apex: —— non corded–, ---- corded–valve.

Although the apical flow is stronger with a chorded valve, the presence of the chordae within the ventricle generates additional dissipation and this is evidenced in figure 4.14 with the phase averaged kinetic energy of the ventricular flow within a cycle. It can be noted that, even if the flow rates are identical for the two cases, the flow with the chorded valve is constantly less energetic than for the other case. This is especially true during the peak E–wave when the velocities the strongest and the drag exerted by the chordae presumably the highest.

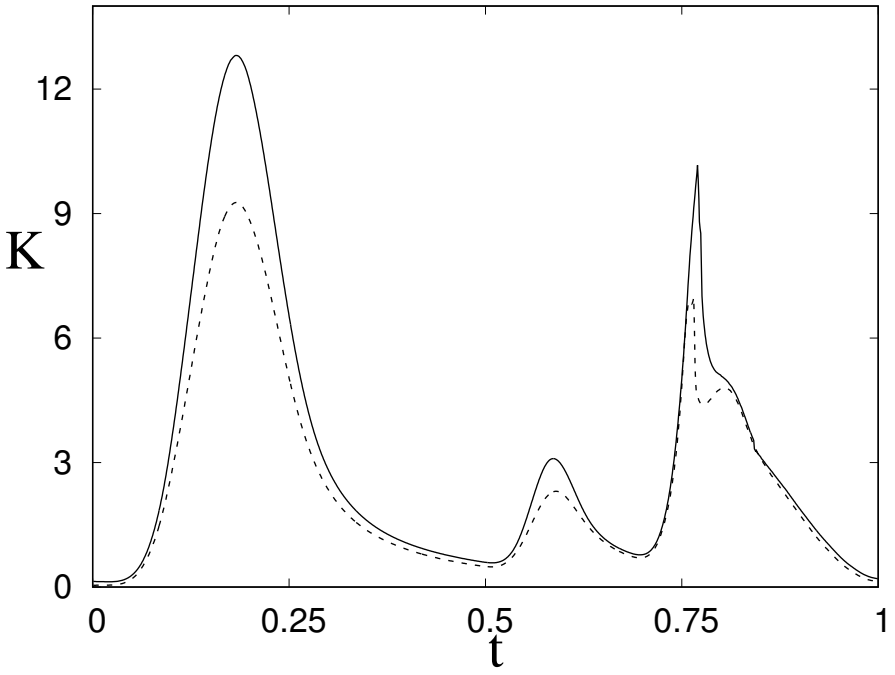

Figure 4.14: Time evolution of the kinetic energy of the intra ventricular flow: —— non corded–, - - - - corded–valve.

4.4 Closing remarks

In this chapter, the flow in the left ventricle coupled with chorded mitral valves has been studied by FSI numerical simulations for a healthy left ventricle with an ejection fraction $EF = 60\%$. The model has been proven to be computationally efficient and to yield reliable results which are consistent with the experimental. It has been found that, even thought the function of the chordae tendineae on the mitral valve leaflets can be replaced by ad hoc kinematic conditions, their effects on the whole system is more complex and it involves either the fluid dynamics, with a better apical washing and a more dissipative recirculation, and a different ventricle deformation caused by the pulling action of the chordae on the myocardium. This is consistent with the view of the heart as a highly synergistic system in which every part works in combination with the others and influence each other dynamics.

We believe that the inclusion of the chordae tendineae in an already complex left ventricle models is an important step forward an uncompromised model of the heart. However, it is worth mentioning that still there are features that need to be accounted for and the model development is a restless process. A natural extension would be the inclusion of the papillary muscles which tether the chordae tendineae to the ventricle wall and also to replace the passive adaptation of the ventricle to an imposed inflow with an active contraction driven by the propagation of the electrical stimulus. This will contribute to the realization of a much more realistic and reliable model: we are already working in these directions and the developments will be the topic of forthcoming papers.

Chapter 5

Flow–induced mitral leaflets motion in Hypertrophic Cardiomyopathy

Based on: Valentina Meschini, Rajat Mittal & Roberto Verzicco, 'Flow–induced mitral leaflets motion in Hypertrophic Cardiomyopathy', in preparation.

5.1 Introduction

Hypertrophic cardiomyopathy (HCM) is a complex but relatively common form of genetic heart disease that occurs in 1 out of 500 people, (Maron *et al.*, 1995), even if it often goes undiagnosed in the community. It represents one of the most common cause of cardiac sudden death in people under 30 years, especially in young sportive men. From medical imaging techniques it is found that its occurrence comes together with the thickening of the septum between the left and right ventricles, as shown in figure 5.1 at different severity levels, and also combined with the abnormal growth of part of it inside the left ventricle, thus obstructing blood flow into the aorta during systole and causing sudden death.

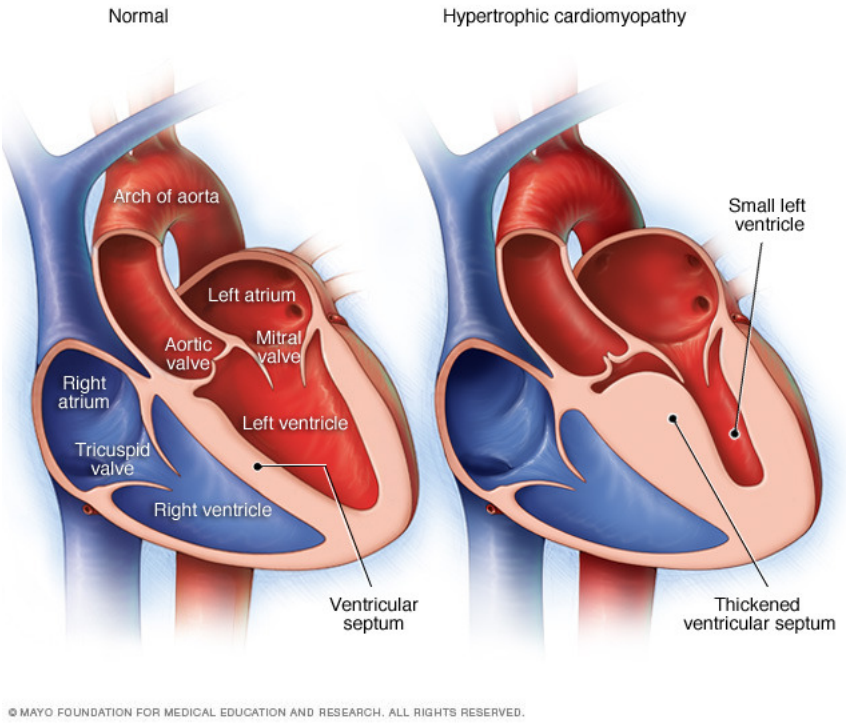

Figure 5.1: Schematic of a) physiological left ventricle, b) hypertrophic left ventricle (http://www.mayoclinic.org/diseases–conditions/hypertrophic–cardiomyopathy/home/ovc–20122102).

Moreover the majority of patients affected by HCM presents elongated anterior and posterior mitral leaflets with respect to normal subjects, (Maron *et al.*, 2014). On echocardiography it has been noted that these elongated leaflets extend into the left ventricle cavity well above the plane of the mitral annulus. This is crucial in understanding the cause of obstruction of the left ventricle outflow tract which has been identified in the systolic anterior motion of the mitral valve leaflets. The pathophysiology of systolic anterior motion consists in the movement of the anterior or both leaflets of the mitral valve towards the intra ventricular septum; this is induced by the low pressure and accelerating flow in the obstructed region of the left ventricle near the outflow

tract. The understanding of the cause of leaflets migration has been the topic of debates among cardiac surgeons and still has to be understood whether it is a push/pull mechanism of the leaflets or a sort of Venturi effect in the outflow responsible for this phenomenon.

Different levels of obstruction of the left ventricle are identified by the medical doctors using the transvalvular pressure gradient as reference quantity. The difference between the pressure values inside the left ventricle (behind the aortic valve) and the ones close to the outflow tract (above the aortic valve) is measured; if this value is < 30 mmHg medical doctors refer to HCM, while if it is ≥ 30 mmHg they refer to obstructive HCM (OHCM), Naidu (2015). Although HCM is a chronic disease without a known cure, a number of treatments are now available to alter its course. Typical therapies for HCM/OHCM are septal myectomy, that is surgical removal of the abnormal grown portion inside the ventricle, and mitral leaflet plication thus resulting in shortened leaflets, (Feins *et al.*, 2014). Both these possibilities have their risks and advantages; a choice between them is made by the surgeons analyzing the specific clinical case on the base of echocardiography and Doppler ultrasound, (Mittal *et al.*, 2016).

The above considerations underline the potentialities of efficient computational models able to capture the dynamics of HCM which could significantly advance the diagnosis process and treatments efficacy of such disease, thus leading to improved outcomes for patients and reduced health care costs.

To this purpose in this chapter we present a FSI computational model for the left ventricle and mitral valve aiming at describing the patho–physiology of HCM/OHCM and focusing on the ventricular flow and systolic mitral leaflet dynamics. A parametric study is performed for different levels of ventricle hypertophy starting from the physiological case up to a severe hypertrophic ventricle, and for two valve leaflets lengths, pathological and physiological. In addition to give a complete overview a case with the maximum severity of hypertrophy but reduced pumping efficiency is set up in order to evaluate the effects of these parameters on HCM occurrence. Finally the surgical procedures of leaflets plication and septal myectomy are simulated and comparisons between the resulting flow and leaflets dynamics are made in order to assess the efficiency and reliability of these surgical procedures.

This chapter is organized as follows. In the next section the numerical set–up, the numerical algorithm and the flow and structure parameters are given. In Section 3 the results obtained for different levels of hypertrophy, physiological and elongated leaflets, and the two surgical interventions are presented and analysed. The closing remarks are given in the final section.

5.2 The computational model for Hypertrophic Cardiomyopathy

5.2.1 The numerical set–up

In this study in order to capture the general dynamics of the system all the computational geometries have not not been extracted from specific clinical images but are rather realized using modeling software.

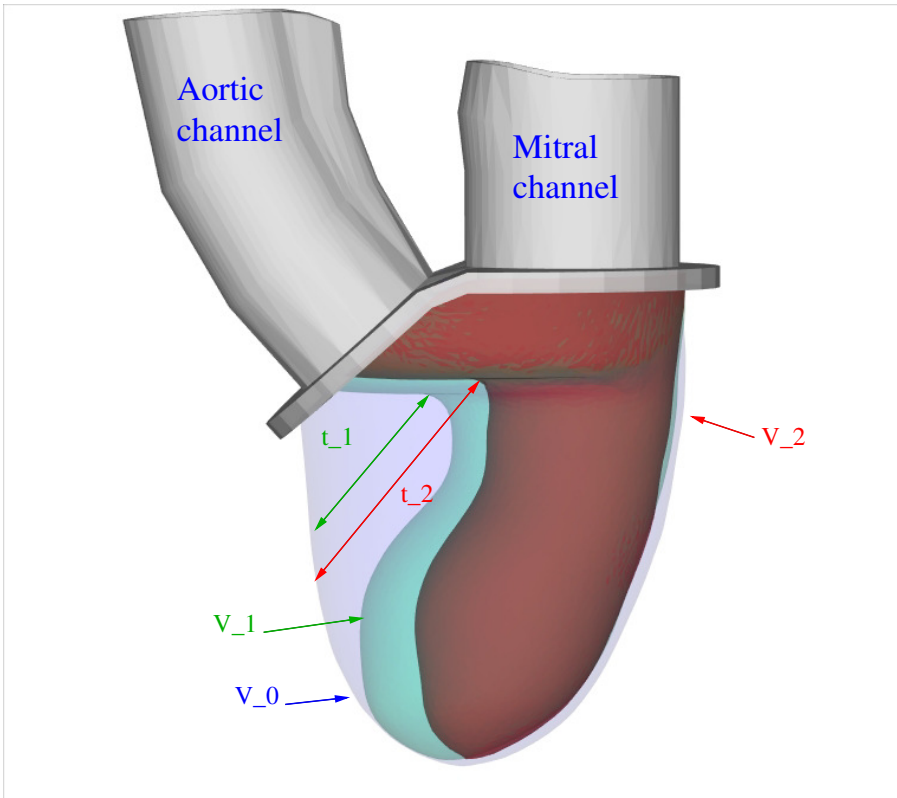

Figure 5.2: Three geometries for the left ventricle: physiological ventricle (blue shaded), a first level of hypertrophy left ventricle (green shaded), a second level of hypertrophy left ventricle (red solid).

In figure 5.2 the three different ventricle geometries are shown: the physiological left ventricle (blue shaded) with an initial non–dimensional volume $V_0 = 4.3$ and no thickening of the septum; a ventricle with a first level of hypertrophy, a thickening t_1 and a smaller volume $V_1 = 2.9$ (green shaded); a ventricle with a severe thickening of the septum t_2 and an even smaller volume $V_2 = 2.2$ (red solid). The contraction and relaxation of the ventricles are not active and they passively adapt to a flow rate function, as shown in figure 5.3. This function is composed of a first inflow phase, the diastole, where $U(t)$ is positive and the flow is pumped inside through the mitral channel. In the second outflow phase, the systole, in which $U(t)$ is negative and the fluid leaves the left ventricle through the aortic channel. The level of health of the left ventricle can be quantified by its ejection fraction (EF); let $V^*(t)$ be the volume of blood in the ventricle during the cardiac cycle with a maximum V^*_M at the end of the diastolic phase, when the myocardium is fully relaxed, and a minimum V^*_m at the end of the systolic phase, when the myocardium ends its contraction; the difference $V^*_M - V^*_m$ is the amount of blood ejected from the ventricle during one cycle and the ejection fraction is defined as the ratio $EF = (V^*_M - V^*_m)/V^*_M$. This parameter has some variation among individuals but values $55\% \leq EF \leq 70\%$ are considered physiological; in this study we impose an ejection fraction of 60%.

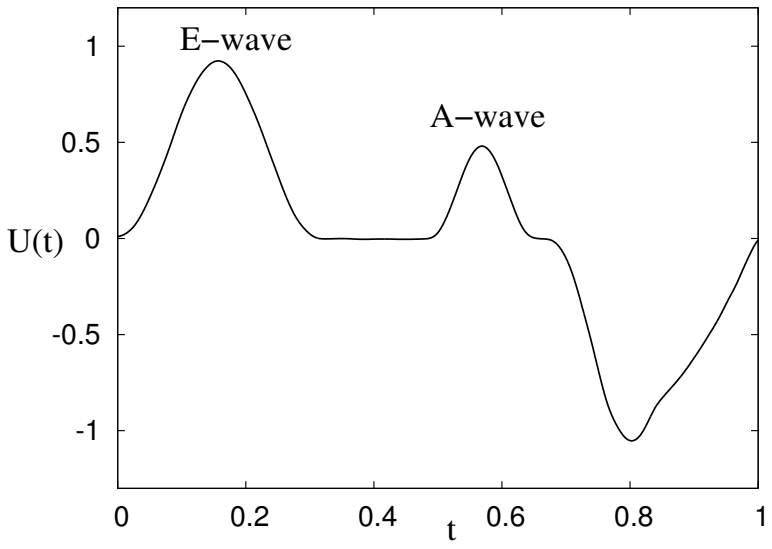

Figure 5.3: Flow rate function $U(t)$.

The mitral and aortic channels together with the valve planes (in grey in figure 5.2) are modeled as a rigid structure that is used as a frame to anchor the deformable ventricle and the valve leaflets.

The numerical set–up is completed by the leaflets of the mitral valve which are found to be elongated in case of HCM; the two geometries of figure 5.4, one for the physiological 5.4a and another for the pathological case 5.4b, are used for comparison. Since we use deformable membranes a crucial point that needs to be addressed is the modeling of the contact mechanism between the ventricle and the leaflets of the valve and especially between the two leaflets. We model each structural element by a triangular mesh whose nodes are evolved in time according to the equations of membranes, as already described in chapter 3, to model the contact of deformable structures we use an array that is null in the fluid and assumes a specific integer value, different for each body, in the cell occupied by the nodes of a specific body. The value in the cell is updated every time step and if a triangle ends up in a non null cell, meaning that the position is already occupied by another triangle, then the velocities of both surface elements are set to their average so that they can still freely move together in space but cannot compenetrate. The same procedure is used to model the contact between the leaflet and the ventricle, but once a triangle ends up in a non null cell the velocities are reversed in sign to induce a sort of re–bound. We have found that this approach is efficient and allows the valve to close without prescribing a coaptation zone but, at the same time, it prevents the compenetration between the leaflets and between leaflets and ventricle.

Finally we want to underline that we do not model a physical aortic valve, since it regulates the outflow of the ventricle and has a minor impact either on the intra-ventricular flow and on the mitral valve dynamics. For this reason, in order to reduce the computational load we only introduce a numerical procedure to mimic its opening and closing. We simulate the presence of a porous medium in the aortic channel whose porosity tends to zero during di-

astole thus preventing the fluid from exiting the left ventricle and to infinity during systole so that the fluid can leave the ventricle.

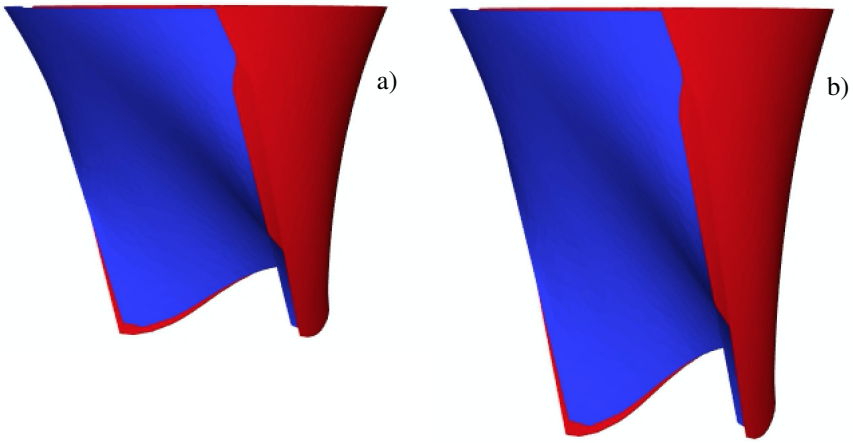

Figure 5.4: Anterior leaflet (blue) and posterior leaflet (red) of the mitral valve in the a) physiological case and b) pathological HCM case.

5.2.2 The numerical method

The numerical scheme consists of a flow solver two–way coupled with a structure solver, which is essentially the one presented by de Tullio & Pascazio (2016), Spandan *et al.* (2017) and Meschini *et al.* (2017). We refer the previous references for a detailed description of the method, the convergence checks and the experimental validation of the model; here we report only the main features.

The Navier–Stokes equations are employed to describe the motion of the blood as an incompressible and viscous fluid, which in non dimensional form read

$$\frac{\partial \mathbf{u}}{\partial t} + \mathbf{u} \cdot \nabla \mathbf{u} = -\nabla p + \frac{1}{Re} \nabla^2 \mathbf{u} + \mathbf{f},$$
$$\nabla \cdot \mathbf{u} = 0,$$

where $\mathbf{u}$ is the velocity, p is the pressure and $\mathbf{f}$ is a body force term related to the immersed boundary technique. It has to be mentioned that despite the blood is a non–Newtonian fluid, here it is assumed Newtonian since it is known that its non–Newtonian nature does not arise in large vessels. However in our code the non–Newtonian feature is already implemented with the Carreau Yasuda model and in section 3.3.2 a simulation with non–Newtonian blood is carried out; it is shown that there is substantial agreement in the intraventricular flow and also the dynamics of the mitral valve is correctly represented.

The structure deformation is solved using an interaction potential approach with a spring–mass model. This idea was first introduced in Tanaka *et al.* (2012) and then applied to study different fluid–dynamics phenomenon in de Tullio & Pascazio (2016), Spandan *et al.* (2017) and Meschini *et al.* (2017).

The immersed surfaces of the ventricle and mitral valve are discretized using triangular meshes composed of almost equilateral triangular elements. Elastic springs are used to connect among them the vertices of the triangles, where the total mass of the body is uniformly distributed. The system appears as a complex network which deforms according to the external forces and internal reactions, given by elastic, bending, area and volume energy which is stored into the system. Assuming the structure as an isotropic membranes, the model constants are computed based on the material properties following the Van Gelder model, (Van Gelder, 1998).

Two different IBM are employed to simulate the influence of the structure on the fluid and vice versa. For the moving and deformable bodies we use the moving least square approach of Vanella & Balaras (2009) because, despite the computational cost, it gives a more precise computation of the structure deformations; while for rigid structures a much computationally cheaper direct–forcing approach of Fadlun *et al.* (2000) is employed.

A loose coupled FSI algorithm is employed to describe the synergistic interaction of fluid and structure components of the model. Moreover it is combined with a time substepping procedure to advance the structure deformation: starting from the flow and structure at the time t^n, the flow at the new time ($t^{n+1} = t^n + \Delta t$) is computed; then the structure is advanced with a time substep $\Delta t_s = \Delta t/S$, using the hydrodynamic loads at t^n and t^{n+1}, typically a value $S = 100$ is used in all the simulations.

5.2.3 Simulation parameters and convergence checks

As discussed in chapter 3, after a careful grid independence study a grid resolution of 129^3 is used in all simulations performed in this chapter. In order to maintain the optimal ratio between the Lagrangian (triangular) and the local Eulerian meshes of about 70%, (de Tullio & Pascazio, 2016), the left ventricle has been discretized by 3×10^4 triangles while the two leaflets of the natural mitral valve have a total of 8×10^3 triangles. The material properties and flow parameters are made dimensionless using the mitral orifice diameter $D = 24$ mm, the velocity $U \simeq 0.75$ m/s at the peak inflow and the fluid density $\rho = 1000 Kg/m^3$. Considering a blood with kinematic viscosity $\nu = 4.5 \times 10^{-6}$ m^2/s, the resulting Reynolds number is $Re = 4200$. A heart rate of 72 bpm has a period $T = 0.833$ s that corresponds to $T_{ad} = 25$ non–dimensional time units. The time integration has been performed at constant Courant number $CFL = 0.2$ with a dynamic time step that adjusts during the integration so to keep the CFL constant.

We refer to sections 3.2.3 and 4.2.3 of this thesis in which two different one–to–one experimental validations are provided on the flow dynamics inside the ventricle, on the structure deformation and on the mitral valve dynamics comparing the numerical and experimental orifice area of the mitral valve. As a result in both validations the matching of experimental measurements and numerical results is obtained for the large scale features of the ventricle deformation, mitral valve and flow dynamics.

5.3 Results

In this section we report the results obtained for the three different geometries of the left ventricle, each one with a different hypertrophy level, and for two lengths of mitral valve leaflets: normal, referring to a physiological case, and elongated, related to the pathological HCM. The reference case which is used as a guideline to replicate the pathological behaviours of the HCM is the one shown in figure 5.5, where we can see medical imaging from an ecocardiography of a patient affected by HCM. Four sequential snapshots are extracted at some representative instants so to introduce the dynamics of the flow, the ventricle and mitral valve deformation.

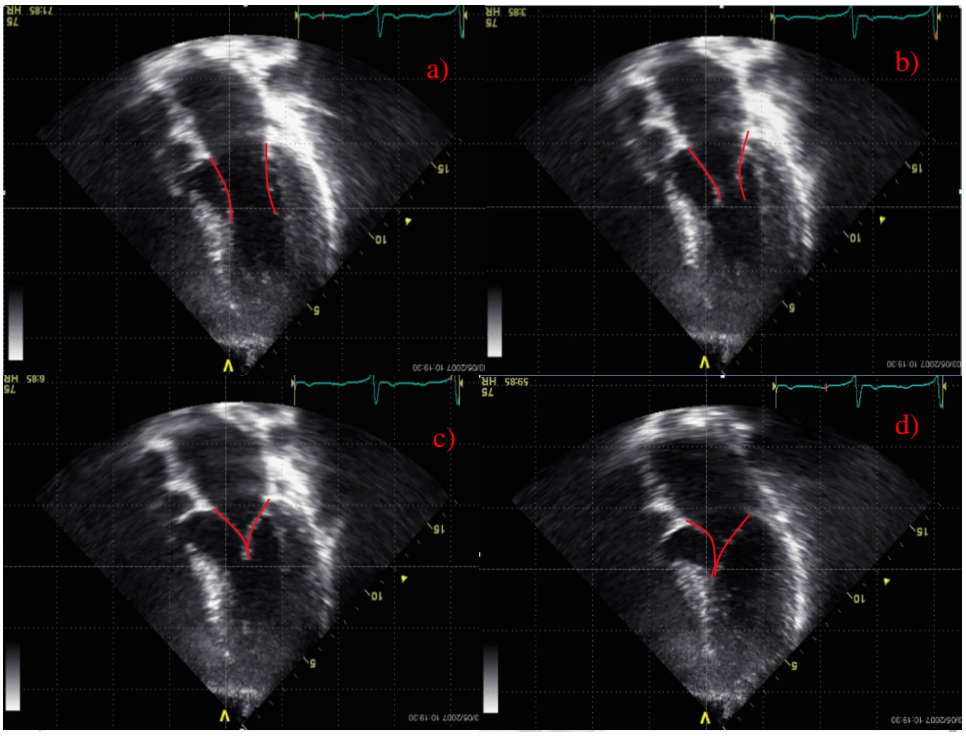

Figure 5.5: Snapshots of the ecocardiography of a patient affected by HCM in selected instants of the cardiac cycle: a) peak of the E–wave, b) peak of the A–wave, c) mid–systole, d) end–systole.

The blood from the left atrium is pumped into the left ventricle through the mitral orifice, the valve starts opening until the peak of the E–wave is reached and the maximum opening position is attained, figure 5.5a; then the fluid starts recirculating inside the left ventricle and the valve leaflets tend to get closer until a new injection is produced by the A–wave opened again by the incoming mitral jet, figure 5.5b. Then systole starts and the leaflets of the mitral valve begin to close until they seal, figure 5.5c, because of the counter pressure. After mitral valve closes the flow leaves the ventricle through the aortic channel where, because of the pathologically thickened septum, has a strong acceleration that produces abnormal local low pressure. The mitral leaflets, therefore experience an anomalous lateral pressure gradient that moves them to the left up to the thickened septum, figure 5.5d.

We start from these clinical data as reference and perform a parametric

study better investigate under which conditions this pathological behaviour is observed. In order to have a range of behaviours we analyze the following configurations: a first hypertrophic ventricle, with an EF of 60% and elongated leaflets (section 5.3.1); a second hypertrophic ventricle with an increased thickening of the septum and elongated leaflets (section 5.3.2); a physiological ventricle with no hypertrophy but with elongated leaflets (section 5.3.3). Moreover in the second case of more severe hypertrophy and longer leaflets we also run a simulation with reduced pumping efficiency ($EF = 40\%$), in order to assess its effects on HCM (section 5.3.4). Finally the surgical interventions of leaflets plication and septal myectomy are analysed in the case of severe hypertrophy and simulated to evaluate their effectiveness in reducing the migration of mitral leaflets and the consequent obstruction of the outflow aortic tract (section 5.3.5).

5.3.1 HCM: a first case of left ventricle hypertrophy with elongated leaflets

We start by presenting the flow and the leaflets dynamics for a case of hypertrophic ventricle with $EF = 60\%$. The numerical set–up is the one described in section 5.2.1 and illustrated in figure 5.4b: the leaflets are elongated and the ventricle has an initial volume $V_1 = 2,9$ with a relative volume with respect to the non hypertrophic case of $\frac{V_1}{V_0} = 67\%$. In figure 5.6 four instantaneous snapshots of the velocity vector field colored with the values of the vertical velocity at the same representative instants as in figure 5.5 are shown for make comparisons. The blood from the left atrium enters the left ventricle and is injected through the mitral channel by the inflow function of figure 5.3. As the flow rate evolves, the elongated leaflets of the mitral valve drift apart and the mitral jet, due to the asymmetry of the leaflets, initially points transversally to the lateral wall, figure 5.6a; then it sweeps up to the ventricle apex and starts recirculating inside it until a second weaker jet of incoming fluid is produced, figure 5.6b. As the fluid is pumped inside the ventricle owing to the synergistic functioning of fluid and structure, the left ventricle expands less than in the physiological case because of the thickened septum. As systole starts, the ventricle contracts and the fluid initially leaves the ventricle both from aortic and mitral channels until the mitral valve closes, figure 5.6c. After this point the fluid continues to exit only from the aortic channel. The thickened septum reduces the outflow region which, in turn, induces abnormal high velocity and low sub–valvular aortic pressure; this results in the migration of the mitral leaflets towards the aortic channel (figure 5.6d) which is referred to as systolic anterior motion. In the most severe cases the leaflets can attach to the ventricle septum thus producing the obstruction of the aortic valve. It is worth mentioning that in this movement the mitral leaflets could also open and produce mitral regurgitation; in this case, even if the leaflets slightly open in the region next to the mitral annulus, mitral regurgitation does not occur since they remain sealed at the tips. The time evolution of the leaflets motion is shown in figure 5.7 for the x–centroid, $\overline{X}$. As in the physiological case, the posterior leaflet moves less than the anterior up to the point of full closure ($t \approx 0.76$) then both leaflets experience a steeply decrease of $\overline{X}$ which indicates the abrupt migration towards the ventricle septum. Once the leaflets get close the septum they remain in that pathological position up to the end

of systole when the fluid stops leaving the ventricle and the pressure recovers physiological values.

This dynamics is consistent with the above clinical picture and the occurrence of systolic anterior motion is confirmed for the selected configuration.

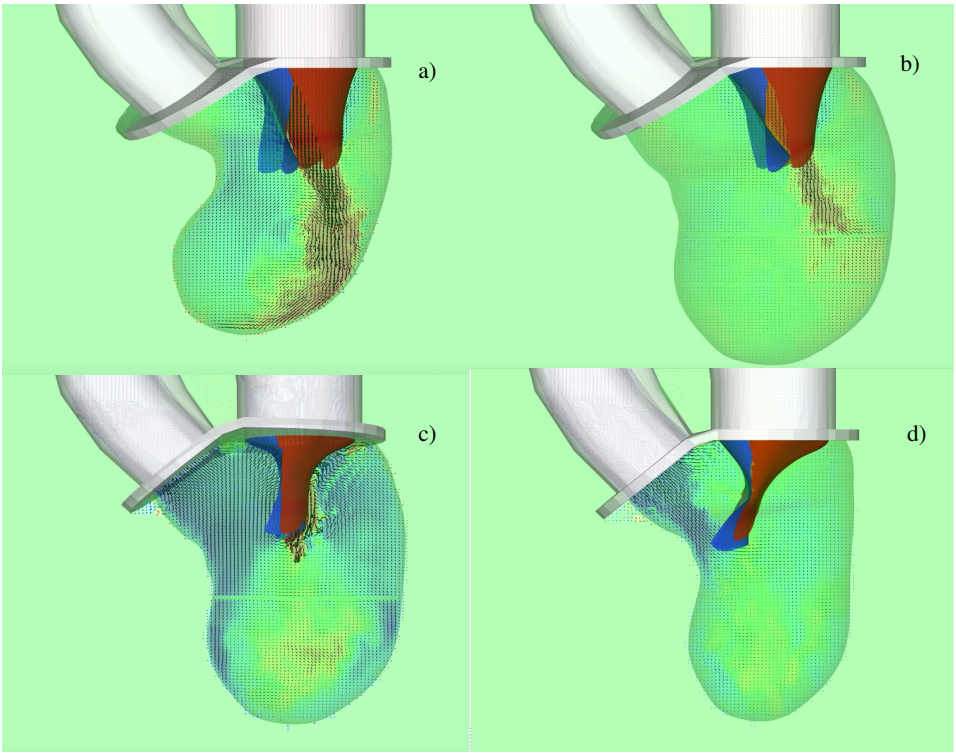

Figure 5.6: Snapshots of the velocity vector in the x–z symmetry plane and contours of vertical velocity at $EF = 60\%$ at different instants of the cardiac cycle: a) peak of E–wave, b) peak of the A–wave, c) mid–systole, d) end–systole.

5.3.2 HCM: a severe case of left ventricle hypertrophy with elongated leaflets

In order to evaluate the role of the septum thickening on the patho–physiology of HCM, the same set–up as before is adopted here except for the ventricle geometry which has a more pronounced hypertrophy (red shape of figure 5.2). This severely hypertrophic ventricle is characterized by an initial volume $V_2 = 2.19$, corresponding to half the physiological value ($V_2/V_0 = 50\%$). In figure 5.8 four snapshots of the velocity vector fields coloured with vertical velocity, at the same instants as figure 5.6, are reported showing a dynamics similar to the previous case. The most important difference is that the severe hypertrophy level brings the leaflets in contact with the ventricle septum thus further obstructing the aortic channel (figure 5.8d). Looking at figure 5.9 it can be noted that $\overline{X}$ attains, at the end of the cycle, smaller values than for the previous case (figure 5.7) implying that the leaflets move less to the left. However, because of the thicker ventricle septum, they come anyway in contact and prevent the blood from freely flowing into the aorta.

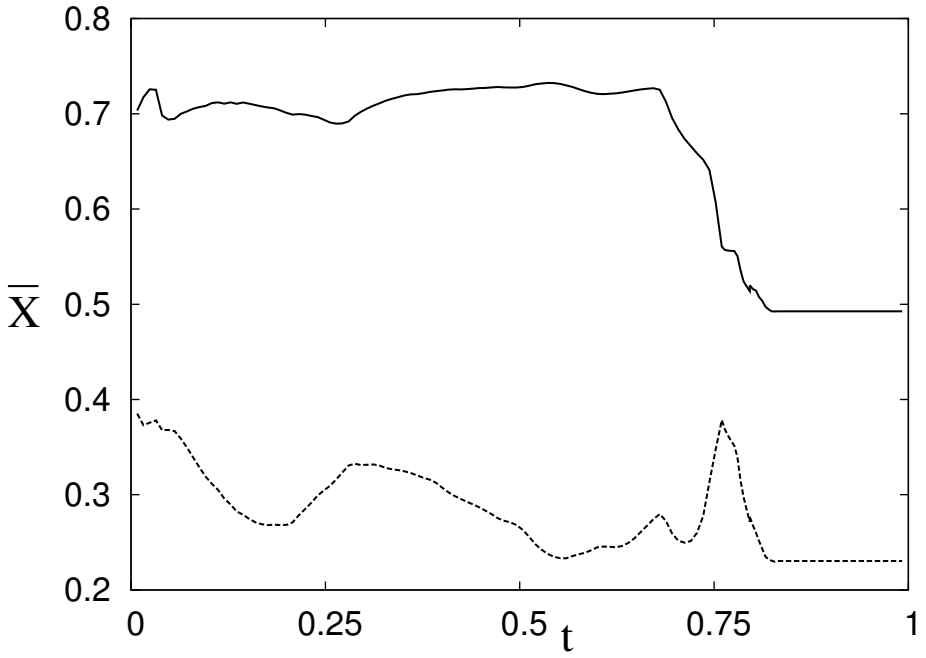

Figure 5.7: Time evolution of the mean horizontal coordinate $\overline{X}$ of the posterior (——) and anterior (·····) leaflet of the natural mitral valve for the first level of ventricle hypertrophy.

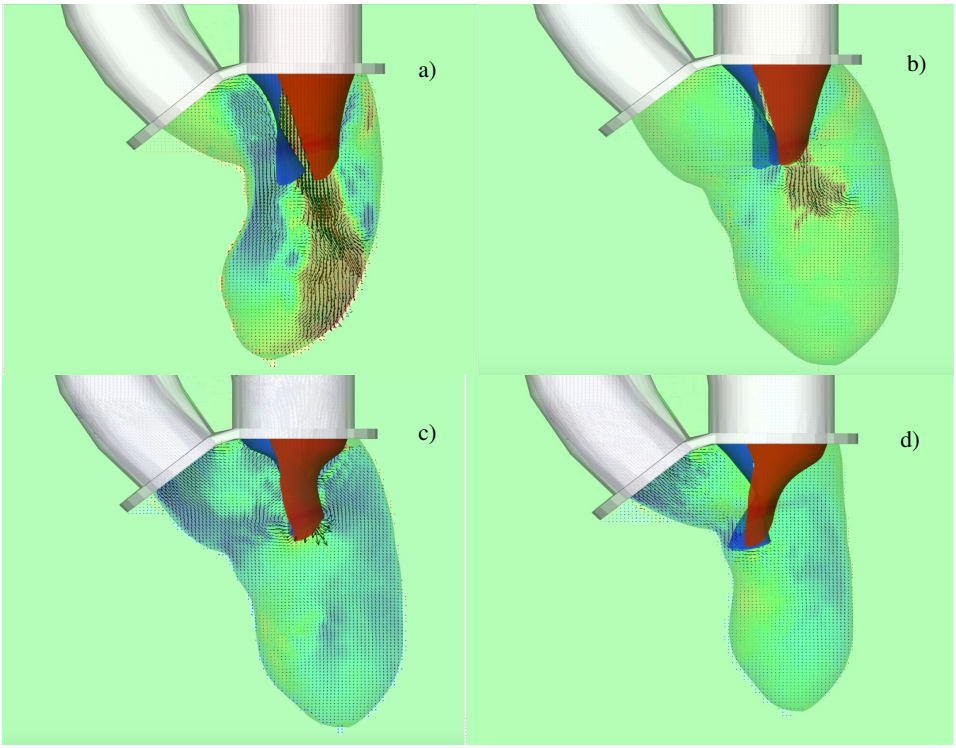

Figure 5.8: The same as figure 5.6, but for a different ventricle geometry characterized by a greater degree of thickening t_2 and a smaller initial volume V_2.

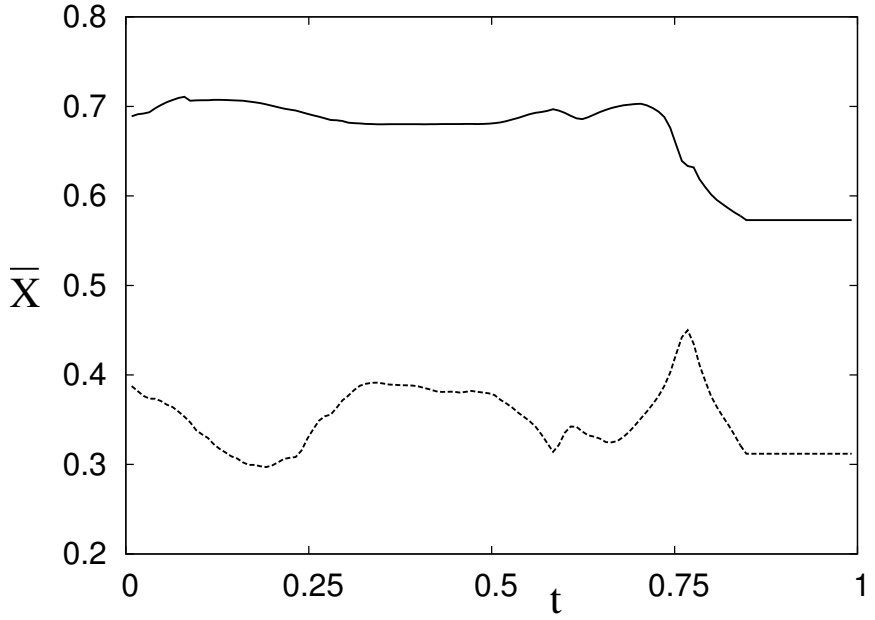

Figure 5.9: The same as figure 5.7, but for a more severe level of left ventricle hypertrophy.

In the clinical practice, an easy quantity used to characterize the HCM pathology is the aortic transvalvular pressure drop (TPD) which is the pressure difference upstream and downstream the aortic valve at peak systole. This quantity is referred to as 'transvalvular pressure *gradient*' by the medical community and it is widely used in this context (Maron *et al.* (1995); Naidu (2015)) owing to its simplicity and correlation with the pathology. Cardiac surgeons define *obstructive* the hypertrophic cardiomyopathy if TPD$\geq$ 30 mmHg and non–obstructive if it is $<$ 30 mmHg. In our model this threshold corresponds to the non–dimensional value $\mathrm{TPD_{ad}} \approx 6$ and we have obtained $\mathrm{TPD_{ad}} = 6.1$ for the first ventricle (section 5.3.1) and 6.4 for the present case.

5.3.3 Physiological ventricle with elongated leaflets

According to (Maron *et al.*, 1995) the thickening of the ventricular septum often occurs together with an excessive length of the mitral valve leaflets and this combination can produce the obstruction of the aortic channel during systole. Here we want to test whether these long leaflets in a physiological ventricle (blue shaded in figure 5.2) are still able to produce systolic anterior motion. Simulations are carried out for the same parameters as subsections 5.3.1 and 5.3.2, except for the ventricle geometry. The snapshots of figure 5.10 show how during diastole the left ventricle deformations are different although the flow has similar features. However, during systole, when the mitral valve closes, the leaflets do not move towards the aortic channel and no obstruction of the outflow tract is measured. Further confirmation of this behaviour comes from figure 5.11 where there is no evidence of the sudden $\overline{X}$ decrease for $t \geq 0.76$ evidencing the systolic anterior motion.

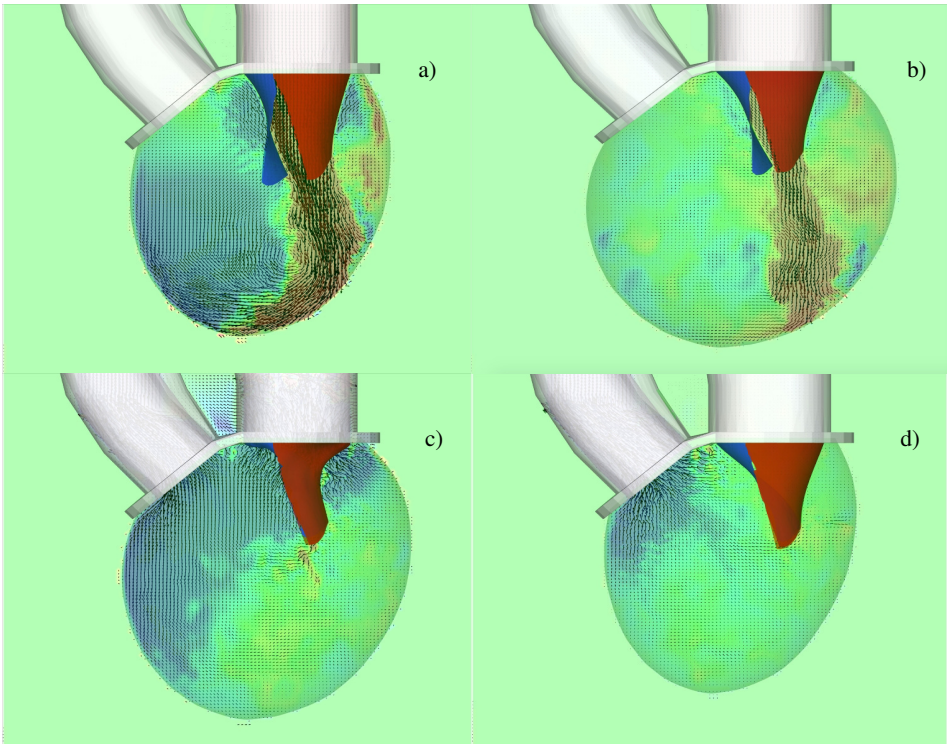

Figure 5.10: The same as figure 5.6 and 5.8, but with the geometry of a physiological left ventricle with elongated leaflets.

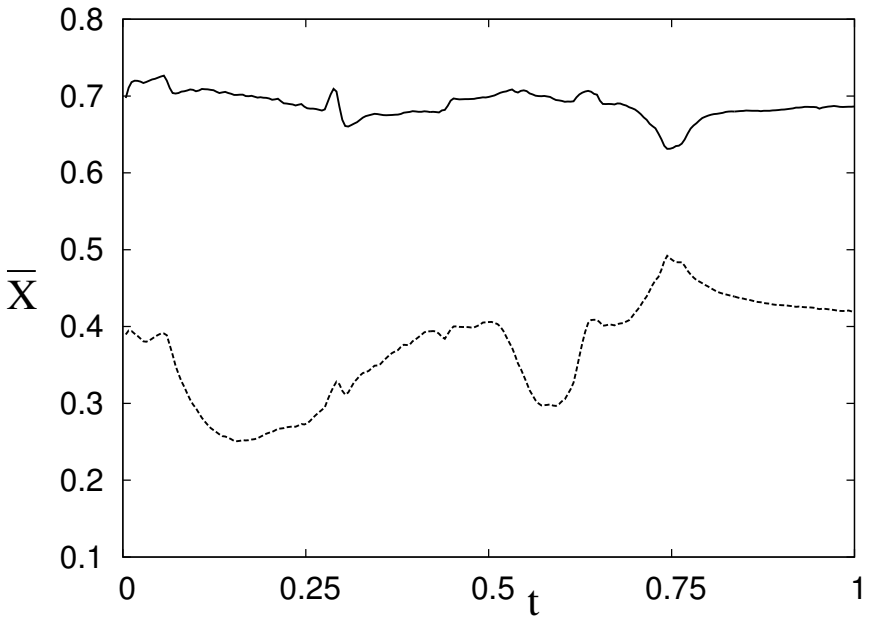

Figure 5.11: The same as figure 5.7, but for a physiological left ventricle with elongated leaflets.

5.3.4 HCM: a severe ventricle hypertrophy with elongated leaflets and reduced ejection fraction EF=40%

In order to isolate the effect of the ventricle pumping efficiency in HCM, a case with pathological ejection fraction ($EF = 40\%$) is analysed using the set–up with severe HCM discussed in section 5.3.2. The rationale behind this test is that it appears that the systolic anterior motion is triggered by the low pressure induced in the aortic channel by the abnormal flow conditions. In the previous sections we have shown that this requires a combination of septum thickening and mitral leaflets elongation to produce the ventricle obstruction. However, the pathologic low pressure in the aortic subvalvular region can not be produced if the systolic flow rate, or in other words the ejection fraction, is high enough and it is reasonable to speculate that impaired ventricles are less keen on producing blockage.

A comparison of figures 5.8 and 5.12 reveals that it is indeed the case and a weakened flow with a reduced ejection fraction does not generate obstruction. The mitral valve opens less during E–wave and A–wave (figures 5.12ab) and the weak systole does not allow a perfect mitral valve closure (figure 5.12c). In the remaining part of the cycle no anterior systolic motion is observed with the leaflets that maintain their mean X position (figure 5.13).

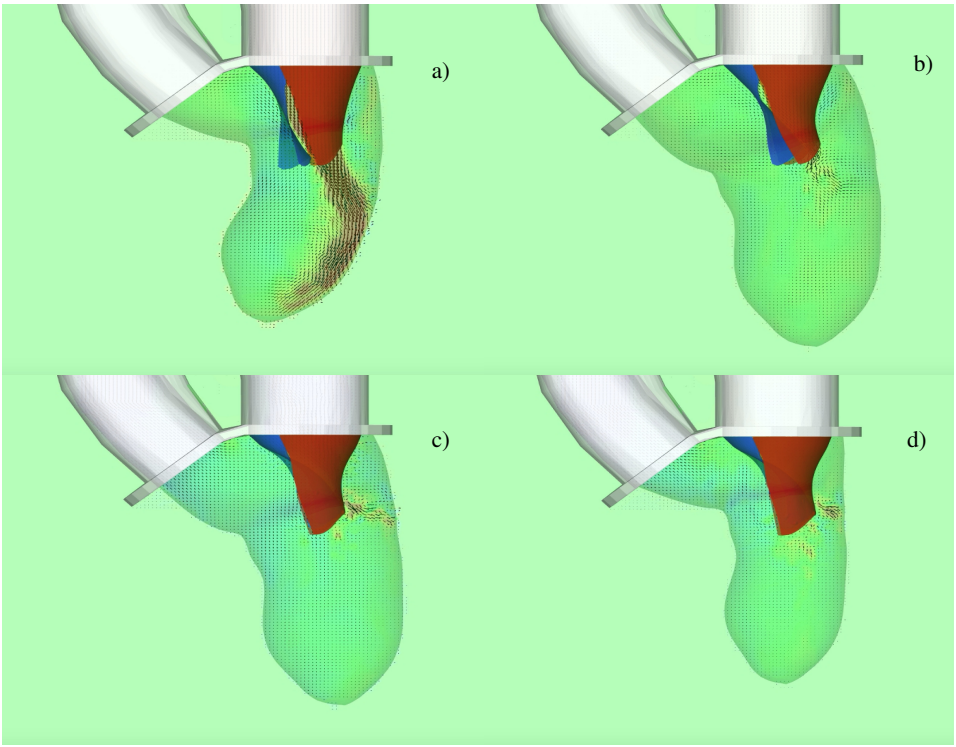

Figure 5.12: The same as figure 5.8, but with a reduced ejection fraction of 40%.

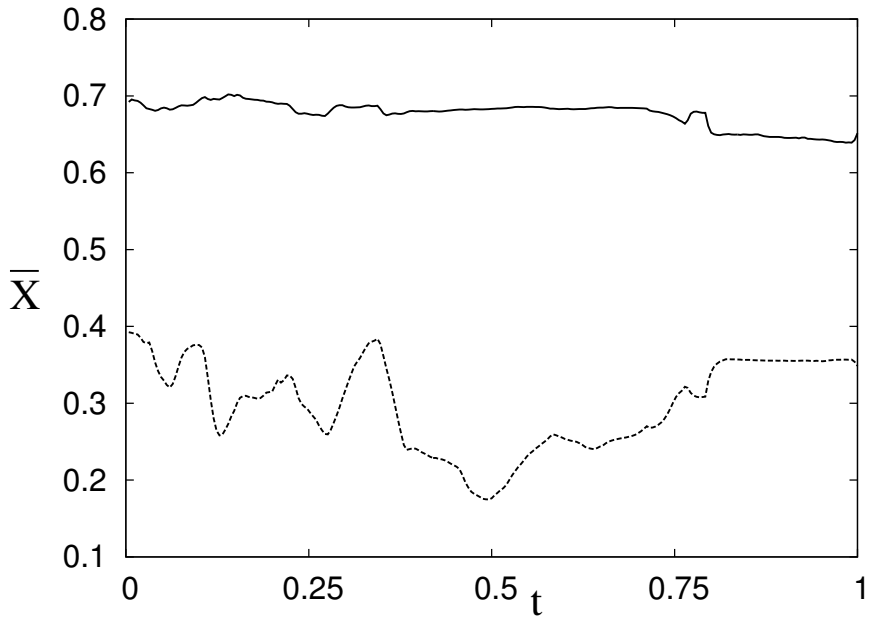

Figure 5.13: The same as figure 5.9, but with a reduced ejection fraction of 40%.

5.3.5 Testing surgical techniques for HCM: leaflets plication and septal myectomy

As mentioned in the introduction, HCM is a disease without a known specific cure, even though drug therapy (essentially beta–blocking agents aimed at reducing the systemic blood pressure that, in turn, decreases the aortic transvalvular pressure drop) works reasonably well for most of the people. There are however patients who may be intolerant to the drug or develop severe HCM symptoms after a few years on medications and alternative surgical procedures must be considered for them. Mitral leaflets plication and septal myectomy are the most effective procedures; the former consists of shortening the elongated leaflets to their physiological length, while the latter implies the removal of the abnormal growth of the thickened septum protruding inside the left ventricle, as shown in figure 5.16a. Both are aimed at eliminating the systolic anterior motion and the obstruction of the aortic channel.

These surgical measures are simulated here using the same set–up as in the previous sections. The leaflet plication is mimicked using the same configuration as in subsection 5.3.2 but with the physiological leaflets of figure 5.4a. Figure 5.14 reports the snapshots of the velocity field at the same instants as figure 5.8 and the the only relevant difference is the absence of mitral leaflet migration at the end of the cycle (figure 5.14d). This is confirmed by figure 5.15, in which no rapid decreasing of the x–centroids can be observed at $t = 0.76$. The transvalvular pressure drop in the present case is TPD= 3.8 which is clearly below the pathologic threshold of $\mathrm{TPD}_{\mathrm{th}} = 6$ which induce ventricle outflow obstruction.

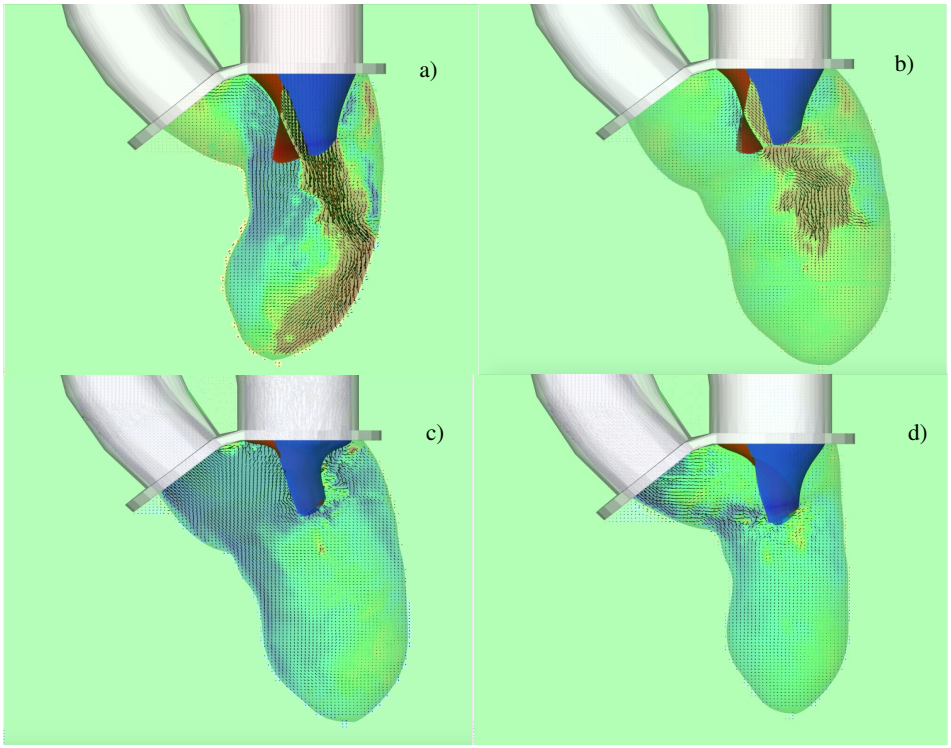

Figure 5.14: The same as figure 5.8, but with shortened leaflets.

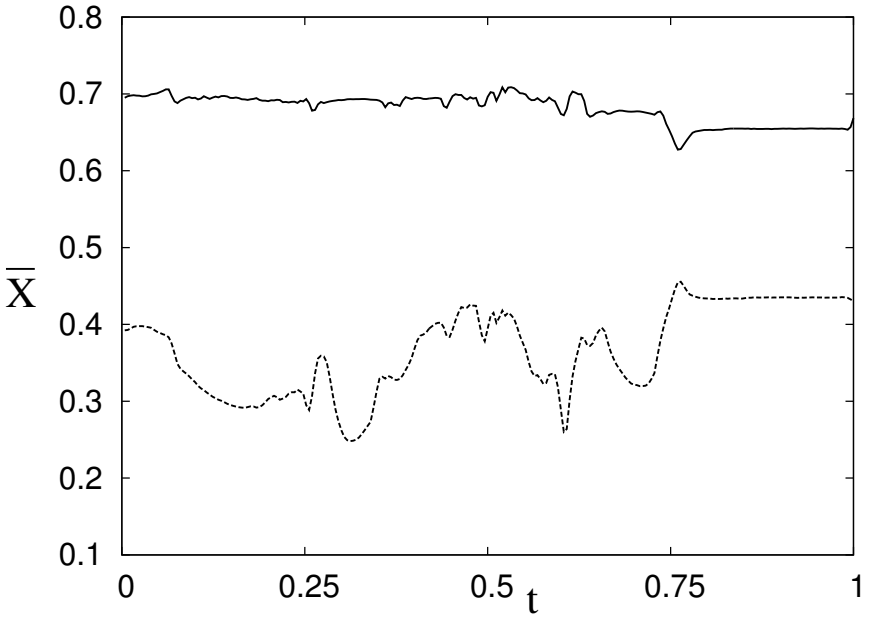

Figure 5.15: The same as figure 5.9, but in the case of leaflet plication.

The other surgical intervention of septal myectomy is also numerically simulated and, since it consists of removing the overgrown septum (figure 5.16a), a new the left ventricle geometry has been used in combination with elongated leaflets (figure 5.16b).

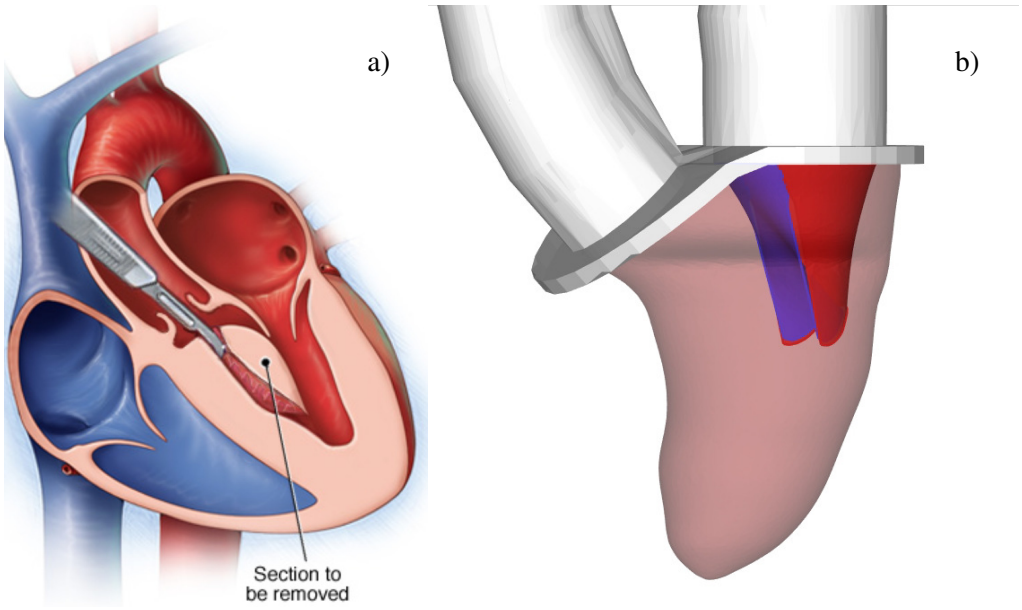

Figure 5.16: a) Sketch of septal myectomy intervention. b) Numerical set–up for the simulation of septal myectomy.

The results are summarized in figure 5.17; as for the previous case, the system dynamics is similar to that of figure 5.8 during diastole, whereas no migration of the elongated mitral leaflets is observed during systole. Again the leaflets centroids $\overline{X}$ do not show the sudden decrease at $t = 0.76$ that indicates the anterior systolic motion (figure 5.18) and also the transvalvular pressure drop, around 4, is sufficiently far from the pathological threshold $\mathrm{TPD}_{\mathrm{th}} = 6$).

In both cases the numerical results support the effectiveness of the surgical procedures and this is an additional confirmation of the reliability of the model which could be used to improve the current intervention techniques and to predict the outcome of innovative procedure of to fine tune the risk stratification of the patients.

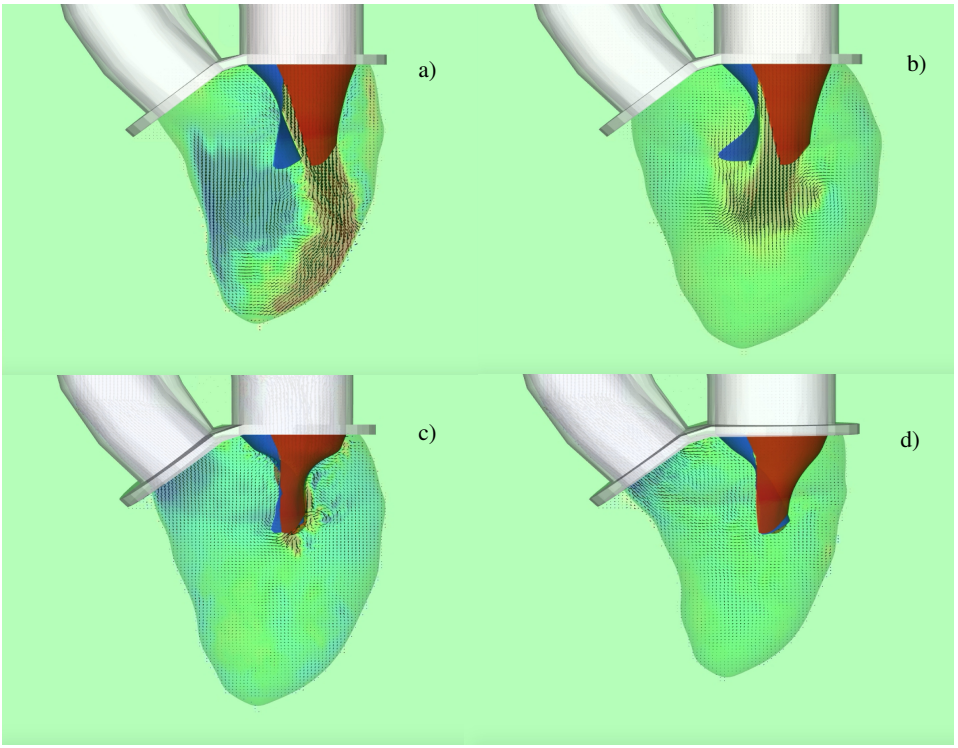

Figure 5.17: The same as figure 5.8, but with a geometry of the left ventricle which replicates septal myectomy.

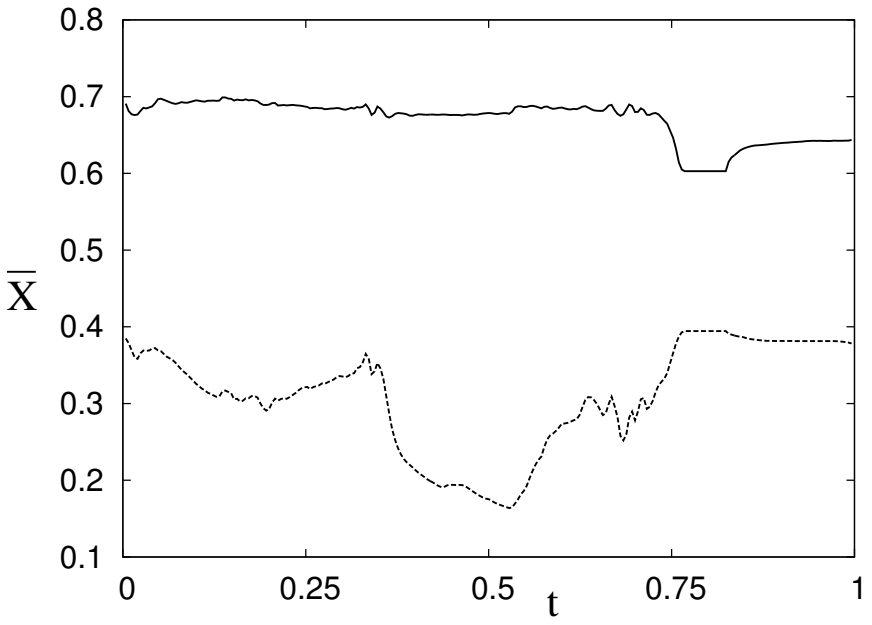

Figure 5.18: The same as figure 5.9, but in the case of septal myectomy.

5.4 Discussion and closing remarks

In this chapter we have presented a computational model that can cope with the patho–physiology of hypertrophic cardiomyopathy of the left ventricle. This tool has proven to be reliable for replicating the flow, the mitral valve dynamics and especially the migration of the leaflets towards the septum, which has been identified as the cause of sudden death. Once the reliability of the package has been assessed, a full parametric study has been performed to identify the factors responsible of the systolic anterior motion.

The systolic anterior motion has been indeed observed in both cases with elongated leaflets and hypertrophic ventricles, even though at different severity levels. In contrast a physiological ventricle with elongated leaflets has not shown the pathological systolic anterior motion. In an additional test it has been found that in order for the pathology to be effective, not only the hypertophy has to be severe and the mitral valve leaflets elongated but also the ventricle ejection fraction must be within physiologic values. In fact a case with $EF = 40\%$ has shown the flow to be too weak to produce a strong enough aortic subvalvular pressure to induce the leaflets migration.

Finally the two standard surgical procedures of leaflet plication and septal myectomy have been numerically tested and their effectiveness in eliminating the mitral leaflet migration has been verified.

All the numerical results have indicated that the occurrence of pathological behaviours in HCM are related to the combined effects of thickened and abnormal growth of the septum, elongated leaflets of the mitral valve and physiological values of the ejection fraction; if one of these factors is missing the systolic anterior motion does not occur. A further confirmation has been obtained from the evaluation of the transvalvular pressure drop (or transvalvular pressure gradient for the medical community), which gives an immediate quantification of the obstruction level of the outflow tract: in both cases showing obstruction this quantity has been found to exceed the threshold of 30 mmHg. In contrast when no systolic anterior motion is observed the pressure drop is always below the threshold.

Chapter 6

Conclusions

The achievement of a computational model able to provide a high–fidelity description of cardiac hemodynamics, reflecting also its accurate biology and chemistry, is still a challenge. However, several advances in modeling have been made in the last decades in overcoming the common practice of considering only separate parts of the entire complex cardiac system, thus leading to oversimplified models and consequently producing unreliable computational results far from clinical findings and medical needs. The necessity of having a self–consistent model in which all the cardiac elements work in a synergistic way, starting from the fluid/structure interaction has become unavoidable. Motivated by these arguments, in this thesis we have developed a multi–physics computational model for the flow inside the left ventricle of the human heart, coupling the fluid and structure dynamics. The core of our model has been a direct numerical simulation solver for the time dependent incompressible flow which essentially discretize the Navier–Stokes equations in space using second–order finite–difference schemes, with all the viscous term treated implicitly and the convective ones explicitly. In a complex deforming computational domain like the left ventricle the time integration of the Navier–Stokes equations would be very difficult without the use of immersed boundary methods (IBM). These methods make things easier because they avoid body fitted meshes, handle moving boundaries and deforming domains and, equally important, they have a reduced computational cost. To compute the structure dynamics a structural solver based on an a interaction potential approach has been employed. The ultimate purpose of simulating the synergistic functioning of all the elements of the left ventricle has been achieved thanks to a loose coupling FSI algorithm with a substepping procedure for the structure dynamics.

The resulting complex computational model has been validated using an ad–hoc experimental set–up: a one–to–one comparison between numerical results and experimental measurements for the flow dynamics, the ventricle deformation, the behaviour of mitral valve has given a first confirmation of the modeling reliability, which has represented a fundamental step for daring further investigations in different related problems.

In chapter 3, the computational model has been employed to asses the performance of different types of mitral valves (natural, prosthetic mechanical or biological) on the flow structure inside the ventricle. It has been found that the ventricular flow is heavily affected by the specific type of mitral valve,

whose effects are more pronounced for a ventricle with reduced pumping efficiency. More precisely, if the ejection fraction of the ventricle (EF) is in the physiological range ($50-70\%$), independently from the mitral valve geometry, the mitral jet sweeps up to the ventricle apex thus preventing apical blood stagnation. On the other hand for pathological values of ejection fraction (around 40%) the coupled effect of the weakened flow and the disturbances introduced by prosthetic devices results in a reduced penetration capability of the mitral jet thus originating a region of stagnant fluid. From a medical point of view these outcomes translate into the occurrence of heart attacks or more generally cardiac pathologies. These findings could be used as additional elements in the prosthesis selection for valve replacement, since presently the main decision factor between a biological or mechanical prosthetic device is the life expectation of the patient.

Despite the useful insights achieved with this model, it has to be mentioned that the geometry of the natural valve employed in chapter 3 had a simplified shape, since chordae tendineae were not physically included in the model and their kinematic effect has been replaced by numerical constraints. In order to fill this gap in chapter 4 a new geometry for a chorded mitral valve has been analysed. Even though the whole network of chordae tendineae is much more complex, we have decided to model them as only four bands, since this has been considered sufficient to reproduce their function. As a result, a double interaction between fluid and structure has been obtained, since the mitral valve opens and the left ventricle expands not only thanks to the incoming fluid but also to the tension of chordae tendineae and viceversa during the contraction phase. Moreover comparisons between velocity fields originated by the chorded mitral valve and the non chorded one have been performed, pointing out the disturbance effect of such chordae inside the left ventricle.

The main purpose of computational models for cardiac hemodynamics is to support the medical community, with the hope of having a powerful tool for testing new intervention procedures or treatments for cardiac pathologies. Although our model is still far from achieving this final goal, in chapter 5 we have made a first attempt by replicating the patho–physiology of hypertrophic obstructive cardiomyopathy, which is a lethal pathology related to the thickening of the interventricular septum and the elongation of the leaflets. Our model has shown to be able to capture the pathological behaviours and especially the systolic anterior motion of the elongated mitral leaflets due to the accelerating flow in the narrower aortic channel. Different levels of hypetrophy have been tested and, consequently, different levels of obstruction have been observed. In addition the two standard surgical interventions of septal myectomy, which consists in the removing of the protruding part of the septum, and leaflets plications, which produces shortened leaflets, have been simulated and their effectiveness in eliminating the systolic anterior motion of the mitral valve leaflets has been confirmed.

Along the thesis we have clarified that our model has some differences with respect to the human left ventricle. The most relevant is the ventricle dynamics that, even if fully coupled with the flow, is passive and driven by the prescribed inflow/outflow and the subsequent developing flow structure, while in reality the ventricle actively contracts during the systole and determines the outflow rather than adapting to it. Moreover the contraction is caused

by an electrical signal which propagates through the intraventricular septum, reaches the apex and moves up to the ventricle following a helical path (Kocica *et al.*, 2006). Therefore the ventricle contraction is not homogeneous, but instead starts from the apex and produces a twist of the myocardium; this implies that the flow during the systole could be different from that observed in the present study. Nevertheless, the diastolic phase is indeed passive, since the myocardium relaxes and it adapts to the E– and A–waves that are produced by the pressure of the blood coming from the pulmonary veins and the atrial contraction. The diastolic flow obtained in this study is thus closer to the real one and the results could be relevant for the heart, except for the twisting motion at the boundaries. Accordingly this is an ongoing project which aims at making the model closer to the real heart. The next step will consists of the addition of an electrophysiologic model that accounts for the anisotropic propagation of the electrical signal through the myocardium and allows for its active contraction (Clayton *et al.*, 2011). Once the electrophysiology will be included and coupled in the full FSI algorithm to the structural and fluidynamics solvers, the modeling of the whole left ventricle with the synergistic functioning of all its components will be reached. As shown in figure 6.1, the computational set–up has already been prepared, including the physical aortic valve and the deformable aorta, and tested without the active contraction/relaxation.

Having now this objective in mind, our prospect goes directly one step further to our final goal, which would be to add one by one all the other cardiac chambers, starting from the left atrium, and achieve the modeling of the whole human heart. We believe that the crucial point in achieving such a challenging purpose would lie in adding the active contraction/relaxation, since our computational model is already programmed for an arbitrary number of bodies. Our group is already working on these aspects and each one will be the topic of a future paper.

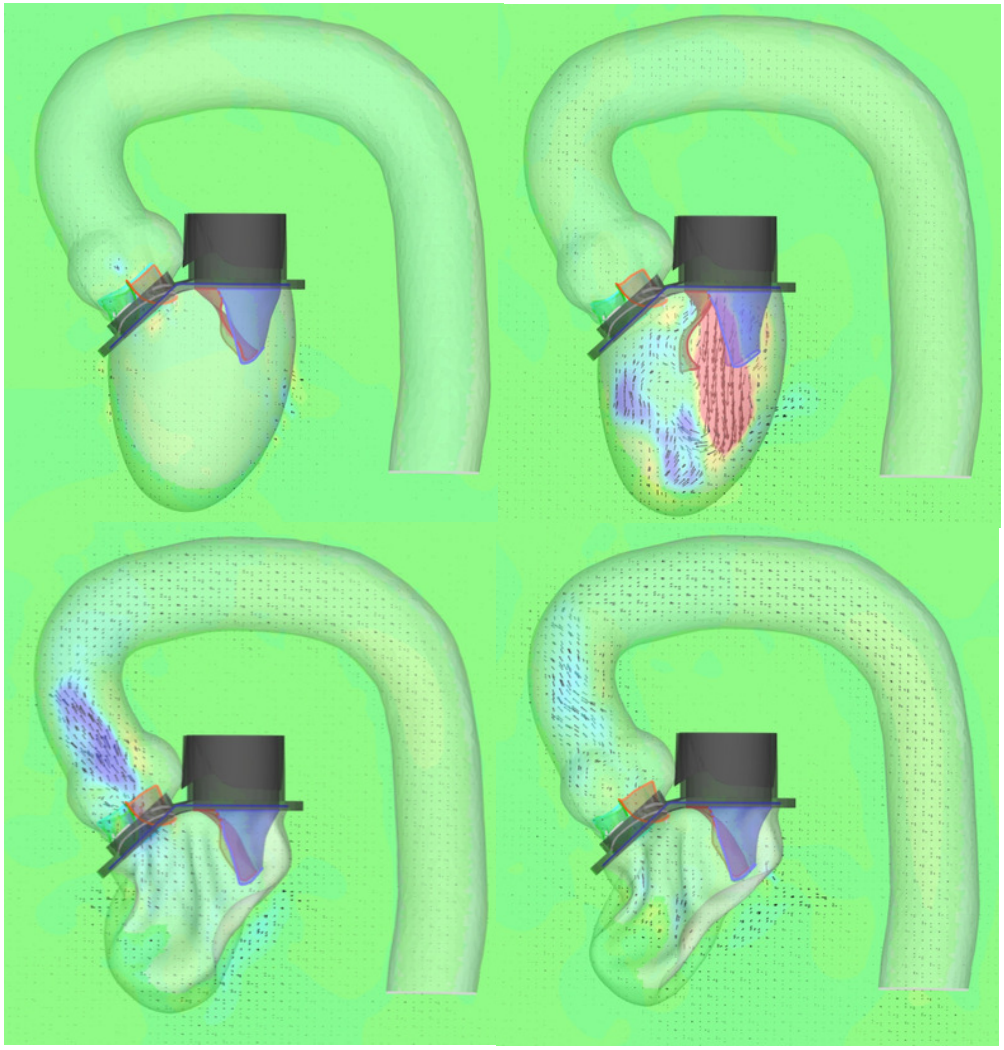

Figure 6.1: Instantaneous snapshots of the velocity field of the flow inside the whole left ventricle computational set–up including aortic valve and deformable aorta.

Bibliography

Atluri, S.N., Cho, J.Y. & Kim, H.G. 1999 Analysis of thin beams, using the meshless local Petrov–Galerkin method, with generalized moving least squares interpolations. *Computational Mechanics* **24** (5), 334–347.

Baccani, B., Domenichini, F., Pedrizzetti, G. & Tonti, G. 2002 Fluid dynamics of the left ventricular filling in dialated cardiomyopathy. *J. Biomech.* **35**, 665–671.

Badas, M. G., Domenichini, F. & Querzoli, G. 2016 Quantification of the blood mixing in the left ventricle using finite time lyapunov exponents. *Meccanica* **52(3)**, 1–16.

Baillargeon, B., Rebelo, N., Fox, D. D., Taylor, R. L. & Kuhl, E. 2014 The living heart project: a robust and integrative simulator for human heart function. *Eur. J. Mech. A/Solids* **48**, 38–47.

Balachandar, S. & Eaton, J. K. 2010 Turbulent dispersed multiphase flow. *Ann. Rev. Fluid Mech.* **42**, 111–133.

Belytschko, T., Gu, L. & Lu, Y. Y. 1994 Fracture and crack growth by element free galerkin methods. *Modelling and Sim. in Mat. Sci. and Engg.* **2** (3A), 519.

Belytschko, T., Krongauz, Y., Organ, D., Fleming, M. & Krysl, P. 1996 Meshless methods: an overview and recent developments. *Computer Methods in App. Mech. and Engg.* **139** (1), 3–47.

Benjamin, E. J. et al. 2017 Heart disease and stroke statistics – 2017 update: a report from the american heart association. *Circulation* **131(4)**.

Biferale, L., Meneveau, C. & Verzicco, R. 2014 Deformation statistics of sub-Kolmogorov-scale ellipsoidal neutrally buoyant drops in isotropic turbulence. *J. Fluid Mech.* **754**, 184–207.

Blanke, P., Willson, A. B., Webb, J. G., Achenbach, S., Piazza, N., Min, J. K., Pache, G. & Leipsic, J. 2014 Oversizing in transcatheter aortic valve replacement, a commonly used term but a poorly understood one: dependency on definition and geometrical measurements. *Journal of Cardiovascular Computer Tomography* **8(1)**, 67–76.

Cannegieter, S. C., Rosendaal, F. R. & Briet, E. 1994 Thromboembolic and bleeding complications in patients with mechanical heart valve prostheses. *Circulation* **89**, 635–641.

Cannegieter, S. C., Rosendaal, F. R., Wintzen, A. R., van der Meer, F. J. M., Vandenbroucke, J. P. & Briët, E. 1995 Optimal oral anticoagulant therapy in patients with mechanical heart valves. *New England Journal of Medicine* **333**, 11–18.

Cen, Y. Y., Glower, D. D., Landolfo, K., Lowe, J. E., Davis, R. D., Wolfe, W. G., Pieper, C. & Peterson, C. 2001 Comparison of survival after mitral valve replacement with biologic and mechanical valves in 1139 patients. *Journal of Thoracic and Cardiovascular Surgery* **122(3)**, 569–597.

Chen, M. & Boyle, F. J. 2014 Investigation of membrane mechanics using spring networks: Application to red-blood-cell modelling. *Material Sci. and Eng. C* **43**, 506–516.

Chikwe, J., Yuting, P., Chiang, Y. P., Egorova, N. N., Itagaki, S. & Adams, S. H. 2015 Survival and outcomes following bioprosthetic vs mechanical mitral valve replacement in patients aged 50 to 69 years. *Journal of American Medical Association* **313(14)**, 1435–1442.

Choi, Y. J., Constantino, J., Vedula, V., Trayanova, N. & Mittal, R. 2015 A new MRI-based model of heart function with coupled hemodynamics and application to normal and diseased canine left ventricles. *Frontiers in Bioeng. and Biotech.* **3**.

Choi, Y. J., Vedula, V. & Mittal, R. 2014 Computational study of the dynamics of a bileaflet mechanical heart valve in the mitral position. *Annales of Biomedical Engineering* **42**, 1668–1680.

Clayton, R. H., Bernus, O., Cherry, E. M., Dierckx, H., Fenton, F. H., Mirabella, L., Panfilov, A. V., Sachse, F. B., Seemann, G. & Zhang, H. 2011 Models of cardiac tissue electrophysiology: Progress, challenges and open questions. *Progress in Biophysics and Molecular Biology* **104**, 22–48.

Cordero, C. D., Rossini, L., Martinez-Lagazpi, P., Del Villar, C. P., Benito, Y., Barrio, A., Fernandez-Aviles, F., Yotti, R., del Alamo, J. C. & Bermejo, J. 2015 Prediction of intraventricular thrombosis by quantitative imaging of stasis: A pilot color-doppler study in patients with acute myocardial infarction. *Journal of Amerinca Colleges of Cardiology* **65**.

Crowe, C. T., Troutt, T. R. & Chung, J. N. 1996 Numerical models for two-phase turbulent flows. *Ann. Rev. Fluid Mech.* **28** (1), 11–43.

De Bacco, W. M., Sartori, A. P., Sant'Anna, J. R. M., Santos, M. F., Prates, P. R., Kalil, R. A. K. & Nesralla, I. A. 2009 Risk factors for hospital mortality in valve replacement with mechanical prosthesis. *Brazilian Journal of Cardiovascular Surgery* **24(3)**, 334–340.

De Vita, F., de Tullio, M. D. & Verzicco, R. 2016 Numerical simulation of the non-newtonian blood flow through a mechanical aortic valve. *Theoretical and Computational Fluid Dynamics* **30(1)**, 129–138.

Domenichini, F. & Pedrizzetti, G. 2011 Intraventricular vortex flow changes in the infarcted left ventricle: Numerical results in an idealised 3d shape. *Comput. Meth. Biomech BioMed. Eng.* **14(1)**, 95–101.

Domenichini, F., Pedrizzetti, G. & Baccani, B. 2005 Three-dimensional filling flow into a model left ventricle. *J. Fluid. Mech.* **539**, 179–198.

Dowell, E. H., Clark, R. & Cox, D. 2004 *A modern course in aeroelasticity*. Springer.

Dupin, M. M., Halliday, I., Care, C. M. & Munn, L. L. 2008 Lattice Boltzmann modelling of blood cell dynamics. *Int. J. Comp. Flu. Dyn.* **22** (7), 481–492.

Einstein, D. R., Kunzelman, K. S., Reinhall, P. G., Nicosia, M. A. & Cocharan, R. P. 2005*a* Non-linear fluid-coupled computational model of the mitral valve. *Journal of Heart Valve Disease* **14(3)**, 376–385.

Einstein, D. R., Kunzelman, K. S., Reinhall, P. G., Nicosia, M. A. & Cochran, R. P. 2005*b* Non-linear fluid-coupled computational model of the mitral valve. *J. Heart Valve Dis.* **14(3)**, 376–385.

Einstein, D. R., Reinhall, P.G, Nicosia, M. A., Cocharan, R. P. & Kunzelman, K. S. 2003 Dynamic finite element implementation of non-linear, anisotropic hyperelastic biological membranes. *Computer Methods in Biomechanics and Biomedical Engeneering* **6**, 33–44.

Emans, M. & Zenger, C. 2005 An efficient method for the prediction of the motion of individual bubbles. *J. Comp. Fluid Dynamics* **19(4)**, 347–357.

Fadlun, E. A., Verzicco, R., Orlandi, P. & Mohd-Yosuf, J. 2000 Combined immersed-boundary finite-difference methods for three-dimensional complex flow simulations. *Journal of Computational Physics* **161**, 35–60.

Falchi, M., Querzoli, G. & Romano, G. P. 2006 Robust evaluation of the dissimilarity between interrogation windows in image velocimetry. *Exp. in Fluids* **41** (2), 279–293.

Faludi, R., Szulik, M., D'hooge, J., Herijgers, P., Rademakers, F., Pedrizzetti, G. & Voig, J. U. 2010 Left ventricular flow patterns in healthy subjects and patients with prosthetic mitral valves: An in vivo study using echocardiographic particle image velocimetry. *J. Thorac. Cardiovasc. Surg.* **139**, 1501–1510.

Fedosov, D. A. 2010 Multiscale modelling of blood flow and soft matter. PhD thesis, Brown University, Providence, United States.

Fedosov, D. A., Caswell, B. & Karniadakis, G. E. 2010 Systematic coarse-graining of spectrin-level red blood cell models. *Computer Methods in App. Mech. and Engg.* **199** (29), 1937–1948.

Feins, E. N., Yamauchi, H., Marx, G. R., Freudenthal, F. P., Liu, H., del Nido, P. J. & Vasilyev, N. V. 2014 Repair of posterior mitral

valve prolapse with a novel leaflet plication clip in an animal model. *J. Thorac. Cardiovasc. Surg.* **147(2)**, 783–791.

Fleishman, S., Cohen-Or, D. & Silva, C. T. 2005 Robust moving least-squares fitting with sharp features. In *ACM Trans. on Graphics*, , vol. 24, pp. 544–552. ACM.

Fornari, W., Picano, F. & Brandt, L. 2016 Sedimentation of finite-size spheres in quiescent and turbulent environments. *J. Fluid Mech.* **788**, 640–669.

Fortini, S., Espa, S., Querzoli, G. & Cenedese, A. 2015 Turbulence investigation in a laboratory model of the ascending aorta. *Journal of Turbulence* **16**, 208–224.

Fortini, S., Querzoli, G., Espa, S. & Cenedese, A. 2013 Three-dimensional structure of the flow inside the left ventricle of the human heart. *Experiments in Fluids* **54**, 1–9.

Freund, J. B. 2014 Numerical simulation of flowing blood cells. *Annual Rev. Fluid Mech.* **46**, 67–95.

Georgiadis, M. W. J. G. & Pasipoularides, A. 1992 Computational fluid dynamics of left ventricular ejection. *Ann. Biomed. Eng.* **20**, 81–97.

Griffith, B. E., Luo, X., Mcqueen, D. M. & Peskin, C. S. 2009 Simulating the fluid dynamics of natural and prosthetic heart valves using the immersed boundary method. *Int. J. Appl. Mech* **1(1)**, 137–177.

Grigioni, M., Daniele, C., D'Avenio, G. & Barbaro, V. 2001 The influence of the leaflets' curvature on the flow field in two bileaflet prosthetic heart valves. *Journal of Biomechanics* **34**, 613–621.

Guido, S. & Villone, M. 1998 Three-dimensional shape of a drop under simple shear flow. *J. of Rheology* **42** (2), 395–415.

Hammermeister, K., Sethi, G. K., Henderson, W. G., Grover, F. L., Oprian, C. & Rahimtoola, S. H. 2000 Outcomes 15 years after valve replacement with a mechanical versus a bioprosthetic valve: Final report of the veterans affairs randomized trial. *Journal of the American College of Cardiology* **36(4)**, 1152–1158.

Harfi, T. T., Seo, J. H., Yasir, H. S., Welsh, N., Meyer, S. A., Abraham, T. P., Gerge, R. T. & Mittal, R. 2017 The e-wave propagation index (epi): A novel echocardiographic parameter for prediction of left ventricular thrombus. derivation from computational fluid dynamic modeling and validation on human subjects. *International Journal of Cardiology* **227**, 662–667.

Hegen, D. 1996 Element-free Galerkin methods in combination with finite element approaches. *Computer Methods in App. Mech. and Engg.* **135** (1), 143–166.

Hoffmann, G., Lutter, G. & Cremer, J. 2008 Durability of bioprosthetic cardiac valves. *Deutsches Arzteblatt International* **105(8)**, 143–148.

Iaccarino, G. & Verzicco, R. 2003 Immersed boundary technique for turbulent flow simulations. *App. Mech. Rev.* **56** (3), 331–347.

Kobbelt, L. & Botsch, M. 2004 A survey of point-based techniques in computer graphics. *Comp. & Graph.* **28** (6), 801–814.

Kocica, M. J., Corno, A. F., Carreras-Costa, F., Ballester-Rodes, M., Moghbel, M. C., Cueva, C. N. C, Lackovic, V., Kanjuh, V. I. & Torrent-Guasp, F. 2006 The helical ventricular myocardial band: global, three–dimensional, functional architecture of the ventricular myocardium hemodynamics of the left ventricle. *European Journal of Cardio–thoracic Surgery* **295**, 521–540.

Kolluri, R. 2008 Provably good moving least squares. *ACM Trans. on Algorithms* **4** (2), 18.

Krongauz, Y. & Belytschko, T. 1996 Enforcement of essential boundary conditions in meshless approximations using finite elements. *Computer Methods in App. Mech. and Engg.* **131** (1), 133–145.

Krüger, T. 2016 Effect of tube diameter and capillary number on platelet margination and near-wall dynamics. *Rheologica Acta* pp. 1–16.

Kunzelman, K. S., Cochran, R. P., Chuong, C., Verrier, E. D. & Eberhart, R. D. 1993 Finite element analysis of the mitral valve. *Journal of Heart Valve Diseas.* **2(3)**, 326–340.

Kunzelman, K. S., Einstein, D. R. & Cocharan, R. P. 2007 Fluid-sructure interaction models of the mitral valve: function in normal and pathological states. *Philosophical Transaction of the Royal Society B: Biological Sciences* **362**, 1393–1406.

Kunzelman, K. S., Reimink, M. S. & Cochran, R. P. 1997*a* Annular dilatation increases stress in the mitral valve and delays coaptation: a finite element computer model. *Cardiovasc. Surg* **5(4)**, 427–434.

Kunzelman, K. S., Reimink, M. S. & Cochran, R. P. 1997*b* Flexible versus rigid ring annuloplasty for mitral valve annular dilatation: a finite element model. *Journal of Heart Valve Diseas.* **7(1)**, 108–116.

Lancaster, P. & Salkauskas, K. 1981 Surfaces generated by moving least squares methods. *Mathematics of Computation* **37** (155), 141–158.

Landau, L. D. & Lifshitz, E. M. 1959 *Fluid mechanics*.

Levine, R. A., Triulzi, M. O., Harrigan, P. & Weyman, A. E. 1987 The relationship of mitral annular shape to the diagnosis of mitral valve prolapse. *Circulation* **75**, 756–767.

Lim, K. H., Yeo, J. H. & Duran, C. M. G. 2005 Three dimensional asymmetrical modelling of the mitral valve: a finite element study with dynamic boundaries. *Journal of heart Valve DIsease* **14**, 386–392.

Liu, G. R. & Gu, Y. T. 2005 *An introduction to meshless methods and their programming*. Springer, Berlin, Germany.

Loth, E. 2008 Quasi-steady shape and drag of deformable bubbles and drops. *Int. J. Multi. Flow* **34** (6), 523–546.

Machler, H., Perthel, M., Reiter, G., Reiter, U., Zink, M., Bergmann, P., Waltensdorfer, A. & Laas, J. 2004 Influence of bileaflet prosthetic mitral valve orientation on left ventricular flow–an experimental in vivo magnetic resonance imaging study. *European Journal of Cardiothoracic Surgery* **26(4)**, 747–753.

Maffettone, P. L. & Minale, M. 1998 Equation of change for ellipsoidal drops in viscous flow. *J. Non-Newtonian Fluid Mech.* **78** (2), 227–241.

Magnaudet, J. & Eames, I. 2000 The motion of high-reynolds-number bubbles in inhomogeneous flows. *Annu. Rev. Fluid Mech.* **32** (1), 659–708.

Mahmood, F., Gorman, J. H., Subramanian, B., Gorman, R. C., Panzica, P. J., Hagberg, R. C., Lerner, A. B., Hess, P. E., Maslow, A. & Khabbaz, K. R. 2010 Changes in mitral valve annular geometry after repair: saddle-shaped versus flat annuloplasty rings. *Ann. Thorac. Surg.* **90**, 1212–1220.

Maron, B. J., Gardin, J. M. & Flack, J. M. et al. 1995 Assessment of the prevalence of hypertrophic cardiomyopathy in a general population of young adults: echocardiographic analysis of 4111 subjects in the cardia study. *Circulation* **92**, 785–944.

Maron, B. J., Ommen, S. R., Semsarian, C., Spirito, P., Olivotto, I. & Maron, M. S. 2014 Hypertrophic cardiomyopathy. present and future, with translation into contemporary cardiovascular medicine. *Journal of the American College of Cardiology* **64**, 83–99.

Mcqueen, D. M. & Peskin, C. S. 2000 A three-dimensional computer model of the human heart for studying cardiac fluid dynamics. *ACM SIGGRAH Comput. Graphics* **34(1)**, 56–60.

Meschini, V., de Tullio, M. D., Querzoli, G. & Verzicco, R. 2016 A computational approach for multi–physics biological flows. *ECCOMAS Newsletter* **June**, 10–13.

Meschini, V., de Tullio, M. D., Querzoli, G. & Verzicco, R. 2017 Flow structure in healthy and pathological left ventricles with natural and prosthetic mitral valves. *Journal of FluidMechanics (To appear)* .

Mihalef, V., Ionasec, P., Shuarma, P., Georgescu, B., Voigt, I., Suehling, M. & Comanicu, D. 2011 Patient-specific modeling of whole heart anatomy, dynamics, and hemodynamics from four-dimensional cardiac ct images. *J. R. Soc. Interface Focus* **1**, 286–296.

Millington S., C., Meir, A., Lawrence, L. & Stolinski, C. 1998 Structure of chordae tendineae in the left ventricle of the human heart. *Journal of Anatomy* **192**, 573–581.

Mittal, R. & Iaccarino, G. 2005 Immersed boundary methods. *Annu. Rev. Fluid Mech.* **37**, 239–261.

Mittal, R., Seo, J. H., Vedula, V., Choi, Y. J., Liu, H., Huang, H. H., Jain, S., Younes, L., Abrahamd, T. & George, R. T. 2016 Computational modeling of cardiac hemodynamics: Current status and future outlook. *Journal of Computational Physics* **305**, 1065–1082.

Naidu, Srihari S. 2015 *Hypertrophic Cardiomyopathy*. Springer.

Nakamura, M., Wada, S., Mikami, T., Kitabatake, A. & Karino, T. 2003 Computational study on the evolution of an intraventricular vortical flow during early diastole for the interpretation of color m-mode doppler echocardiograms. *Biomech. Model. Mechanobiol.* **2**, 59–72.

Pedrizzetti, G., Domenichini, F. & Tonti, F: 2010 On the left ventricular vortex reversal after mitral valve replacement. *Ann. Biomed. Eng.* **38**, 769–773.

Peskin, C. S. 1972 Flow patterns around heart valves: a numerical method. *J. Comp. Phys.* **10** (2), 252–271.

Peskin, C. S. 1977 Numerical analysis of blood flow in the heart. *J. Comput. Phys.* **25**, 220–252.

Peskin, C. S 2002 The immersed boundary method. *Acta numerica* **11**, 479–517.

Peskin, C. S. & McQueen, M. 1989 A three-dimensional computational method for blood flow in the heart i. immersed elastic fibers in a viscous incompressible fluid. *J. Comput. Phys.* **81**, 372–405.

Pibarot, P. & Dumesnil, J. G. 2009 Prosthetic heart valves: Selection of the optimal prosthesis and long-term management. *Circulation* **119**, 1034–1048.

Pibarot, P. & Dumesnil, J. G. 2012 Doppler echocardiographic evaluation of prosthetic valve function. *Heart* **98**, 69–78.

Picano, F., Breugem, W. P. & Brandt, L. 2015 Turbulent channel flow of dense suspensions of neutrally buoyant spheres. *J. Fluid Mechanics* **764**, 463–487.

van der Poel, E. P., Ostilla-Mónico, R., Donners, J. & Verzicco, R. 2015 A pencil distributed finite difference code for strongly turbulent wall-bounded flows. *Computers & Fluids* **116**, 10–16.

Prosperetti, A. 2015 Life and death by boundary conditions. *J. Fluid Mech.* **768**, 1–4.

Prosperetti, A. & Tryggvason, G. 2007 *Computational methods for multiphase flow*. Cambridge university press.

Prot, V., Haaverstad, R. & Skallerud, B. 2009 Finite element analysis of the mitral apparatus: annulus shape effect and chordal force distributionl. *Biomechanics and Modeling in Mechanobiology* **8**, 43–55.

Qiu, Z., Chen, X., Xu, M., Jiang, Y., Xiao, L., Liu, L. & Wang, L. 2010 Is mitral valve repair superior to replacement for chronic ischemic mitral regurgitation with left ventricular dysfunction? *Journal of Cardiothoracic Surgery* **5**, 107.

Querzoli, G., Fortini, S. & Cenedese, A. 2010 Effect of the prosthetic mitral valve on vortex dynamics and turbulence of the left ventricular flow. *Physics of Fluids* **22**, 041901.

Rai, M. M. & Moin, P. 1991 Direct simulations of turbulent flow using finite difference schemes. *J. Comp: Phys.* **96(1)**, 15–53.

Saber, N. R., Wood, N. B., Gosman, A. D., Merrifield, R. D., Yang, G., Charrier, C. L ., Gatahouse, P. D. & Firmin, D. N. 2003 Progess towards patient-specific computational flow modeling of the left heart via combination of magnetic resonance imaging with computational fluid dynamics. *Ann. Biomed. Eng.* **31**, 42–52.

Sacks, M. S., Merryman, W. D. & Schmidt, D. E. 2009 On the biomechanics of heart valve function. *Journal of Biomechanics* **42**, 1804–1824.

Salgo, S. I., Gorman, J. H., C., Gorman R., M., Jackson B., Bowen, F. W., Plappert, T., G., Sutton M. & Edmundus, L. H. 2002 Effect of annular shape on leaflet curvature in reducing mitral leaflet stress. *Circulation* **106**, 711–717.

Scardovelli, R. & Zaleski, S. 1999 Direct numerical simulation of free-surface and interfacial flow. *Ann. Rev. Fluid Mech.* **31** (1), 567–603.

Schaefer, S., McPhail, T. & Warren, J. 2006 Image deformation using moving least squares. In *ACM Trans. on Graphics*, , vol. 25, pp. 533–540. ACM.

Schenkel, T., Malve, M., Markl, M., Jung, B. & Oertel, H. 2009 Mri-based cfd analysis of flow in a human left ventricle methodology and application to a healthy heart. *Ann. Biomed. Eng.* **37(3)**, 505–515.

Schwarz, S., Kempe, T. & Fröhlich, J. 2015 A temporal discretization scheme to compute the motion of light particles in viscous flows by an immersed boundary method. *J. Comp. Phys.* **281**, 591–613.

Schwarz, S., Kempe, T. & Fröhlich, J. 2016 An immersed boundary method for the simulation of bubbles with varying shape. *J. of Comp. Phys.* **315**, 124–149.

Seo, J. H. & Mittal, R. 2013 Effect of diastolic flow patterns on the function of the left ventricle. *Phys. Fluids* **25** (11), 110801.

Seo, J. H., Vedula, V., Abraham, T., Lardo, A. C., Dawoud, F., Luo, H. & Mittal, R. 2014 Effect of the mitral valve on diastolic flow patterns. *Phys. Fluids* **26** (12), 121901.

Seo, J. H., Vedula, V., Abraham, T. & Mittal, R. 2013 Multiphysics computational models for cardiac flow and virtual cardiography. *Int. J. Num. Meth. Biomed. Eng.* **29** (8), 850–869.

Siginer, D. A., De Kee, D. & Chhabra, R. P. 1999 *Advances in the flow and Rheology of non-Newtonian fluids*. Amsterdam: Elsevier.

Sotiropoulos, F., Trung Bao, L. & Gilmanov, A. 2016 Fluid mechanics of heart valves and their replacements. *Ann. Rev. Fluid Mech.* **48**, 259–283.

Spandan, V., Meschini, V., de Tullio, M. D., Querzoli, G., Lohse, D. & Verzicco, R. 2017 A parallel interaction potential approach for large scale simulations of deformable interfaces and membranes. *Journal of Computational Physics* **348**, 567–590.

Spandan, V., Verzicco, R. & Lohse, D. 2016 Deformation and orientation statistics of neutrally buoyant sub-kolmogorov ellipsoidal droplets in turbulent taylor-couette flow. *J. Fluid Mech.* **809** (2), 480–501.

Sung, S. C., Chang, Y. H., Lee, H. D. & Woo, J. S. 2008 A novel technique of supra-annular mitral valve replacement. *Annals of Thoracic Surgery* **86(3)**, 1033–1035.

Tanaka, M., Wada, S. & Nakamura, M. 2012 *Computational Biomechanics*, *Theoretical Background and Biological/Biomedical Problems*, vol. 3. New York NY: Springer.

Taylor, C. A., Fonte, T. A. & Min, J. K. 2013 Computational fluid dynamics applied to cardiac computed tomography for noninvasive quantification of fractional flow reserve: scientific basis. *J. Am. Coll. Cardiol.* **61(22)**, 2233–2241.

Taylor, G. I. 1932 The viscosity of a fluid containing small drops of another fluid. *Proc. Royal Soc. Lond.* pp. 41–48.

Taylor, G. I. 1934 The formation of emulsions in definable fields of flow. *Proc. Royal Soc. Lond.* pp. 501–523.

Torza, S., Cox, R. G. & Mason, S. G. 1972 Particle motions in sheared suspensions xxvii. transient and steady deformation and burst of liquid drops. *J. Coll. Int. Sci.* **38** (2), 395–411.

Tryggvason, G., Dabiri, S., Aboulhasanzadeh, B. & Lu, J. 2013 Multiscale considerations in direct numerical simulations of multiphase flows. *Phys. Fluids* **25** (3), 031302.

de Tullio, M. D., Afferrante, L., Demelio, G., Pascazio, G. & Verzicco, R. 2011*a* Fluid–structure interaction of deformable aortic prostheses with a bileaflet mechanical valve. *Journal of Biomechanics* **44** (9), 1684–1690.

de Tullio, M. D., Cristallo, A., Balaras, E. & Verzicco, R. 2009 Direct numerical simulation of the pulsatile flow through an aortic bileaflet mechanical heart valve. *J. Flu. Mech.* **622**, 259–290.

de Tullio, M. D., De Palma, P., Napolitano, M. & Pascazio, G. 2011*b* Recent advances in the development of an immersed boundary method for industrial applications. In *Computational Fluid Dynamics*, pp. 601–606. Springer.

de Tullio, M. D., Nam, J., Pascazio, G., Balaras, E. & Verzicco, R. 2012 Computational prediction of mechanical hemolysis in aortic valved prostheses. *Euro. J. Mechanics-B/Fluids* **35**, 47–53.

de Tullio, M. D. & Pascazio, G. 2016 A moving least-squares immersed boundary method for simulating the fluid-structure interaction of elastic bodies with arbitrary thickness. *Journal of Computational Physics* **235**, 201–225.

de Tullio, M. D., Pedrizzetti, G. & Verzicco, R. 2011*c* On the effect of aortic root geometry on the coronary entry-flow after a bileaflet mechanical heart valve implant: a numerical study. *Acta Mechanica* **216(1)**, 147–163.

Uhlmann, M. 2004 *Simulation of particulate flows on multi-processor machines with distributed memory*. Ciemat.

Uhlmann, M. 2005 An immersed boundary method with direct forcing for the simulation of particulate flows. *J. Comp. Phys.* **209** (2), 448–476.

Uhlmann, M & Doychev, T 2014 Sedimentation of a dilute suspension of rigid spheres at intermediate galileo numbers: the effect of clustering upon the particle motion. *J. Fluid Mech.* **752**, 310–348.

Van Gelder, A. 1998 Approximate simulation of elastic membranes by triangulated spring meshes. *Journal of Graphics Tools* **3**, 21–41.

Vanella, M. & Balaras, E. 2009 A moving–least–squares reconstruction for embedded–boundary formulations. *Journal of Computational Physics* **228(18)**, 6617–6628.

Vedula, V., Fortini, S., Seo, J. H., Querzoli, G. & Mittal, R. 2014 Computational modeling and validation of intraventricular flow in a simple model of the left ventricle. *Theor. and Comp. Flu. Dyn.* **28** (6), 589–604.

Vedula, V., Seo, J. H., Lardo, A. C. & Mittal, R. 2016 Effect of trabeculae and papillary muscles on the hemodynamics of the left ventricle. *Computational Fluid Dynamics* **30**, 3–21.

Verzicco, R. & Orlandi, P. 1996 A finite-difference scheme for three-dimensional incompressible flows in cylindrical coordinates. *J. Comp. Phys.* **123** (2), 402–414.

Votta, E., Caiani, F., Veronesi, F., M., Soncini, M., Montevecchi F. & Redaelli, A. 2008 Mitral valve finite-element modelling from ultrasound data: a pilot study for a new approach to understand mitral function and clinical scenarios. *Phil. Trans. R. Soc.* **366**, 3411–3434.

Vukićević, M., Fortini, S., Querzoli, G., Espa, S. & Pedrizzetti, G. 2012 Experimental study of an asymmetric heart valve prototype. *European Journal of Mechanics - B/Fluids* **35**, 54–60.

Wang, S., He, G. & Zhang, X. 2013 Parallel computing strategy for a flow solver based on immersed boundary method and discrete stream-function formulation. *Computers & Fluids* **88**, 210–224.

Watton, P. N., Luo, X. Y., Yin, M., Bernacca, G. M. & Wheatley, D. J. 2008 Effect of ventricle motion on the dyanmic behaviour of chorded mitral valves. *Journal of Fluid and Structures* **24**, 58–74.

Wattona, P. N., Luob, X. Y., Yinc, M., Bernaccad, G. M. & Wheatleyd, D. J. 2008 Effect of ventricle motion on the dynamic behavior of chorded mitral valves. *J. Fluids Struct* **24(1)**, 58–74.

Yang, J. & Balaras, E. 2006 An embedded-boundary formulation for large-eddy simulation of turbulent flows interacting with moving boundaries. *J. Comp. Phys.* **215** (1), 12–40.

Zeng, Q. H. & Lu, D. T. 2004 Curve and surface fitting based on moving least-squares methods. *J. of Engg. Graph.* **1** (3), 84–87.

Zheng, X., Seo, J. H., Vedula, V., Abraham, T. & Mittal, R. 2012 Computational modeling and analysis of intracardiac flows in simple models of the left ventricle. *Eur. J. of Mech. B/Fluids* **35**, 31–39.

Scientific Output

Pubblications

- V. Meschini, M. D. de Tullio, G. Querzoli & R. Verzicco, 'A computational approach for multi–physics biological flows', *ECCOMAS Newsletter*, 2016.

- V. Spandan, V. Meschini, M. D. de Tullio, R. Ostilla-Monico, G. Querzoli, D. Lohse & R. Verzicco, 'A parallel interaction potential approach coupled with the immersed boundary method for deformable interfaces and membranes', *Journal of Computational Physics*, 348, 567-590, 2017.

- V. Meschini, M. D. de Tullio, G. Querzoli & R. Verzicco, 'Flow structure in healthy and pathological left ventricles with natural and prosthetic mitral valves', *Journal of Fluid Mechanics*, 2017, to appear.

- V. Meschini, M. D. de Tullio & R. Verzicco, 'Effects of chordae tendineae on the flow in the left heart ventricle', *European Journal of Physics E* special issue on *Fluids and Structures: Interaction and Modeling*, subtmitted.

- V. Meschini, R. Mittal & R. Verzicco, 'Flow-induced mitral leaflets motion in Hypertrophic Cardiomyopathy', in preparation.

Contributed talks

- NewTurbMeeting, Department of Physics, University of Roma Tor Vergata, 18 July 2016
  Hemodynamics of biological and mechanical valves

- EFMC11, European Fluid Mechanics Conference, Seville, 12 – 17 September 2016
  Fluid-Structure Interaction in the left ventricle of the human heart

- APS16 DFD, American Physical Society Conference, Portland, 20 – 22 November 2016
  Fluid-Structure Interaction in the left ventricle coupled with mitral valve

- AIMETA 2017, Salerno, 4 – 7 September 2017
  Fluid-Structure Interaction for the flow in the left heart ventricle coupled with natural and prosthetic mitral valve

- APS17 DFD, American Physical Society Conference, Denver, 19 – 21 November 2017
  Flow-induced mitral leaflets motion in Hypertrophic Cardiomyopathy